

A search for heavy long-lived staus in the LHCb detector at $\sqrt{s} = 7$ and 8 TeV

PRÉSENTÉE LE 21 OCTOBRE 2013
À LA FACULTÉ DES SCIENCES DE BASE
LABORATOIRE DE PHYSIQUE DES HAUTES ÉNERGIES
PROGRAMME DOCTORAL EN PHYSIQUE

ÉCOLE POLYTECHNIQUE FÉDÉRALE DE LAUSANNE
POUR L'OBTENTION DU GRADE DE DOCTEUR ÈS SCIENCES

PAR
Thi Viet Nga La

sur proposition du jury:

Prof. Olivier SCHNEIDER, président du jury
Dr Minh Tâm TRAN, directeur de thèse
Prof. Clara MATTEUZZI, rapporteur
Prof. Gregory R. SNOW, rapporteur
Dr Pierre NORTH, rapporteur

Acknowledgments

I am heartily thankful to my supervisor, Dr Minh-Tam Tran, who encourages, guides, and supports me from the initial to the final knowledge to achieve my PhD degree.

I express my deep gratitude to Prof. Aurelio Bay, the director of the LPHE, for giving me an opportunity to do this thesis in his laboratory and the useful advices on my work.

This thesis would not be completed without the great helps and useful discussions from my colleagues: Neal Gauvin, Stéphane Tourneur and Pierre Jaton (from EPFL), Katharina Müller (from University of Zürich), Robin Hans Ludar Van Der Leeuw (from NIKHEF), Gloria Corti (from CERN), Matthew Peter Coombes (from University of Bristol), and from all the members of the LHCb exotica group. I would like to send to all of you my sincere acknowledges.

I also would like to thank all the members of the jury: Prof. Olivier Schneider, Dr Minh-Tam Tran, Prof. Clara Matteuzzi, Prof. Gregory R. Snow and Dr Pierre North for their important corrections and comments.

Specially, I would like to thank Mr. Maurice Gailloud for the great corrections in this thesis making it becoming complete.

I am deeply indebted to our lovely secretaries, Esther and Erika, who always give to me the important assistance outside physics.

Thanks to all the members in LPHE for many interesting discussions, as well as life enjoying during my PhD time.

In addition to the professional supports, I would like to thank my supervisor and his wife, Mrs Tran Nguyen Anh Nga, for all their kindnesses.

I love to thank all my friends for their help and sharing.

Finally, my eternal gratitude to my parents, my brothers and my friend Ngoc-Linh NGUYEN, who always support and encourage me in everything.

Lausanne, 14 November 2013

Résumé

Le Grand Collisionneur de Hadrons (LHC) produit des collisions pp à 7 et 8 TeV depuis 2010 et promet une nouvelle ère de découvertes en physique des particules. L'une de ses expériences, le "Large Hadron Collider beauty" (LHCb), a été construit pour étudier la violation de CP dans le système des mésons B. En plus de la physique des mésons B, la nouvelle physique au-delà du Modèle Standard est également étudiée dans ce spectromètre à un seul bras. Avec plusieurs sous-détecteurs différents et la bonne résolution du système de détecteurs de traces, le détecteur du LHCb a la capacité de rechercher les particules chargées, lourdes et à longue durée de vie qui sont prédictes dans les extensions du Modèle Standard. L'une de ces extensions, le *minimal Gauge Mediated Supersymmetry Breaking* (mGMSB), propose une telle particule, nommée *stau* ($\tilde{\tau}$) - le partenaire bosonique du lepton tau (τ) dans les théories supersymétriques. La théorie prédit que les staus sont produits par paires dans les collisions pp ou à partir des désintégrations de particules plus lourdes et qu'ils n'ont que des interactions électromagnétiques avec les atomes du milieu comme les muons. A l'énergie du LHC, nous espérons que ces particules peuvent être produites si elles existent vraiment. Et si le taux de leur production est suffisant, nous aurons la chance de les découvrir au détecteur de l'expérience LHCb, ainsi que dans les autres expériences du LHC.

Cette thèse est consacrée à la recherche des paires de staus produites dans des collisions pp aux énergies de centre de masse $\sqrt{s} = 7$ et 8 TeV dans le détecteur LHCb. Dans ce but, nous avons généré des paires de staus avec sept masses différentes dans l'intervalle de 124 à 309 GeV/c^2 et avons simulé leurs parcours, ainsi que celui de leur bruit de fond de muons de la désintégration $Z^0, \gamma^* \rightarrow \mu^+ \mu^-$, dans le détecteur LHCb. En nous basant sur le résultat de la simulation, un ensemble de coupures est alors défini pour sélectionner les paires de staus.

Certaines paires de muons à haute énergies passeront aussi les coupures de sélection. Pour séparer les paires de staus et les paires de muons, des réseaux de neurones (Neural Network) ont été utilisés. Le premier réseau de neurones a été utilisé pour distinguer les traces de staus des traces de muons en utilisant leurs signaux laissés dans les sous-détecteurs : le détecteur au silicium VELO, le calorimètre électromagnétique, le calorimètre hadronique et les détecteurs RICH. Ensuite, nous avons développé deux méthodes pour sélectionner les paires de staus : la première méthode est basée sur le produit des réponses du premier réseau de neurones (NN1) aux traces d'une paire, la deuxième méthode est d'employer un deuxième réseau de neurones pour séparer les paires de staus des paires de muons en utilisant le produit des réponses NN1 et la masse invariante de la paire. Enfin, une région de staus a été définie et les nombres attendus

des paires de staus et de muons dans cette région ont été évalués. L'entraînement des réseaux de neurones a été réalisé avec des variables tirées de la simulation, les réseaux de neurones entraînés sont ensuite utilisés pour classifier les données.

Les données utilisées dans notre travail ont été collectées par l'expérience LHCb en 2011 et 2012 et correspondent aux luminosités intégrées de 1 fb^{-1} à $\sqrt{s} = 7 \text{ TeV}$ et de 2 fb^{-1} à $\sqrt{s} = 8 \text{ TeV}$. Aucun excès significatif d'un signal de stau n'a été observé.

Les limites supérieures à 95% CL sur la section efficace de production des paires de staus dans les collisions pp à $\sqrt{s} = 7$ et 8 TeV ont été calculées en utilisant la méthode de "profile likelihood", dérivée de celle de Feldman et Cousins.

Mots-clés : LHC, LHCb, Modèle Standard, Gauge Mediated Supersymmetry Breaking, particules chargées, lourdes et à longue durée de vie, staus.

Abstract

The Large Hadron Collider (LHC) has been producing pp collisions at 7 and 8 TeV since 2010 and promises a new era of discoveries in particle physics. One of its experiments, the Large Hadron Collider beauty (LHCb) experiment, was constructed to study CP violation in the B meson system. In addition to B physics, new Physics beyond the Standard Model can also be searched for at this single-arm forward spectrometer. With the different sub-detectors and the high resolution of the tracking system, the LHCb detector has the ability to search for heavy, long-lived and charged particles, which are predicted by extensions of the Standard Model. One of these extensions, the *minimal Gauge Mediated Supersymmetry Breaking* (mGMSB), proposes such a particle, named *stau* ($\tilde{\tau}$) - the SUSY bosonic counterpart of the heavy lepton tau (τ). The theory proposes that the staus may be pair-produced in pp collisions or in the decays of heavier particles, and have only electromagnetic interactions with the atoms of the medium like the muons. Therefore, we expect that at the energy of the LHC these particles can be produced if they do exist and that we have a chance to discover them at LHCb, as well as at the other experiments of the LHC.

This thesis is dedicated to the search for stau pairs produced in pp collisions at the centre-of-mass energies $\sqrt{s} = 7$ and 8 TeV in the LHCb detector. For this purpose, we generated the stau pairs with seven different particle masses ranging from 124 to 309 GeV/c² and simulated their path through the LHCb detector, as well as their muon background from the decays $Z^0, \gamma^* \rightarrow \mu^+ \mu^-$. Based on the results from the simulation, a set of cuts are then defined to select the stau pairs.

Some muon pairs at high energies will also pass the selection cuts. Thus, to separate the stau pairs from the muon pairs, the Neural Network technique has been used. A first Neural Network has been used to distinguish the stau tracks from the muon tracks using their signals left in the sub-detectors: the VELO silicon detector, the electromagnetic calorimeter, the hadron calorimeter and the RICH detectors. Then, two methods to select the stau pairs have been developed: the first one is based on the product of the two responses from the first Neural Network (NN1) for the two tracks, the second one employs a second Neural Network to separate the stau pairs from the muon pairs by using the above product of the two NN1 responses and the invariant mass of pair. Finally, a favourable region for the staus finding has been defined and the expected numbers of stau and muon pairs in this region have been evaluated. The training of the Neural Network has been achieved with the Monte Carlo variables, then the trained Neural Network has been used to classify the data.

The data used in our work were collected by the LHCb experiment in 2011 and 2012 and correspond to integrated luminosities of 1 fb^{-1} at $\sqrt{s} = 7 \text{ TeV}$ and of 2 fb^{-1} at $\sqrt{s} = 8 \text{ TeV}$. No significant excess of signal has been observed.

Upper limits at 95% CL on the cross section for stau pair production in pp collisions at $\sqrt{s} = 7$ and 8 TeV have been computed by using the profile likelihood method, which is derived from the well known Feldman and Cousins method.

Keywords: LHC, LHCb, Standard Model, minimal Gauge Mediated Supersymmetry Breaking, heavy long-lived and charged particles, staus.

Contents

Introduction	1
I. Theoretical Models	3
1. The Standard Model	5
1.1. The content of the Standard Model	5
1.2. Limits of the Standard Model and beyond it	11
2. Supersymmetry	15
2.1. Introduction to Supersymmetry	15
2.2. Supersymmetric Lagrangian	19
2.2.1. Lagrangian of the chiral supermultiplet	19
2.2.2. Lagrangian of the gauge supermultiplet	23
2.2.3. Lagrangian of the supersymmetric gauge interactions	24
2.2.4. Soft supersymmetry breaking	24
2.3. The Minimal Supersymmetric Standard Model	25
2.3.1. Grand Unification in MSSM	25
2.3.2. Superpotential in MSSM	27
2.3.3. <i>R</i> -parity	27
2.3.4. Soft SUSY breaking in MSSM	28
2.3.5. The mass spectrum of the MSSM	29
2.3.6. Origins of supersymmetry breaking in MSSM	33
2.4. The minimal GMSB models	34
2.4.1. Structure of mGMSB	34
2.4.2. The Lightest Supersymmetric Particle	37
2.4.3. The Next-to-Lightest Supersymmetric Particle	37
II. The LHCb experiment	41
3. Large Hadron Collider	43
4. LHCb detector	45
4.1. Magnet	46
4.2. The tracking system	46
4.2.1. Vertex Locator	47

4.2.2. Silicon Tracker	49
4.2.3. Outer tracker	53
4.2.4. Track reconstruction	54
4.3. The particle identification system	55
4.3.1. RICH	55
4.3.2. Calorimeters	58
4.3.3. The muon system	61
4.4. Trigger	64
4.5. Analysis framework and applications	67
III. Monte-Carlo and Results	69
5. Monte-Carlo	71
5.1. Generation of stau pairs in pp collisions	71
5.2. Simulation of staus and their backgrounds	76
5.2.1. Identification by the muon chambers	76
5.2.2. Backgrounds and a first attempt to reduce them	76
5.2.3. Triggering and stripping	78
5.2.4. Reconstruction of the tracks	79
5.2.5. Energy deposited in the VELO	80
5.2.6. Deposited energies in the calorimeters	85
5.2.7. Response of the RICHs	89
5.2.8. Impact parameter	92
5.2.9. Asymmetry in transverse momentum	93
5.2.10. Pair isolation	94
5.3. Selection and efficiencies	95
5.4. Other backgrounds	98
6. Analysis of the Monte Carlo data by Neural Network	99
6.1. Analysis of individual tracks	99
6.2. Selection of the stau pairs	101
6.2.1. Selection based on the pair significance	101
6.2.2. Selection based on the pair significance and invariant mass of the pairs	103
7. Results	109
7.1. Selection	109
7.2. Analysis of the tracks with Neural Network	111
7.3. Selection of the stau pairs	113
7.3.1. Selection based on the pair significance	113
7.3.2. Selection based on the pair significance and the invariant mass of the pairs	114
7.4. Systematics	123
7.5. Limit on cross section	129

Conclusions and Outlook	135
Bibliography	137
List of Figures	141
List of Tables	143

Introduction

Modern particle physics can be thought of as starting in the late 1940s with the discovery of the charged pions. After that, various particles, as well as their interactions, were observed. To describe the physics of the particles, the key theoretical elements of the Standard Model was formulated in the early 1970s. In 1983, the discovery of the W and Z bosons at CERN convinced physicists that the Standard Model was correct. Thirty years later, this model has once again shown its accuracy through the observation of the Higgs boson-like particle in the ATLAS and CMS experiments.

Though successful, the Standard Model does not completely explain all the data that we observed. To extend this model, the Supersymmetric theories were proposed in 1971 and are now one among the most plausible extensions. However, till now there is no experimental evidence to confirm these theories. It motivates us to carry out the search for a superparticle, the stau, at the LHCb detector. This manuscript describes this search and is organized as follows:

In part I, we will discuss about the theoretical models. Chapter 1 will shortly present the Standard Model and its limits. Then, in Chapter 2 we will describe the Supersymmetry (SUSY) and focus on the minimal Gauge Mediated Supersymmetry Breaking model, which predicts the existence of the massive and long-lived stau.

Part II will be dedicated to the description of the LHC and of the LHCb detector. This part is composed of the next two chapters (3 and 4). Chapter 3 will introduce briefly the LHC and its experiments. The LHCb experiment, its detectors, triggers and software will be described quite in detail in Chapter 4.

In part III, we have three chapters (5, 6 and 7) to present the works that were done to search for stau pairs:

- + Chapter 5 will describe the Monte Carlo for the stau pairs and their background in the LHCb detector. The characteristics of the staus and the response of the sub-detectors, will be examined to define the selection cuts for the stau pairs. The "calibration" of the Monte Carlo signals will be exposed; the aim of this calibration is to have the MC signals similar to the ones from data.

- + In Chapter 6, an analysis by a Neural Network to distinguish the stau tracks from muon tracks by using their signals in the sub-detectors will be presented. After that, we go on with the differentiation between stau pairs and muon pairs. The expected number of pairs for signal and background in the signal region will be given.

+ Finally, Chapter 7 will give the results obtained by applying the cuts and analysis method presented in Chapters 5 and 6. The results allow to compute the limits on the cross section for stau pair production in pp collisions at 7 and 8 TeV.

Part I.

Theoretical Models

Chapter 1.

The Standard Model

The Standard Model (SM) [1], [2] of Particle Physics is presently the theory that gives the best description of the elementary particles and their interactions. It allows to explain most of the experimental results and to predict many discoveries in Particle Physics. However, there are some experimental data that this model cannot explain. Moreover, this model does not include the gravity. This chapter will shortly review the content of the SM in section 1.1 and its limits in section 1.2.

1.1. The content of the Standard Model

The Standard Model (SM) of the Elementary Particles Physics is a quantum field theory [3], which is made up from the electroweak theory and the Quantum Chromodynamics (QCD) in order to represent the elementary particles and their interactions.

The particles and their interactions:

The most elementary fermions that we observed are the six *leptons* ($e, \mu, \tau, \nu_e, \nu_\mu, \nu_\tau$), the six *quarks* (u, d, c, s, t, b) and their antiparticles. Matter is made up from these. The particles interact with each other via their interactions: electromagnetic, weak, strong and gravitational. However, the present SM is only able to describe the three first ones. The three interactions in the SM are achieved by exchanging the force carriers (γ, W^\pm, Z^0, g) of spin 1, which are called the *gauge bosons*: the photon for the electromagnetic interaction, the W^\pm and Z^0 bosons for the weak interaction and the eight gluons (g) for the strong interaction. In addition, the SM also predicts the existence of a massive scalar (i.e. spin 0) particle, called the Higgs boson (H^0); via the interaction with the Higgs boson, the SM particles can acquire mass. Table 1.1 shows the elementary particle of the Standard Model.

		Fermions			Bosons
Quarks					
	u up	c charm	t top	γ photon	
Leptons	d down	s strange	b bottom	Z Z boson	
	ν_e electron neutrino	ν_μ muon neutrino	ν_τ tau neutrino	W W boson	g gluon
			μ muon	τ tau	H Higgs* boson
Source: American Association for the Advancement of Science; <i>The Economist</i>			*Confirmation just announced		

Table 1.1.: The elementary particles of the Standard Model

Quantum Electrodynamics:

It is quite significant a progress in modern particle theories, the concept of gauge invariance is now used for all forces of the SM: it has been first introduced in QED. Let us first have a look to the Quantum Electrodynamics (QED) - the starting point in the construction of the SM. This is a relativistic quantum field theory that successfully describes the electromagnetic interaction between charged particles via the photon (γ) exchange. This interaction must conserve the total electric charge. Thus the Lagrangian must be invariant under a certain group of symmetry transformation G . In QED, this group, denoted by $U(1)$, corresponds to a global shift in the phase of the particle wave-function, for which the Lagrangian \mathcal{L} is invariant.

$$G^{U(1)}\psi \rightarrow \psi^* \quad (1.1)$$

$$G^{U(1)}\mathcal{L}(\psi) \rightarrow \mathcal{L}^*(\psi^*) \quad (1.2)$$

However, under a local phase transformation $G(x)\mathcal{L}(\psi) \rightarrow \mathcal{L}^*(\psi^*)$ the Lagrangian is not invariant $\mathcal{L}(\psi) \neq \mathcal{L}(\psi^*)$. It is a very nice surprise that this problem can be

solved by redefining the derivative as a "covariant derivative" which then introduces an infinite field (A) whose quantum is massless. The Lagrangian is now invariant under the transformation:

$$G^{U(1)}(x)\mathcal{L}(\psi, A) \rightarrow \mathcal{L}(\psi^*, A^*) \quad (1.3)$$

The field required is the electromagnetic field whose quantum is the *photon*. In other words, the photon is the force carrier in the electromagnetic interactions.

Electro-Weak interaction:

Observations show that only left-handed fermions participate in the weak interaction, so we will split the wave-functions into the right and left-handed components. For example, lepton components are:

$$l_L = \begin{pmatrix} \nu_l \\ l^- \end{pmatrix}_L, \quad l_R \quad (1.4)$$

Let's consider a left-handed doublet; regardless of the charge the two particles feel the same weak interaction: this remind us of the low energy symmetry between the nucleon doublet (neutron and proton) and for which Werner Heisenberg has introduced in 1933 the concept of "*Isospin*" and the $SU(2)$ group of symmetry. Similarly, one can apply the concept of "*weak isospin*" to the left-handed doublet of leptons, and the related symmetry group is now $SU(2)^W$ where the superscript " W " refers to weak interaction.

As for QED and in order to comply with the local gauge invariance, one must introduce the massless gauge bosons W^\pm and W^0 . Here again, the gauge bosons $W^{\pm,0}$ communicate the local convention of rotation in the isospin space to all the interacting leptons. The fact that the gauge invariance requires the gauge bosons to be massless is quite inconvenient here because the range of the weak interactions is very short (below 1 fm). Therefore one expects the weak gauge bosons to be quite massive with respect to the energy scale which could be reached in the sixties. And this explains why these gauge bosons were not discovered yet in that period.

This difficulty can be overcome with the mechanism of the spontaneous symmetry breaking introduced by Peter Higgs and co-workers. The idea here is to introduce a massless scalar field of two components $\Phi = (\phi_1, \phi_2)$, called the Higgs field and the massless vector gauge particle, denoted by A for instance, responsible for communicating the ϕ_1, ϕ_2 content from place to place. Let us define a Lagrangian whose shape is the one of the wine bottle. The axes ϕ_1 and ϕ_2 are the average values of the corresponding pattern field.

With this particular Lagrangian, the energy is not minimum for $\phi_1 = \phi_2 = 0$, but any value on a circle $\phi_1^2 + \phi_2^2 = R^2$.

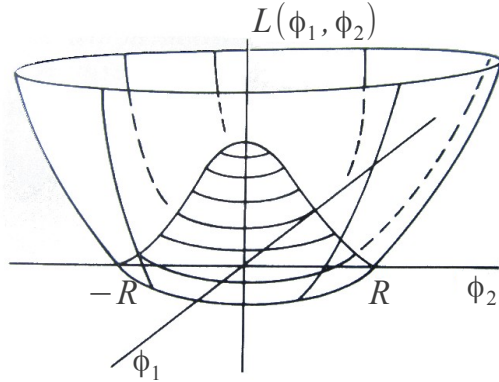


Figure 1.1.: The interaction energy chosen for the two components of the Higgs field. The state of minimum energy corresponds to a non-zero value for the field [1].

Redefining these scalar fields, $(\phi_1, \phi_2) \rightarrow (\phi'_1 = \phi_1, \phi'_2 = \phi_2 - R)$, would keep the Lagrangian conserved and leads to a consequence: the massless boson ϕ'_1 , called the Goldstone boson, is eaten by the massless vector gauge particle A and A becomes massive. The boson ϕ'_2 also acquires mass after the redefinition and is called the Higgs boson.

Now, we apply the above ideas to the electro-weak interactions of the leptons. First, we need four massless gauge vector bosons, of which two are charged for the charged current weak interactions (W^\pm), one is neutral for the weak neutral current (W^0) and one for the electromagnetic current (B). The smallest possible group is then $SU(2) \times U(1)$.

If the symmetry holds, or prior to the spontaneous symmetry breaking, the two components of a left-handed weak isospin doublet are identical except for the I_3^W value, $I_3^W = +1/2$ for the neutrino and $I_3^W = -1/2$ for the left-handed lepton. This latter can be defined as

$$Q = e(I_3^W + Y^W/2) \quad (1.5)$$

where Y^W is called the *weak hypercharge* and has the value $Y^W = -1$ for the left-handed leptons.

Now we require that the interactions of the leptons conserve weak isospin and weak hypercharge, i.e. the Lagrangian be invariant under $SU(2)^W \times U(1)^W$. The $U(1)^W$ of transformation correspond to the shifting of the phases of the lepton wave-functions. Using the same notations as before, we have

$$G^{SU(2)^W \times U(1)^W} \mathcal{L}(l_L, l_R, W^{\pm,0}, B) \rightarrow \mathcal{L}(l_L^*, l_R^*, W^{\pm,0*}, B^*) \quad (1.6)$$

As we have to give mass to three vector bosons ($W^{\pm,0}$) and keep the photon massless, we need to introduce at least four scalar fields: (ϕ^0, ϕ^-) and its antiparticles $(\bar{\phi}^0, \phi^+)$. When the spontaneous symmetry breaking occurs, weak isospin and weak hypercharge are no longer conserved, but their combination forming the electric charge remains

conserved. This means that the U(1) gauge symmetry of QED holds and the photon remains massless. Moreover, the two neutral gauge fields (W^0, B) mix to produce two orthogonal components:

$$A = W^0 \sin \theta_W + B \cos \theta_W \quad (1.7)$$

$$Z^0 = W^0 \cos \theta_W - B \sin \theta_W \quad (1.8)$$

where θ_W is Weinberg angle and $\sin^2 \theta_W = 0.23120 \pm 0.00015$ at $Q = 91.2 \text{ GeV}/c$.

After spontaneous symmetry breaking (SSB), part of the gauge vector bosons get mass by absorbing the scalar fields: W^-, W^+ absorb ϕ^-, ϕ^+ , respectively; Z^0 absorbs a mixture of ϕ^0 and its antiparticle $\bar{\phi}^0$. The remaining of the mixture of ϕ^0 and $\bar{\phi}^0$ creates a scalar massive particle - the Higgs boson. The photon A is left massless. In table 1.2, we have the particles before and after the spontaneous symmetry breaking (SSB). The numbers in the parentheses are the physical degrees of freedom corresponding to the fields. The total physical degrees of freedom before and after SSB is always 12.

Before SSB		After SSB
Φ^- (1), W^- (2)	→	massive W^- (3)
Φ^+ (1), W^+ (2)	→	massive W^+ (3)
Φ^0 (1), $\bar{\Phi}^0$ (1), W^0 (2), B (2)	→	$\left\{ \begin{array}{l} \text{Higgs boson (1)} \\ \text{massive } Z^0 \text{ (3)} \\ \text{massless } A \text{ (2)} \end{array} \right.$

Table 1.2.: The bosons before and after the spontaneous symmetry breaking. In parentheses are the physical degrees of freedom of the particles.

All the bosons generated after SSB in the above table have been discovered.

Quantum Chromodynamics (QCD):

Soon after the introduction of the quarks, one realized that for some combinations of these quarks there is an incompatibility with the Fermi-Dirac statistics. Let us take the example of the Δ^{++} and the Ω^- particles which both belong to the $J^P = 3/2^+$ decuplet: they have half integer spin, hence their total wave function must be antisymmetric.

$$\psi_{total} = \psi_{space} \times \psi_{spin} \times \psi_{flavour} \quad (1.9)$$

As the Δ^{++} and the Ω^- both have three quarks of the same flavour (uuu for the Δ^{++} and sss for the Ω^-), $\psi_{flavour}$ is symmetric, as is ψ_{spin} . As the three quark spins add up to form the particle spin of $3/2$, the orbital momentum of these quarks must be zero and

they should stand is such a way that the space wave function is symmetric. The total wave function is then symmetric which is against the Pauli principle for particles with half integer spin.

The contradiction can be solved if the quarks bear another quantum number which would be different for the otherwise identical quarks. This quantum number is called *colour* and appears as *red*, *green* and *blue* (3 colours) which can be taken as the fundamental representation of a new symmetry group $SU(3)_C$. Group algebra shows that the simplest colour multiplet generated from the fundamental representation (r, g, b) is the colour singlet. All hadrons (mesons and baryons) are thought to be colour singlets:

$$q\bar{q} = \frac{1}{\sqrt{3}}[r\bar{r} + g\bar{g} + b\bar{b}] \quad (1.10)$$

$$qqq = \frac{1}{\sqrt{6}}[(rgb - rbr) + (gbr - grb) + (brg - bgr)] \quad (1.11)$$

Now, we like to have a gauge theory for the colour description of the quark interactions. As for the other theories, we require the local gauge invariance and then need to have vector gauge fields to communicate the local colour convention; these gauge fields are massless and have a spin-1; they are called *gluons* (g). As gluon mediates the interaction between a quark and an antiquark, it should come from the combination of a colour triplet and a anti-colour triplet.

$$3 \times \bar{3} = 1 + 8 \quad (1.12)$$

Indeed, we have eight gluons (colour octet) as $r\bar{b}$, $g\bar{r}$, etc. Bearing colour charges, the gluons can interact therefore among themselves. We note that a photon cannot interact with another photon, but a gluon can interact with another gluon and this has as a consequence the confinement of quarks.

Together, the electroweak theory and the QCD build a beautiful model, the Standard Model, for particle physics:

$$SU(3)_C \otimes SU(2)_L \otimes SU(1)_Y \quad (1.13)$$

The SM is working well at the electroweak scale with its 19 independent parameters:

- ✓ 6 quarks masses, 3 charged lepton masses,
- ✓ 3 gauge couplings (e, θ_W, α_s),
- ✓ 3 Cabibbo mixing angles and the CP-violating Cabibbo-Maki-Nakagawa-Kitabayashi complex phase,
- ✓ the QCD vacuum angle,
- ✓ the Higgs mass and the vacuum expectation value v .

1.2. Limits of the Standard Model and beyond it

Even if we celebrate the triumph of the Standard Model with the discovery of the Higgs-like boson, we still know that the SM remains an incomplete theory.

The absence of the gravity: At the electroweak scale, M_{Z,W^\pm} , where the gravitational force can be neglected, the SM describes well the electromagnetic, weak and strong forces; however, at the Planck scale, $M_P = (8\pi G_{Newton})^{-1/2} = 2.4 \times 10^{18}$ GeV, where quantum gravitational effects become important, how does the SM behave?

The neutrino problem: In the SM, quarks, electrons, muons and taus acquire their masses from gauge invariant terms expressing their interactions with the Higgs field. In this part of the Lagrangian left-handed and right-handed charged leptons are involved. For neutrinos, right-handed neutrinos have never been observed and thus the SM considers that this interaction does not exist. Hence, neutrinos cannot get a mass in the SM. However, the mixing between the neutrino species [4] observed experimentally shows that neutrinos have a non-null mass, even though it is tiny. To describe the neutrino mixing, at least 9 parameters need to be introduced: 3 masses of neutrinos, 3 mixing angles and 3 phases.

The grand unification: The successful unification of two groups $SU(2) \times U(1)$ in the electroweak theory inspired the theoretical physicists to unify them into a larger symmetry group G . Of course, this larger group must be broken at an energy scale (M_{GUT}) which is much higher than the electroweak scale. This is called the Grand Unified Theories (GUT). The simplest GUT theory is the SU(5) symmetry. In this realm, quarks can change to lepton and the proton can decay. However, this simple, non-SUSY SU(5) is now excluded by the non observation of proton decay. Figure 1.2 shows the evolution of the coupling constant in non-SUSY GUTs.

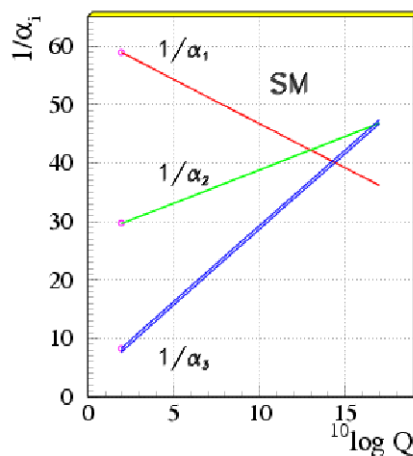


Figure 1.2.: The coupling constants as a function of energy using SM expression; α^{-1} is the inverse of the coupling constants, the horizontal axis scale is the exponent of the energy scale in GeV [11].

The hierarchy problem ([6], [7], [8]): In the electroweak sector of the SM, there is a parameter with energy dimension which sets the scale of all masses in the theory. It is the *vacuum expectation value* of the Higgs field ($v \approx 246$ GeV). For example, the mass of W^\pm is given by

$$m_W = gv/2 \sim 80 \text{ GeV}/c^2 \quad (1.14)$$

where g is the SU(2) gauge coupling constant.

The Higgs boson mass is

$$m_H = v \sqrt{\frac{\lambda}{2}} \quad (1.15)$$

where $\lambda > 0$ is the strength of the Higgs self-interaction in the Higgs potential $V = -\mu^2\phi^\dagger\phi + \frac{\lambda}{4}(\phi^\dagger\phi)^2$, $2\mu^2 = m_H^2$ and ϕ is the SU(2) doublet field. Thus, m_H^2 is roughly in order of $\sim (100\text{GeV})^2$. The newly discovered like-Higgs boson has a mass about 125 GeV/c^2 .

The problem is that m_H^2 receives an enormous quantum correction from the virtual effects of each particle that couples, directly or indirectly, to the Higgs field. Figure 1.3 shows a loop containing a fermion f of mass m_f that couples to Higgs field: the correction is then

$$(\Delta m_H^2)_f = -\frac{|\lambda_f|^2}{16\pi^2} (2\Lambda_{UV}^2 + \dots) \quad (1.16)$$

where Λ_{UV} is an ultraviolet cutoff representing the energy scale at which new physics appears and where the SM must be modified. If Λ_{UV} is of order the Planck mass, then the quantum correction Δm_H^2 is about 30 orders of magnitude larger than the expected value of m_H^2 . This is known as *hierarchy problem*, which is a big challenge of the SM.

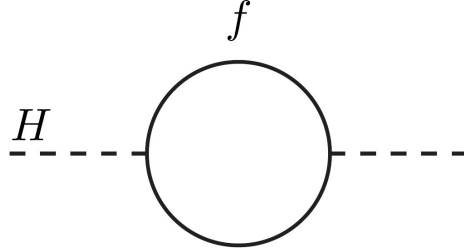


Figure 1.3.: The loop containing a Dirac fermion f that couples to Higgs field [6].

Connection to Cosmology [5]: In Cosmology, the distribution of matter in galaxies can be determined via the orbital velocities and radius of its objects with Kepler's law

$$V = \sqrt{\frac{GM(R)}{R}} \quad (1.17)$$

For luminous matter (stars, dust, gas), the matter density can be measured via the disk surface brightness by assuming that this brightness is proportional to the surface density of luminous matter. The surprise is that the radial velocity distribution levels at a value which is quite higher than the one expected from Newtonian physics based on the observed luminous matter. For example, in the Milky Way, the luminous matter velocity is one tenth of the observed velocity. Figure 1.4 presents the results of the measurement for the galaxy M33. What kind of matter is this mass excess? Nowadays, a part of this mass is believed to belong to the black holes in the centre of the galaxies. However the observed curve in figure 1.4 shows that the velocity stays constant from near 5 kpc; this means that the mass $M(R)$ is proportional to the radius R and that the unknown matter must be distributed everywhere in the galaxies. This unknown matter is called *dark matter*. Recent observations of gravitational lensing effects by the Hubble Space Telescope also provide evidences for it.

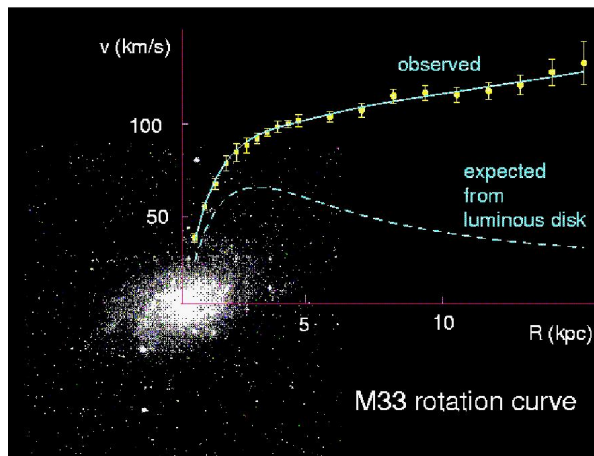


Figure 1.4.: The velocities as a function of radius are measured using Kepler's law and for the luminous matter for the galaxy M33.

Today, it is believed that roughly 27% of the Universe is dark matter, the normal matter accounting for about 5%. This dark matter is believed to be non baryonic and thus do not belong to the Standard Model. If it were baryonic, we would be able to detect it by its absorption of radiation passing through it. The most common view is that the dark matter is make up of some particles which are Weakly Interacting Massive Particles (WIMPs).

An other point about cosmology is the fact that the amount of baryons over photons is $(4 \pm 1) \cdot 10^{-10}$. This value can be reproduced in many Grand Unified Theories but using only the quark sector CP violation of SM, one predicts that only one proton is left for 10^{18} protons, which is way off: the needed CP violation requires new physics beyond the Standard Model.

Chapter 2.

Supersymmetry

The Standard Model needs to be extended to correct its limits. One of the most plausible extensions are Supersymmetry theories [6], [7], [8], [9], [10]. In this chapter, we will concentrate on discussing about these theories. First, we will introduce to the Supersymmetry in section 2.1, then we will see the construction of its Lagrangian in section 2.2. After that, the content of the Minimal Supersymmetric Standard Model will be presented in section 2.3. Finally, we focus on one of the SUSY versions, the minimal Gauge Mediated Supersymmetry Breaking (mGMSB) model, which contains the stau particle ($\tilde{\tau}$) that we will study in this thesis (section 2.4).

2.1. Introduction to Supersymmetry

Back to the hierarchy problem, we know that the contribution from a fermion to the Higgs mass correction is expressed by equation 1.16 and the problem comes from the Λ_{UV} .

Suppose now that there is a scalar particle S with mass m_S which also couples to Higgs boson as shown in figure 2.1(b), then the correction from this particle to the Higgs mass is

$$(\Delta m_H^2)_S = \frac{|\lambda_S|}{16\pi^2} (\Lambda_{UV}^2 + \dots) \quad (2.1)$$

From equations 1.16 and 2.1, we can see that if $\lambda_S = |\lambda_f|^2$ and if each of the particle of the Standard Model is accompanied by a partner whose spin differ by half a unit from the one of the original particle, then the Λ_{UV}^2 contributions to the Higgs mass in figure 2.1 will be neatly cancelled. This suggests that a symmetry between fermion and boson might be a good solution for the "hierarchy problem". This symmetry is called *Supersymmetry* and abbreviated as SUSY.

In supersymmetric theories, a supersymmetric operator Q is introduced in order to allow to change a fermionic state into a bosonic state and vice versa; in other words, this operator changes the spin of particle, the other quantum numbers being maintained.

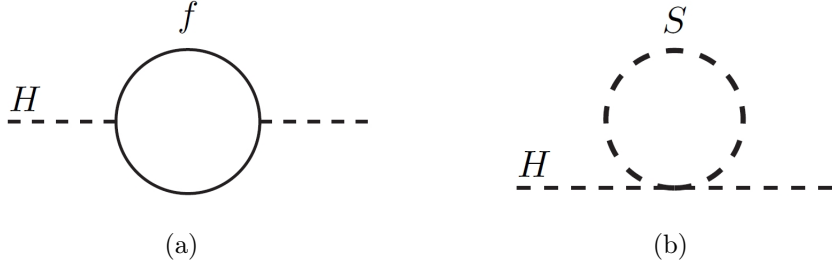


Figure 2.1.: Feynman diagrams presenting the contributions to the Higgs mass from fermion in (a) and from boson in (b) [6].

$$Q|Boson\rangle = |Fermion\rangle, \quad Q|Fermion\rangle = |Boson\rangle \quad (2.2)$$

Particles in the same supersymmetry multiplet, called *supermultiplet*, have the same gauge transformation properties (electric charge, weak isospin, colour,...). Each supermultiplet contains both fermion and boson states whose degrees of freedom are equal.

$$n_B = n_F \quad (2.3)$$

The two simplest ways to combine particles according to equation 2.3 are:

- A supermultiplet containing a single Weyl fermion with two spin states, i.e. $n_F = 2$, has to contain two real scalars, i.e. $n_B = 2$. The two real scalar degrees of freedom can be assembled into a complex scalar field. Then, one can combine the two-component Weyl fermion and the complex scalar field into a *chiral* supermultiplet.
- For a multiplet containing a spin-1 gauge boson, this boson is massless before the gauge symmetry breaking, it has two helicity states, i.e. $n_B = 2$. The superpartner of this boson is a Weyl fermion of spin-1/2 which has two helicity states, i.e. $n_F = 2$. These fermionic partners are called *gauginos*. The combination of gauginos and gauge boson is called *gauge* supermultiplet.

If we include gravity, the spin-2 graviton (with 2 helicity states, $n_B = 2$) will have a spin-3/2 superpartner called the *gravitino*. The graviton and gravitino would be massless if supersymmetry were unbroken.

Each particle of spin σ in the Standard Model belongs to either chiral or gauge supermultiplet and has a *superpartner* of spin $\sigma \pm \frac{1}{2}$.

A fermion (quarks and leptons) of the Standard Model has to belong to a chiral supermultiplet. Its bosonic superpartners are prefixed by an *s*, for scalar; so they are called *sfermion* (or *squarks*, *sleptons*). The symbol for a SM particle and its superpartner is the same, but with a tilde (\sim) for the superpartner. For example,

the superpartners of the left-handed and right-handed electrons (e_L, e_R) are the left-handed and right-handed *selectrons* (\tilde{e}_L, \tilde{e}_R). However, the handedness here does not refer to the helicity of selectrons because they have spin-0, but to the handedness of their superpartners. Neutrinos of the Standard Model are only left-handed, so their superpartners are symbolized by $\tilde{\nu}$ or with the subscript $\tilde{\nu}_e, \tilde{\nu}_\mu, \tilde{\nu}_\tau$ to indicate their flavours.

The Higgs boson of the Standard Model should be considered as the complex scalar component of a chiral supermultiplet since it has spin-0, its superpartners are fermions and are called *Higgsinos*. In the Standard Model, the Higgs boson can be chosen with hypercharge of $Y = \pm 1$, so that the Higgsino can also take a hypercharge of $Y = \pm 1$. Two chiral supermultiplets are introduced, each of which has one of $Y = \pm 1$. Furthermore, we will see that in SUSY theories, only the Higgs chiral supermultiplet of $Y = +1$ can give masses to quarks of $+2/3$ charge (u, c, t) and only one of $Y = -1$ can give masses to quarks of $-1/3$ charge (d, s, b) and to the charged leptons. For this reason, we denote the complex scalar fields with $Y = +1$ and $Y = -1$ by H_u and H_d respectively. Since the third component of weak isospin of each Higgs particle has two values ($\pm 1/2$), the H_u has therefore two electric charges (1, 0) and denoted by H_u^+ and H_u^0 . Similarly, H_d has two charges (0, -1) and symbolized by H_d^0 and H_d^- . The symbols corresponding to Higgsino are $\tilde{H}_u, \tilde{H}_d, \tilde{H}_u^+, \tilde{H}_u^0, \tilde{H}_d^0, \tilde{H}_d^-$. The chiral supermultiplets in the Minimal Supersymmetric Standard Model are shown in table 2.1.

Names	Symbol	spin-0	spin-1/2	$SU(3)_C, SU(2)_L, U(1)_Y$
squark, quarks ($\times 3$ families)	Q	$(\tilde{u}_L, \tilde{d}_L)$	(u_L, d_L)	$(3, 2, 1/3)$
	\bar{u}	\tilde{u}_R^*	u_R^\dagger	$(\bar{3}, 1, -4/3)$
	\bar{d}	\tilde{d}_R^*	d_R^\dagger	$(\bar{3}, 1, -2/3)$
slepton, leptons ($\times 3$ families)	L	$(\tilde{\nu}, \tilde{e}_L)$	(ν, e_L)	$(1, 2, -1)$
	\bar{e}	\tilde{e}_R^*	e_R^\dagger	$(1, 1, 1/2)$
Higgs, higgsinos	H_u	(H_u^+, H_u^0)	$(\tilde{H}_u^+, \tilde{H}_u^0)$	$(1, 2, +1)$
	H_d	(H_d^0, H_d^-)	$(\tilde{H}_d^0, \tilde{H}_d^-)$	$(1, 2, -1)$

Table 2.1.: Chiral supermultiplets in the Minimal Supersymmetric Standard Model.

Back to the gauge supermultiplets, the bosons of the Standard Model have superpartners suffixed by *-ino*; for example, the *gluon*'s superpartner is the *gluino* (\tilde{g}). For the bosons in the electroweak gauge symmetry (W^+, W^-, W^0 and B^0), the superpartners are the *winos* ($\tilde{W}^+, \tilde{W}^-, \tilde{W}^0$) and the *bino* (\tilde{B}^0). After electroweak symmetry breaking, the W^0 and B^0 gauge eigenstates mix to give mass eigenstates Z^0 and γ . Similarly, the \tilde{W}^0 and \tilde{B}^0 also mix to create *zino* (\tilde{Z}^0) and *photino* ($\tilde{\gamma}$). The gauge supermultiplets in the Minimal Supersymmetric Standard Model are presented in table 2.2.

Names	spin-1/2	spin-1	$SU(3)_C, SU(2)_L, U(1)_Y$
gluino, gluon	\tilde{g}	g	(8, 1, 0)
winos, W bosons	$\widetilde{W}^\pm, \widetilde{W}^0$	W^\pm, W^0	(1, 3, 0)
bino, B boson	\widetilde{B}^0	B^0	(1, 1, 0)

Table 2.2.: Gauge supermultiplets in the Minimal Supersymmetric Standard Model.

However, the most noticeable point of this theory is that none of the superparticles has been found. If supersymmetry was unbroken, then the superparticles would have the same mass as their Standard Model partners. For example, selectrons \tilde{e}_L and \tilde{e}_R would have masses exactly equal to $m_e = 0.511 \text{ MeV}/c^2$, gluino and photino are massless, etc... Therefore, these superparticles would have been discovered a long time ago. The unique explanation for this conflict is that supersymmetry was broken.

Assuming that SUSY still provides a solution to the hierarchy problem even in the presence of supersymmetry breaking, i.e. that the quadratic divergences must be systematically cancelled, the relationship $\lambda_S = |\lambda_f|^2$ must be preserved. We are hence led to consider *soft supersymmetry breaking*. A soft supersymmetry breaking term will be added into the Lagrangian, which will break supersymmetry, but only "softly", this adverb means that the modification of the Lagrangian at high energy is so small that no new divergent contribution to the mass of a scalar is added. The Lagrangian can be written

$$\mathcal{L} = \mathcal{L}_{susy} + \mathcal{L}_{soft} \quad (2.4)$$

where \mathcal{L}_{susy} contains all of the gauge and Yukawa interactions and preserves supersymmetry invariance, \mathcal{L}_{soft} only contains mass terms and couplings with positive mass dimension. If m_{soft} is the largest mass scale present in \mathcal{L}_{soft} , the corrections to the Higgs mass arising from \mathcal{L}_{soft} must vanish when $m_{soft} \rightarrow 0$, so they cannot grow as Λ^2 . Additionally, the UV divergences are either quadratic or logarithmic, hence these corrections must be of the form

$$\Delta m_H^2 \sim \lambda m_{soft}^2 \ln\left(\frac{\Lambda}{m_{soft}}\right) \quad (2.5)$$

Furthermore, within a supermultiplet we have $m_{soft}^2 \sim (m_B^2 - m_F^2)$. We would like that Δm_H should be less than or approximately equal to m_H , therefore we deduce

$$m_B^2 - m_F^2 \lesssim (1 \text{ TeV})^2 \quad (2.6)$$

Equation 2.6 motivates that the masses of superparticles are less than about $1 \text{ TeV}/c^2$. Therefore, we can hope they can be produced and detected at LHC.

2.2. Supersymmetric Lagrangian

In this section, we will present the general recipe to construct the Lagrangian for the supersymmetric theories with soft supersymmetry breaking. In section 2.1 we showed that we have the chiral and gauge supermultiplets, we will therefore consider in turn the Lagrangian for the free chiral supermultiplet (i.e. no masses, no interactions are included), for interacting chiral supermultiplet and for gauge supermultiplet. Then, the total Lagrangian of the supersymmetry theory is the sum of these Lagrangian components.

2.2.1. Lagrangian of the chiral supermultiplet

Free chiral supermultiplet

We start to consider a simplest chiral supermultiplet that contains a single left-handed two component Weyl fermion ψ_α and its superpartner, a complex scalar ϕ . The simplest action which consists of kinetic energy terms of these fields (no masses, no interactions) is

$$S = \int d^4x (\mathcal{L}_s + \mathcal{L}_f) \quad (2.7)$$

$$\mathcal{L}_s = -\partial^\mu \phi^* \partial_\mu \phi, \quad \mathcal{L}_f = i\psi^\dagger \bar{\sigma}^\mu \partial_\mu \psi \quad (2.8)$$

where $\partial_\mu = (\partial/\partial t, \vec{\nabla})$, $\partial^\mu = (\partial/\partial t, -\vec{\nabla})$ are the covariant and contravariant derivatives; ϕ^* is the complex conjugate of ϕ and ψ^\dagger is the Hermitian conjugate of ψ ; $\bar{\sigma}^\mu$ are the transposed matrices of the Pauli matrices σ^μ .

Since a supersymmetric transformation should turn the scalar boson field ϕ into the fermion field ψ , we have the following possibilities.

$$\delta\phi = \epsilon\psi, \quad \delta\phi^* = \epsilon^\dagger\psi^\dagger \quad (2.9)$$

where ϵ is an infinitesimal, anticommuting, two component Weyl fermion object which parametrises the transformation. Since ψ has dimension of [mass]^{3/2} and ϕ has dimension of [mass], ϵ has therefore dimension of [mass]^{-1/2}. As we discuss about global supersymmetry, we have $\partial_\mu\epsilon^\alpha = 0$ as ϵ^α is a constant.

$$\delta\mathcal{L}_s = -\epsilon\partial^\mu\psi\partial_\mu\phi^* - \epsilon^\dagger\partial^\mu\psi^\dagger\partial_\mu\phi \quad (2.10)$$

We would like that this $\delta\mathcal{L}_s$ is cancelled by $\delta\mathcal{L}_f$, so that the action S is invariant under the SUSY transformation. For this and from equation 2.10, we see that $\delta\psi$ should be linear in ϵ^\dagger and in ϕ , and must contain one space-time derivative. The only possibility is

$$\delta\psi_\alpha = -i(\sigma^\mu\epsilon^\dagger)_\alpha\partial_\mu\phi, \quad \delta\psi_{\dot{\alpha}}^\dagger = i(\epsilon\sigma^\mu)_{\dot{\alpha}}\partial_\mu\phi^* \quad (2.11)$$

where $\dot{\alpha} = 1, 2$ is the spinor index of the right-handed Weyl spinor $\psi_{\dot{\alpha}}^\dagger$ -the hermitian conjugate of the left-handed Weyl spinor. Using equation 2.11, we obtain

$$\delta\mathcal{L}_f = -\epsilon\sigma^\mu\bar{\sigma}^\nu\partial_\nu\psi\partial_\mu\phi^* + \psi^\dagger\bar{\sigma}^\nu\sigma^\mu\epsilon^\dagger\partial_\mu\partial_\nu\phi \quad (2.12)$$

Using the following relations:

$$[\sigma^\mu\bar{\sigma}^\nu + \sigma^\nu\bar{\sigma}^\mu]_\alpha^\beta = -2\eta^{\mu\nu}\delta_\alpha^\beta \quad (2.13)$$

$$[\bar{\sigma}^\mu\sigma^\nu + \bar{\sigma}^\nu\sigma^\mu]_{\dot{\alpha}}^{\dot{\beta}} = -2\eta^{\mu\nu}\delta_{\dot{\alpha}}^{\dot{\beta}} \quad (2.14)$$

$$\partial_\mu\partial_\nu = \partial_\nu\partial_\mu \quad (2.15)$$

where $\eta_{\mu\nu} = \text{diag}(-1, +1, +1, +1)$ is the space-time metric.

we can write again the equation 2.12 as

$$\begin{aligned} \delta\mathcal{L}_f = & \epsilon\partial^\mu\psi\partial_\mu\phi^* + \epsilon^\dagger\partial^\mu\psi^\dagger\partial_\mu\phi \\ & -\partial_\mu(\epsilon\sigma^\nu\bar{\sigma}^\mu\psi\partial_\nu\phi^* + \epsilon\psi\partial^\mu\phi^* + \epsilon^\dagger\psi^\dagger\partial^\mu\phi) \end{aligned} \quad (2.16)$$

The first two terms cancel against $\delta\mathcal{L}_s$ and the rest is total derivative, we therefore arrive at

$$\delta S = \int d^4x(\delta\mathcal{L}_s + \delta\mathcal{L}_f) = 0 \quad (2.17)$$

However, equation 2.17 is not enough to declare that the theory described by equation 2.8 is supersymmetric. It is still necessary that the supersymmetry algebra closes, this means that the commutator of two SUSY transformations parametrized by two different spinors ϵ_1, ϵ_2 is also a symmetry operation. For scalar fields, we find

$$(\delta_{\epsilon_2}\delta_{\epsilon_1} - \delta_{\epsilon_1}\delta_{\epsilon_2})\phi \equiv \delta_{\epsilon_2}(\delta_{\epsilon_1}\phi) - \delta_{\epsilon_1}(\delta_{\epsilon_2}\phi) = i(-\epsilon_1\sigma^\mu\epsilon_2^\dagger + \epsilon_2\sigma^\mu\epsilon_1^\dagger)\partial_\mu\phi \quad (2.18)$$

We have got $i\partial_\mu$ which is nothing but the four-momentum operator P_μ , the operator of space-time translation, a symmetry of space-time. For fermion fields, we get

$$\begin{aligned} (\delta_{\epsilon_2}\delta_{\epsilon_1} - \delta_{\epsilon_1}\delta_{\epsilon_2})\psi_\alpha = & i(-\epsilon_1\sigma^\mu\epsilon_2^\dagger + \epsilon_2\sigma^\mu\epsilon_1^\dagger)\partial_\mu\psi_\alpha \\ & + i\epsilon_{1\alpha}\epsilon_2^\dagger\bar{\sigma}^\mu\partial_\mu\psi - i\epsilon_{2\alpha}\epsilon_1^\dagger\bar{\sigma}^\mu\partial_\mu\psi \end{aligned} \quad (2.19)$$

The first term of the equation 2.19 is similar to what we got for scalar field ϕ in equation 2.18, but the two last terms only vanish on-shell, i.e. when the classical equations of motion $\bar{\sigma}^\mu\partial_\mu\psi = 0$ are satisfied. But we want also SUSY to be a valid symmetry even off-shell. To solve this problem, we will use a trick and introduce a bosonic spin-0 field which does not have any kinetic term and is called *auxiliary field* F . The F field has dimension [mass]² and does not affect the dynamic classically or in the quantum theory.

From equation 2.19, we see that in order to cancel the two last terms the transformation of F field should be:

$$\delta F = -i\epsilon^\dagger \bar{\sigma}^\mu \partial_\mu \psi \quad (2.20)$$

Then, SUSY transformation law for fermion field ψ will become:

$$\delta\psi_\alpha = -i(\sigma^\mu \epsilon^\dagger)_\alpha \partial_\mu \phi + \epsilon_\alpha F \quad (2.21)$$

and this lead the commutator in equation 2.19 to become a symmetry operation for on-shell as well as for off-shell.

Let us now count the fermionic and bosonic degrees of freedom. We recall that for SUSY we must have $n_F = n_B$. On shell, the complex scalar field has two real components, i.e. $n_F = 2$ degrees of freedom which match the two spin polarization states of ψ . When we go off-shell, the Weyl fermion ψ is a complex two-component spinor and has $n_f = 4$ degrees of freedom. To have the same fermionic and bosonic number of degrees of freedom, the introduction of the scalar auxiliary field is necessary. We have then ϕ which is a complex scalar field with $n_B = 2$ and the auxiliary field F which is also a complex scalar with $n_B = 2$. The counting rule $n_F = n_B$ is then preserved off shell by the introduction of this auxiliary field.

This does not harm when we are on shell as the Lagrangian for this auxiliary field is

$$\mathcal{L}_{\text{aux}} = F^* F \quad (2.22)$$

and the equation of motion is $F = F^* = 0$: the auxiliary field vanishes on shell.

For a free, massless chiral supermultiplet, we finally obtain the total Lagrangian that is invariant under SUSY transformations expressed by equations 2.9, 2.20 and 2.21.

$$\begin{aligned} \mathcal{L}_{\text{free}} &= \mathcal{L}_s + \mathcal{L}_f + \mathcal{L}_{\text{aux}} \\ &= -\partial^\mu \phi^* \partial_\mu \phi + i\psi^\dagger \bar{\sigma}^\mu \partial_\mu \psi + F^* F \end{aligned} \quad (2.23)$$

By proceeding as before, we also obtain:

$$(\delta_{\epsilon_2} \delta_{\epsilon_1} - \delta_{\epsilon_1} \delta_{\epsilon_2}) X \equiv \delta_{\epsilon_2}(\delta_{\epsilon_1} X) - \delta_{\epsilon_1}(\delta_{\epsilon_2} X) = i(-\epsilon_1 \sigma^\mu \epsilon_2^\dagger + \epsilon_2 \sigma^\mu \epsilon_1^\dagger) \partial_\mu X \quad (2.24)$$

for each of $X = \phi, \phi^*, \psi, \psi^\dagger, F, F^*$. That means that the modified SUSY theory closes off-shell as well as on-shell.

Interacting chiral supermultiplets

In the previous paragraph, we constructed a Lagrangian which is invariant under SUSY transformations for the free, massless chiral supermultiplets ($\mathcal{L}_{\text{free}}$), i.e. the masses and

the interaction were not included in this Lagrangian. In this paragraph, we will construct a Lagrangian for interacting chiral supermultiplets (\mathcal{L}_{int}) which still preserve SUSY invariance.

To begin, we note that the terms of the Lagrangian must be renormalizable, so each term has a field content with total mass dimension ≤ 4 . Additionally, this interacting Lagrangian must be invariant under the SUSY transformations (equations 2.9, 2.20 and 2.21) as the free Lagrangian $\mathcal{L}_{\text{free}}$ is already invariant. So, the plausible Lagrangian is

$$\mathcal{L}_{\text{int}} = \left(-\frac{1}{2} W^{ij} \psi_i \psi_j + W^i F_i \right) + \text{h.c.} \quad (2.25)$$

where W^{ij} and W^i are polynomials in the scalar fields ϕ_i , ϕ^{*i} and have the degrees number of 1 and of 2, respectively since $[\phi] = m$, $[F] = m^2$ and $[\psi] = m^{3/2}$; and W^{ij} and W^i satisfy the following relations:

$$W^i = \frac{\partial W}{\partial \phi_i}, \quad W^{ij} = \frac{\partial^2 W}{\partial \phi_i \partial \phi_j} \quad (2.26)$$

The most general normalisable supersymmetric form is:

$$W = \frac{1}{2} M^{ij} \phi_i \phi_j + \frac{1}{6} y^{ijk} \phi_i \phi_j \phi_k \quad (2.27)$$

and is called *superpotential*. Here, M^{ij} is a symmetric mass matrix and y^{ijk} are couplings.

Linear terms $L_i \phi_i$ are also possible when ϕ_i is a gauge singlet, but there is no gauge singlet in MSSM, so we will omit them.

The equations of motion for the auxiliary fields are

$$F_i = -W_i^*, \quad F^{*i} = -W^i \quad (2.28)$$

From the superpotential, a scalar potential can be determined:

$$\begin{aligned} V(\phi, \phi^*) &= W^k W_k^* = F^{*k} F_k \\ &= M_{ik}^* M^{kj} \phi^{*i} \phi_j \\ &\quad + \frac{1}{2} M^{in} y_{jkn}^* \phi_i \phi^{*j} \phi^{*k} + \frac{1}{2} M_{in}^* y^{jkn} \phi^{*i} \phi_j \phi_k \\ &\quad + \frac{1}{4} y^{ijn} y_{kln}^* \phi_i \phi_j \phi^{*k} \phi^{*l} \end{aligned} \quad (2.29)$$

In the above paragraphs, we constructed the free and interacting Lagrangians (eq 2.23, 2.25) in a chiral supermultiplet. The total Lagrangian of a chiral supermultiplet is now the sum of these components.

$$\begin{aligned}
\mathcal{L}_{\text{chiral}} &= \mathcal{L}_{\text{free}} + \mathcal{L}_{\text{int}} \\
&= -\partial^\mu \phi^{*i} \partial_\mu \phi_i + i\psi^{\dagger i} \bar{\sigma}^\mu \partial_\mu \psi_i + F^* F \\
&\quad - \frac{1}{2} (W^{ij} \psi_i \psi_j + W_{ij}^* \psi^{\dagger i} \psi^{\dagger j}) + \text{h.c}
\end{aligned} \tag{2.30}$$

The superpotential can be put into the Lagrangian to get the full Lagrangian density from which we can drive from the equation of motions that fermions and bosons do have the same mass.

2.2.2. Lagrangian of the gauge supermultiplet

As said in the introduction, a gauge supermultiplet contains a gauge boson A_μ^a and a gaugino λ^a , where the index a runs over the gauge group generator: $a = 1, 2, \dots, 8$ for $SU(3)_C$; $a = 1, 2, 3$ for $SU(2)_L$ and $a = 1$ for $U(1)_Y$. The Lagrangian for the gauge supermultiplet is

$$\mathcal{L}_{\text{gauge}} = -\frac{1}{4} F_{\mu\nu}^a F^{\mu\nu a} + i\lambda^{\dagger a} \bar{\sigma}^\mu D_\mu \lambda^a + \frac{1}{2} D^a D^a \tag{2.31}$$

where the field strength $F_{\mu\nu}^a$ and the covariant derivative of the gaugino are defined as:

$$F_{\mu\nu}^a = \partial_\mu A_\nu^a - \partial_\nu A_\mu^a + g f^{abc} A_\mu^b A_\nu^c \tag{2.32}$$

$$D_\mu \lambda^a = \partial_\mu \lambda^a + g f^{abc} A_\mu^b \lambda^c \tag{2.33}$$

D^a is a real bosonic auxiliary field which is introduced in order for the supersymmetry to be a valid symmetry off-shell: like chiral auxiliary field F , the gauge auxiliary field also has dimension of [mass]² and no kinetic term so that it can be eliminated on-shell using its equation of motion.

The gauge transformations of fields in the gauge supermultiplet are

$$\delta A_\mu^a = -\frac{1}{\sqrt{2}} (\epsilon^\dagger \bar{\sigma}_\mu \lambda^a + \lambda^{\dagger a} \bar{\sigma}_\mu \epsilon) \tag{2.34}$$

$$\delta \lambda_\alpha^a = \frac{i}{2\sqrt{2}} (\sigma^\mu \bar{\sigma}^\nu \epsilon)_\alpha F_{\mu\nu}^a + \frac{1}{\sqrt{2}} \epsilon_\alpha D^a \tag{2.35}$$

$$\delta D^a = \frac{i}{\sqrt{2}} (-\epsilon^\dagger \bar{\sigma}^\mu D_\mu \lambda^a + D_\mu \lambda^{\dagger a} \bar{\sigma}^\mu \epsilon) \tag{2.36}$$

Using these SUSY transformation laws, we can show that the supersymmetry algebra for the fields of the gauge supermultiplets closes on-and off shell thanks to the auxiliary field D^a .

2.2.3. Lagrangian of the supersymmetric gauge interactions

We finally consider the general Lagrangian density for a supersymmetry theory with both chiral and gauge supermultiplets $X_i = \phi_i, \psi_i, F_i$. As SUSY and gauge groups commute, all the fields X_i must transform according to the same representation of the gauge group, with generator T^a :

$$\delta_{\text{gauge}} X_i = ig\lambda^a(T^a X)_i \quad (2.37)$$

To have a gauge invariant Lagrangian, the ordinary derivatives must first be turned into covariant ones everywhere.

$$\partial_\mu \phi_i \rightarrow D_\mu \phi_i = \partial_\mu \phi_i - igA_\mu^a(T^a \phi)_i \quad (2.38)$$

$$\partial_\mu \psi_i \rightarrow D_\mu \psi_i = \partial_\mu \psi_i - igA_\mu^a(T^a \psi)_i \quad (2.39)$$

Then, one needs to add the other possible interactions between the fields in the chiral and gauge supermultiplets. In fact, there are three such interactions between the fields ϕ, ψ, λ^a and D^a ; these three interactions are expressed by the three last terms in the Lagrangian of the supersymmetry theory.

$$\mathcal{L} = \mathcal{L}_{\text{chiral}} + \mathcal{L}_{\text{gauge}} - \sqrt{2}g(\phi^* T^a \psi)\lambda^a - \sqrt{2}g\lambda^{\dagger a}(\psi^\dagger T^a \phi) + g(\phi^* T^a \phi)D^a \quad (2.40)$$

This Lagrangian is SUSY invariant, provided that the superpotential is gauge invariant:

$$\delta_{\text{gauge}} W = \frac{\partial W}{\partial \phi_i} \delta \phi_i = W_i(T^a)_{ij} \phi_j = 0 \quad (2.41)$$

The equations of motion of D^a are now:

$$D^a = -g(\phi^* T^a \phi) \quad (2.42)$$

and the scalar potential:

$$V(\phi, \phi^*) = F^{*i} F_i + \frac{1}{2} \sum_a D^a D^a \quad (2.43)$$

and is completely determined by the auxiliary fields. The terms $F^{*i} F_i$ and $\sum_a D^a D^a$ are referred to as the F -term and the D -term.

2.2.4. Soft supersymmetry breaking

As mentioned in 2.1, the supersymmetry breaking should be soft for the solution of the hierarchy problem. The supersymmetry breaking Lagrangian would contain the

only mass terms and coupling parameters with positive mass dimension. The possible Lagrangian is

$$\mathcal{L}_{\text{soft}} = -\left(\frac{1}{2}M_a\lambda^a\lambda^a + \frac{1}{6}a^{ijk}\phi_i\phi_j\phi_k + \frac{1}{2}b^{ij}\phi_i\phi_j\right) + h.c - (m^2)_j^i\phi^{j*}\phi_i \quad (2.44)$$

where M_a is gaugino masses with $a = 1, 2, 3$; $(m^2)_j^i$ and b^{ij} are scalar squared-mass terms; a^{ijk} are couplings. It can be shown that $\mathcal{L}_{\text{soft}}$ (2.44) is free of quadratic divergence in quantum correction for scalar masses to all orders in perturbation theories.

2.3. The Minimal Supersymmetric Standard Model

2.3.1. Grand Unification in MSSM

Before presenting in some detail the Minimal Supersymmetric Standard Model, we would like to come back to the unification of the interactions and show that a Minimal Supersymmetric Standard Model (MSSM) would do the job. We define the coupling strength of the SM interactions as:

$$\alpha_1 = \frac{5}{3} \frac{1}{4\pi} g'^2, \quad \alpha_2 = \frac{1}{4\pi} g^2, \quad \alpha_3 = \frac{1}{4\pi} g_s^2 \quad (2.45)$$

The one-loop renormalization group equations for gauge couplings are

$$\frac{d\alpha_i}{d \log Q} = -\frac{b_i}{2\pi} \alpha_i^2 \quad (2.46)$$

where $\alpha_i = g_i^2/(4\pi)$ with $i = 1, 2, 3$; and Q is a "running" energy scale and b_i are constants. The solution of equation 2.46 is

$$\alpha_i^{-1}(Q) = \alpha_i^{-1}(Q_0) - \frac{b_i}{2\pi} \log\left(\frac{Q}{Q_0}\right) \quad (2.47)$$

where Q_0 is the scale at which the running begins.

Suppose that the three gauge coupling constants of the Standard Model are unified at some energy Q_U , then the coupling constants are equal:

$$\alpha_1^{-1}(Q_U) = \alpha_2^{-1}(Q_U) = \alpha_3^{-1}(Q_U) \quad (2.48)$$

Using equation 2.47 and 2.48, we obtain the relation

$$\alpha_3^{-1}(Q_0) = (1 + B)\alpha_2^{-1}(Q_0) - B\alpha_1^{-1}(Q_0) \quad (2.49)$$

where

$$B = \frac{b_3 - b_2}{b_2 - b_1} \quad (2.50)$$

The values of the $\alpha_i^{-1}(Q_0)$ have been measured very accurately at $Q_0 = m_Z$: $\alpha_3^{-1}(m_Z) = 8.5$, $\alpha_2^{-1}(m_Z) = 29.57$, $\alpha_1^{-1}(m_Z) = 59.00$. Then, one can deduce

$$B = 0.716 \quad (2.51)$$

We can now compare the value of B (Eq. 2.51) to values obtained by equation 2.50 using different models. The model that gives the B value consistent with equation 2.51 will be accepted as the one that can do the grand unification. In the minimal Standard Model, the values of the b_i are

$$\begin{aligned} b_3 &= 11 - \frac{4}{3}n_g \\ b_2 &= \frac{22}{3} - \frac{4}{3}n_g - \frac{1}{6}n_h \\ b_1 &= -\frac{4}{3}n_g - \frac{1}{10}n_h \end{aligned} \quad (2.52)$$

where n_g is the number of generations, n_h is the number of Higgs doublets. For the minimal case, $n_h = 1$, we obtain $B = 0.53$ which is very poor agreement with 2.51, this minimal Standard Model is therefore considered as having failed.

In MSSM, $n_h = 2$, we get $B = 0.714$. This value is in good agreement with equation 2.51. Using equation 2.47, we easily find the unification scale $Q_U \simeq 2.2 \times 10^{16}$ GeV. Figure 2.2 shows the running of the three coupling constants $\alpha_i^{-1}(Q)$ as a function of $\log Q$ in the SM and in the MSSM.

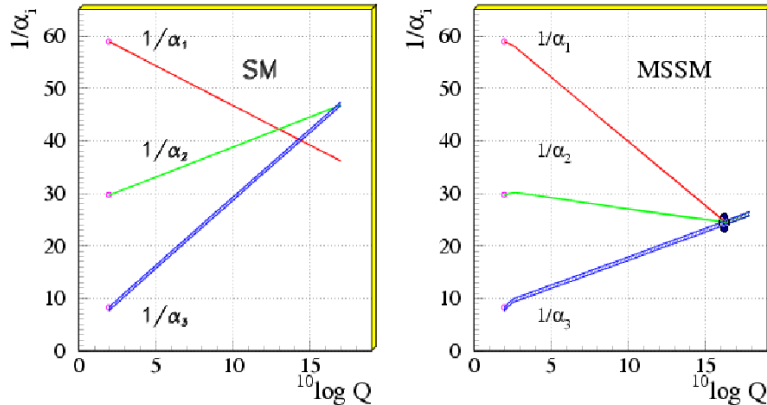


Figure 2.2.: The coupling constants as a function of $\log Q$ in the SM and in the MSSM; where α_i^{-1} is the inverse of the coupling constants, the index $i = 1, 2, 3$ [11].

2.3.2. Superpotential in MSSM

In the section 2.2, we showed the recipe for constructing the Lagrangians for the supersymmetry theories with soft supersymmetry breaking. In this section, we will apply these general results to the Minimal Supersymmetric Standard Model. By using equation 2.27, we can now write the superpotential of the MSSM.

$$W_{MSSM} = \bar{u} \mathbf{y}_u Q H_u - \bar{d} \mathbf{y}_d Q H_d - \bar{e} \mathbf{y}_e L H_d + \mu H_u H_d \quad (2.53)$$

where H_u , H_d , Q , L , \bar{u} , \bar{d} , \bar{e} are chiral superfields corresponding to the ones in table 2.1. The dimensionless Yukawa coupling parameters \mathbf{y}_u , \mathbf{y}_d , \mathbf{y}_e are 3×3 matrices. These couplings give masses to the quarks and leptons when the Higgs field acquire Vacuum Expectation Value (VEV). The μ term is the supersymmetric version of the Higgs boson mass in the Standard Model. We see no presence of mass terms for fermions in the superpotential because they would explicitly break the $SU(2)_L$ gauge symmetry. In equation 2.53, all the indices of family ($i, j = 1, 2, 3$), of gauge $SU(3)_C$ colour ($a = 1, 2, 3$) and of gauge $SU(2)_L$ weak isospin ($\alpha, \beta = 1, 2$) have been suppressed. For example, the term $\bar{u} \mathbf{y}_u Q H_u$ can be explicitly written out as $\bar{u}^{ia} (\mathbf{y}_u)_i^j Q_{j\alpha a} (H_u)_\beta \epsilon^{\alpha\beta}$ and $\mu H_u H_d$ as $\mu (H_u)_\alpha (H_d)_\beta \epsilon^{\alpha\beta}$.

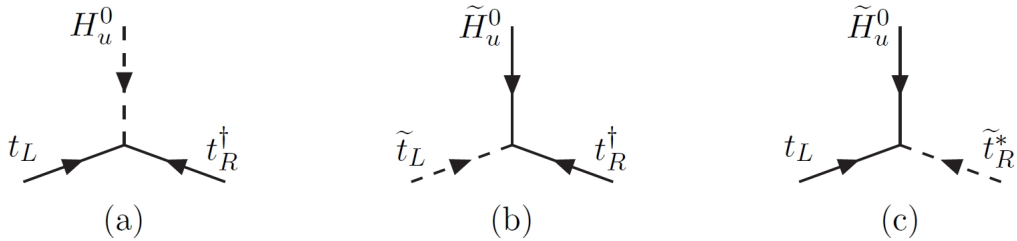


Figure 2.3.: The Yukawa coupling between Higgs boson and top quark (a), Higgsino ans stops (b),(c) [6].

2.3.3. *R*-parity

The superpotential written in 2.53 does not include terms which explicitly violate lepton or baryon numbers. However these terms exist and are invariant and renormalisable. They are

$$W_{\Delta L=1} = \frac{1}{2} \lambda^{ijk} L_i L_j \bar{e}_k + \lambda'^{ijk} L_i Q_j \bar{d}_k + \mu'^i L_i H_u \quad (2.54)$$

$$W_{\Delta B=1} = \frac{1}{2} \lambda'^{ijk} \bar{u}_i \bar{d}_j \bar{d}_k \quad (2.55)$$

If baryon and lepton numbers were violated simultaneously, protons would decay in very short time, for instance following the process $p \rightarrow e^+ \pi^0$. However, the proton lifetime

is observed to be greater than $10^{33} - 10^{34}$ years. In order to solve this problem, an additional discrete symmetry, called *R*-parity, is introduced and the corresponding quantum number is asked to be conserved.

$$R = (-1)^{3(B-L)+2\sigma} \quad (2.56)$$

where B is the baryonic number, $B = 1/3$ for quarks and squarks, $B = 0$ otherwise; L is the leptonic number, $L = 1$ for leptons and sleptons, $L = 0$ otherwise; σ is the spin. With this definition, $R = 1$ for all particles of the Standard Model, $R = -1$ for all superparticles. The conservation of *R*-parity forbids the baryon and lepton numbers to be violated simultaneously. In the case where the baryon or lepton numbers are separately violated, *R*-parity is still conserved.

The conservation of *R*-parity leads to two important phenomenological consequences:

- The lightest supersymmetric particle (LSP) must be stable. This leads to a very significant hypothesis in cosmology. In the high temperature of the early Universe when the SUSY was not broken, an enormous amount of such superparticle would have been produced. Since it can not decay, it must still exist in our Universe today. And if it is electrically neutral and interacts weakly with ordinary matter, it can be a candidate for the non-baryonic dark matter.
- The superparticles can be produced in pair in the collisions of SM particles. That means we may catch the superparticles in our detectors if the collision energy is large enough to produce them.

2.3.4. Soft SUSY breaking in MSSM

We now use equation 2.44 to write down the Lagrangian of soft SUSY breaking in MSSM.

$$\begin{aligned} \mathcal{L}_{\text{soft}}^{\text{MSSM}} = & -\frac{1}{2}(M_3 \tilde{g} \tilde{g} + M_2 \tilde{W} \tilde{W} + M_1 \tilde{B} \tilde{B} + \text{h.c.}) \\ & -\tilde{Q}^\dagger \mathbf{m}_Q^2 \tilde{Q} - \tilde{\bar{u}} \mathbf{m}_{\bar{u}}^2 \tilde{\bar{u}}^\dagger - \tilde{\bar{d}} \mathbf{m}_{\bar{d}}^2 \tilde{\bar{d}}^\dagger \\ & -\tilde{L}^\dagger \mathbf{m}_L^2 \tilde{L} - \tilde{\bar{e}} \mathbf{m}_{\bar{e}}^2 \tilde{\bar{e}}^\dagger \\ & -m_{H_u}^2 H_u^* H_u - m_{H_d}^2 H_d^* H_d - (b H_u H_d + \text{h.c.}) \\ & -(\tilde{\bar{u}} \mathbf{a}_{\bar{u}} \tilde{Q} H_u - \tilde{\bar{d}} \mathbf{a}_{\bar{d}} \tilde{Q} H_d - \tilde{\bar{e}} \mathbf{a}_{\bar{e}} \tilde{L} H_d + \text{h.c.}) \end{aligned} \quad (2.57)$$

The first line of equation 2.57 expresses the gaugino (gluino, wino and bino) mass term (the gauge indices are suppressed).

The second and third lines are the squark and slepton squared-mass terms respectively, where the \mathbf{m}_Q^2 , $\mathbf{m}_{\bar{u}}^2$, $\mathbf{m}_{\bar{d}}^2$, \mathbf{m}_L^2 and $\mathbf{m}_{\bar{e}}^2$ are 3×3 matrices, the family indices are also suppressed (see Table 2.1).

The fourth line is the Higgs mass terms, where b is the squared-mass term of the type b^{ij} and $m_{H_u}^2, m_{H_d}^2$ are the squared-mass term of the type $(m^2)_j^i$ in the equation of soft supersymmetry breaking 2.44.

The last line is the triple scalar coupling terms, where $\mathbf{a_u}, \mathbf{a_d}, \mathbf{a_e}$ are complex 3×3 matrices and are of the type of a^{ijk} as in equation 2.44.

All the terms in 2.57 clearly break SUSY. We expect that all these parameters are of the order of m_{soft} and in the range of [100,1000] GeV.

2.3.5. The mass spectrum of the MSSM

- **The Higgs sector**

In MSSM, two Higgs doublets are needed, (H_u^+, H_u^0) and (H_d^0, H_d^-) , while there is one Higgs in the Standard Model. The Higgs scalar potential in MSSM is

$$\begin{aligned} V_{\text{Higgs}} = & (|\mu|^2 + m_{H_u}^2)(|H_u^0|^2 + |H_u^+|^2) + (|\mu|^2 + m_{H_d}^2)(|H_d^0|^2 + |H_d^-|^2) \\ & + [b(H_u^+ H_d^- - H_u^0 H_d^0) + \text{h.c.}] \\ & + \frac{1}{8}(g^2 + g'^2)(|H_u^0|^2 + |H_u^+|^2 - |H_d^0|^2 + |H_d^-|^2)^2 \\ & + \frac{1}{2}g^2|H_u^+ H_d^{0*} + H_u^0 H_d^{-*}|^2 \end{aligned} \quad (2.58)$$

The minimum of this potential is required to break electroweak down to electromagnetic symmetry. This results in $H_u^+ = H_d^- = 0$ at the minimum of the potential. The potential is now restricted to the neutral sector.

$$\begin{aligned} V_{\text{Higgs}} = & (|\mu|^2 + m_{H_u}^2)|H_u^0|^2 + (|\mu|^2 + m_{H_d}^2)|H_d^0|^2 - bH_u^0 H_d^0 + \text{h.c.} \\ & + \frac{1}{8}(g^2 + g'^2)(|H_u^0|^2 - |H_d^0|^2)^2 \end{aligned} \quad (2.59)$$

The parameter b can be taken to be real and positive. For the electroweak symmetry breaking, it is necessary that H_u^0 and H_d^0 get non-zero VEVs. This leads to two conditions:

$$2b < 2|\mu|^2 + m_{H_u}^2 + m_{H_d}^2 \quad (2.60)$$

$$b^2 > (|\mu|^2 + m_{H_u}^2)(|\mu|^2 + m_{H_d}^2) \quad (2.61)$$

Now we require the non-zero VEVs of H_u^0 and H_d^0 to be compatible with the electroweak symmetry breaking with:

$$v_u = \langle H_u^0 \rangle, \quad v_d = \langle H_d^0 \rangle \quad (2.62)$$

and one must have a connection with the phenomenology of electroweak symmetry breaking via:

$$v_u^2 + v_d^2 = 2m_Z^2/(g^2 + g'^2) \approx (174\text{GeV})^2 \quad (2.63)$$

The ratio of the two VEVs is written as

$$\tan\beta \equiv v_u/v_d \quad (2.64)$$

Using the conditions at the minimum of the potential $\partial V/\partial H_u^0 = \partial V/\partial H_d^0 = 0$ and relations 2.63, 2.64, we obtain:

$$\sin 2\beta = \frac{2b}{m_{H_u}^2 + m_{H_d}^2 + 2|\mu|^2} \quad (2.65)$$

$$m_Z^2 = \frac{|m_{H_d}^2 - m_{H_u}^2|}{\sqrt{1 - \sin^2(2\beta)}} - m_{H_u}^2 - m_{H_d}^2 - 2|\mu|^2 \quad (2.66)$$

In the minimal SM, there are four degrees of freedom (dof) for the Higgs doublet; after electroweak symmetry breaking, three of them are absorbed by W^\pm and Z^0 and the other one given to the neutral Higgs boson. In the MSSM, there are two Higgs doublets, which correspond to eight degrees of freedom. When electroweak symmetry is broken, these degrees of freedom become:

- The three degrees of freedom corresponding to the Goldstone bosons go to the longitudinal mode of the massive vector bosons W^\pm and Z^0 .
- Two dof go to two CP even neutral scalars h^0 and H^0 .
- One dof goes to one CP odd neutral scalar A^0 .
- Two dof go to two charged scalars H^+ and H^- .

The Higgs masses are then after some algebra:

$$m_{A^0}^2 = \frac{2b}{\sin 2\beta} \quad (2.67)$$

$$m_{H^\pm}^2 = m_{A^0}^2 + m_W^2 \quad (2.68)$$

$$m_{h^0, H^0}^2 = \frac{1}{2}(m_{A^0}^2 + m_Z^2) \mp \sqrt{(m_{A^0}^2 - m_Z^2)^2 + 4m_Z^2 m_{A^0}^2 \sin^2(2\beta)} \quad (2.69)$$

• Neutralinos and charginos

After electroweak symmetry breaking, the higgsinos and electroweak gauginos mix together to form new mass eigenstates. As the superpartners of the neutral Higgs and

gauge bosons are not mass eigenstate, we write down their mass Lagrangian.

$$\mathcal{L} = -\frac{1}{2} \psi_0^T M_n \psi_0 \quad (2.70)$$

where $\psi_0 = (\tilde{B}, \tilde{W}^0, \tilde{H}_d^0, \tilde{H}_u^0)$ and

$$M_n = \begin{pmatrix} M_1 & 0 & -m_Z \cos \beta \sin \theta_W & m_Z \sin \beta \sin \theta_W \\ 0 & M_2 & m_Z \cos \beta \cos \theta_W & -m_Z \sin \beta \cos \theta_W \\ -m_Z \cos \beta \sin \theta_W & m_Z \cos \beta \cos \theta_W & 0 & -\mu \\ m_Z \sin \beta \sin \theta_W & -m_Z \sin \beta \cos \theta_W & -\mu & 0 \end{pmatrix} \quad (2.71)$$

Here M_1 and M_2 are the bino and wino mass parameters that come from equation 2.57. In equation 2.57, they can be complex, but in this equations they are taken to be real and positive by redefining their phases. The higgsino mass parameter μ is real with sign $I = \pm 1$.

Diagonalizing the above mass matrix gives the masses of the particles:

$$m_{\tilde{N}_1} = M_1 - \frac{m_Z^2 s_W^2 (M_1 + \mu \sin 2\beta)}{\mu^2 - M_1^2} \quad (2.72)$$

$$m_{\tilde{N}_2} = M_2 - \frac{m_W^2 (M_2 + \mu \sin 2\beta)}{\mu^2 - M_2^2} \quad (2.73)$$

$$m_{\tilde{N}_3} = |\mu| + \frac{m_Z^2 (I - \sin 2\beta) (\mu + M_1 c_W^2 + M_2 s_W^2)}{2(\mu + M_1)(\mu + M_2)} + \dots \quad (2.74)$$

$$m_{\tilde{N}_4} = |\mu| + \frac{m_Z^2 (I + \sin 2\beta) (\mu - M_1 c_W^2 - M_2 s_W^2)}{2(\mu - M_1)(\mu - M_2)} + \dots \quad (2.75)$$

where $s_W = \sin \theta_W$, $c_W = \cos \theta_W$. These masses eigenstates are called *neutralinos*. The lightest neutralino, \tilde{N}_1 , is usually the LSP.

In a similar way, one can get the spectrum of *charginos*:

$$m_{\tilde{C}_1}^2, m_{\tilde{C}_2}^2 = \frac{1}{2} (\xi \mp \sqrt{\xi^2 - 4|\mu M_2 - m_W^2 \sin 2\beta|^2}) \quad (2.76)$$

where $\xi = |M_2|^2 + |\mu|^2 + 2m_W^2$.

• Squarks and sleptons

In general, squarks and sleptons of the same charge get mixed. But one can show that if universality is valid, the mixing is only large for the third family. The first and second families of squarks and sleptons have negligible Yukawa couplings, so they end up in 7 very nearly degenerate, unmixed pairs $(\tilde{e}_R, \tilde{\mu}_R)$, $(\tilde{\nu}_e, \tilde{\nu}_\mu)$, $(\tilde{e}_L, \tilde{\mu}_L)$, $(\tilde{u}_R, \tilde{c}_R)$, $(\tilde{d}_R, \tilde{s}_R)$,

$(\tilde{u}_L, \tilde{c}_L)$, $(\tilde{d}_L, \tilde{s}_L)$. For the third family, due to the large Yukawa couplings (y_t, y_b, y_τ) and soft couplings (a_t, a_b, a_τ) , they have significant mixing.

The mass term of the top squarks in the Lagrangian is:

$$\mathcal{L}_{\text{stop masses}} = - \begin{pmatrix} \tilde{t}^*_L & \tilde{t}^*_R \end{pmatrix} \mathbf{M}_t^2 \begin{pmatrix} \tilde{t}_L \\ \tilde{t}_R \end{pmatrix} \quad (2.77)$$

where \mathbf{M}_t^2 is the mass matrix for the top squark:

$$\mathbf{M}_t^2 = \begin{pmatrix} m_{Q_3}^2 + m_t^2 + \Delta_{\tilde{u}_L} & v(a_t^3 \sin \beta - \mu y_t \cos \beta) \\ v(a_t \sin \beta - \mu^* y_t \cos \beta) & m_{\tilde{t}_R}^2 + m_t^2 + \Delta_{\tilde{u}_R} \end{pmatrix} \quad (2.78)$$

with

$$\Delta = (T_3 - Q \sin^2 \theta_W) m_Z^2 \cos 2\beta \quad (2.79)$$

This matrix is hermitian and can be diagonalised using a unitary matrix. We have then the mixing:

$$\begin{pmatrix} \tilde{t}_1 \\ \tilde{t}_2 \end{pmatrix} = \begin{pmatrix} c_{\tilde{t}} & -s_{\tilde{t}} \\ s_{\tilde{t}} & c_{\tilde{t}} \end{pmatrix} \begin{pmatrix} \tilde{t}_L \\ \tilde{t}_R \end{pmatrix} \quad (2.80)$$

where $|c_{\tilde{t}}|^2 + |s_{\tilde{t}}|^2 = 1$, $c_{\tilde{t}}$ and $s_{\tilde{t}}$ are cosin and sine of the mixing angle $\theta_{\tilde{t}}$ if the all diagonal elements of the mass matrix are real. We have here $m_{\tilde{t}_1}^2 < m_{\tilde{t}_2}^2$. A similar analysis for the sbottom and stau can be performed. Their mass matrices are:

$$\mathbf{M}_b^2 = \begin{pmatrix} m_{Q_3}^2 + \Delta_{\tilde{d}_L} & v(a_b^* \cos \beta - \mu y_b \sin \beta) \\ v(a_b \cos \beta - \mu^* y_b \sin \beta) & m_{\tilde{d}_3}^2 + \Delta_{\tilde{d}_R} \end{pmatrix} \quad (2.81)$$

$$\mathbf{M}_\tau^2 = \begin{pmatrix} m_{L_3}^2 + \Delta_{\tilde{e}_L} & v(a_\tau^* \cos \beta - \mu y_\tau \sin \beta) \\ v(a_\tau \cos \beta - \mu^* y_\tau \sin \beta) & m_{\tilde{e}_3}^2 + \Delta_{\tilde{e}_R} \end{pmatrix} \quad (2.82)$$

• Gluino

The gluino \tilde{g} is a colour octet fermion, therefore it cannot mix with any other MSSM particle. The gluino mass parameter M_3 is related to the bino and wino mass parameters M_1 and M_2 by $M_3 : M_2 : M_1 \approx 6 : 2 : 1$. This relation shows that the gluino should be heavier than the lighter neutralino and chargino.

Finally, we obtain the particle spectrum in MSSM given in table 2.3

Name	Spin	P_R	Gauge Eigenstates	Mass Eigenstates
Higgs bosons	0	+1	$H_u^0 \ H_d^0 \ H_u^+ \ H_d^-$	$h^0 \ H^0 \ A^0 \ H^\pm$
squarks	0	-1	$\tilde{u}_L \ \tilde{u}_R \ \tilde{d}_L \ \tilde{d}_R$ $\tilde{s}_L \ \tilde{s}_R \ \tilde{c}_L \ \tilde{c}_R$ $\tilde{t}_L \ \tilde{t}_R \ \tilde{b}_L \ \tilde{b}_R$	same same $\tilde{t}_1 \ \tilde{t}_2 \ \tilde{b}_1 \ \tilde{b}_2$
sleptons	0	-1	$\tilde{e}_L \ \tilde{e}_R \ \tilde{\nu}_e$ $\tilde{\mu}_L \ \tilde{\mu}_R \ \tilde{\nu}_\mu$ $\tilde{\tau}_L \ \tilde{\tau}_R \ \tilde{\nu}_\tau$	same same $\tilde{\tau}_1 \ \tilde{\tau}_2 \ \tilde{\nu}_\tau$
neutralinos	1/2	-1	$\tilde{B}^0 \ \tilde{W}^0 \ \tilde{H}_u^0 \ \tilde{H}_d^0$	$\tilde{N}_1 \ \tilde{N}_2 \ \tilde{N}_3 \ \tilde{N}_4$
charginos	1/2	-1	$\tilde{W}^\pm \ \tilde{H}_u^\pm \ \tilde{H}_d^-$	$\tilde{C}_1^\pm \ \tilde{C}_2^\pm$
gluino	1/2	-1	\tilde{g}	same
goldstino	1/2	-1	\tilde{G}	same
gravitino	3/2	-1	\tilde{G}	same

Table 2.3.: The particles in the MSSM.

2.3.6. Origins of supersymmetry breaking in MSSM

We are interested mostly in the way supersymmetry got broken. We know a mechanism by which a symmetry can be broken, that is the spontaneous symmetry breaking. However, it can be shown that original spontaneous symmetry breaking cannot occur in MSSM. The prevailing idea is that spontaneous symmetry breaking occurs in some hidden sector via some non renormalisable interactions and is communicated to the visible sector by some interactions.

There have been two main hypotheses for mediating these interactions:

- **Gravity mediation:** Gravity is clearly a plausible candidate for the hidden sector as quantum gravity is certainly outside the domain of present normalisable field theories. The SUSY breaking source is transmitted from the hidden sector to the MSSM by the new interactions including gravity that enter near the Planck mass scale M_P . If SUSY is broken in the hidden sector by some vacuum expectation values ($\langle F \rangle$) of the auxiliary field F , the soft SUSY terms should be of the order:

$$m_{\text{soft}} \sim \frac{\langle F \rangle}{M_P} \quad (2.83)$$

If we demand that m_{soft} is around 1 TeV, then $\sqrt{\langle F \rangle} \sim 10^{11}$ or 10^{12} GeV.

- **Gauge mediation:** Here, the mediating interactions are the ordinary electroweak and strong gauge interactions. More precisely, there exist some *messengers* that can

couple directly to a SUSY breaking source in the *secluded sector* and also couple to the MSSM visible particles via the $SU(3)_C \times SU(2)_L \times U(1)_Y$ interactions. (From now on, we will use the terminology "secluded sector" for GMSB models to distinguish them from the hidden sector in the theories where SUSY breaking is mediated by gravity.) This scenario is called *gauge mediated supersymmetry breaking* (GMSB). The soft SUSY breaking terms come from loop diagrams containing these messengers. We can estimate the m_{soft} .

$$m_{\text{soft}} \sim \frac{\alpha_a}{4\pi} \frac{\langle F \rangle}{M_{\text{mess}}} \quad (2.84)$$

where the $\alpha_a/4\pi$ is a loop factor for Feynman diagrams involving gauge interactions, M_{mess} is the messenger mass. If m_{soft} ranges from few hundreds GeV to 1 TeV and M_{mess} and $\sqrt{\langle F \rangle}$ are of the same order, we estimate $\sqrt{\langle F \rangle} \sim 10^4 \div 10^5$ GeV, which is much lower than the value we got in the case of gravity mediated symmetry breaking. In this thesis, we concentrate on the minimal model of GMSB.

2.4. The minimal GMSB models

2.4.1. Structure of mGMSB

In the previous section, we have already given a short introduction on the GMSB. The SUSY breaking is based on the F -term occurring for single chiral supermultiplet as F acquires a non-zero VEV. So, the idea of GMSB is that there are some messengers which couple directly to the single chiral supermultiplet in the secluded sector and also couple to the MSSM particles via gauge interactions. The mechanism of the GMSB models is presented in figure 2.4.

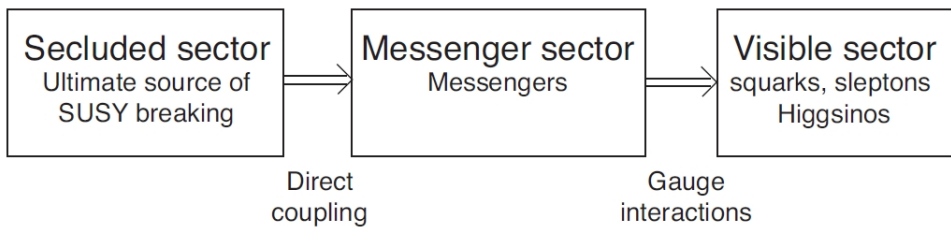


Figure 2.4.: The mechanism for mediating the SUSY breaking source from the secluded sector to the visible sector in the GMSB models.

We first introduce the gauge single chiral supermultiplet S in the secluded sector. And the messenger sector is described by N_f flavours of the new chiral supermultiplets (messengers) Φ_i and $\bar{\Phi}_i$ with $i = 1, \dots, N_f$, the bar denotes that Φ_i and $\bar{\Phi}_i$ transform under conjugate representations of the Standard Model gauge group, so their quantum

numbers are exactly opposite. We denote the scalar, fermionic and auxiliary components of Φ_i by ϕ_i, ψ_i and F_i , those of $\bar{\Phi}_i$ by $\bar{\phi}_i, \bar{\psi}_i$ and \bar{F}_i ; and those of S by ϕ_S, ψ_S and F_S .

The components ϕ_S and F_S acquire the non-zero VEVs, denoted by $\langle \phi_S \rangle$ and $\langle F_S \rangle$. The Φ_i are a set of left handed chiral supermultiplets q, \bar{q}, l, \bar{l} . They contain messenger quarks ($\psi_q, \psi_{\bar{q}}$) and scalar (q, \bar{q}) and corresponding messenger leptons and scalar leptons. These particles must get very high masses in order not to be detected yet by experiments.

The messengers interact with the single supermultiplet in the secluded sector via the superpotential:

$$W_{\text{mess}} = \sum y_i S \Phi_i \bar{\Phi}_i \quad (2.85)$$

The Lagrangian of fermionic messenger fields is

$$\mathcal{L} = -y_i \langle \phi_S \rangle \psi_i \bar{\psi}_i + \text{c.c.} \quad (2.86)$$

The fermion masses are given:

$$m_{\text{fermion}}^2 = |y_i \langle \phi_S \rangle|^2 \quad (2.87)$$

The scalar superpotential containing the mass terms of scalar messenger fields is then:

$$V = |y_i \langle \phi_S \rangle|^2 (\phi_i \phi_i^* + \bar{\phi}_i \bar{\phi}_i^*) - (y_i \langle F_S \rangle \phi_i \bar{\phi}_i + y_i^* \langle F_S^* \rangle \phi_i^* \bar{\phi}_i^*) + \text{quartic} \quad (2.88)$$

The first term presents the mass terms, while the second term consists of soft supersymmetry breaking masses. The Lagrangian containing this potential can be written as

$$\mathcal{L} = \begin{pmatrix} \phi_i^* \\ \bar{\phi}_i \end{pmatrix} \begin{pmatrix} |y_i \langle \phi_S \rangle|^2 & -y_i^* \langle F_S^* \rangle \\ -y_i \langle F_S \rangle & |y_i \langle \phi_S \rangle|^2 \end{pmatrix} \begin{pmatrix} \phi_i \\ \bar{\phi}_i^* \end{pmatrix} \quad (2.89)$$

The matrix is the squared mass matrix. The scalar messenger masses are the eigenvalues of this matrix.

$$m_i^2 = |y_i \langle \phi_S \rangle|^2 \pm |y_i \langle F_S \rangle| \quad (2.90)$$

Comparing equations 2.87 and 2.90, we note that the supersymmetry is broken if $\langle F_S \rangle \neq 0$; and each messenger supermultiplet pair (Φ and $\bar{\Phi}$) is split in mass by the effect of SUSY breaking.

The gauginos of MSSM obtain masses from the loop in figure 2.5 and the computed masses are

$$M_a = \frac{\alpha_a}{4\pi} \Lambda N_5 \quad (2.91)$$

where Λ is the scale at which the SUSY breaking happens and is defined as:

$$\Lambda = \langle F_S \rangle / \langle \phi_S \rangle \quad (2.92)$$

and N_5 is the number of messenger supermultiplets. Because the messenger masses far below the GUT scale can ruin the grand unification, the number of messenger supermultiplets are required to be equal to the number of multiplets of $SU(5)$ group.

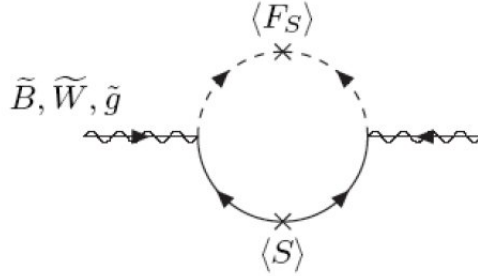


Figure 2.5.: The loop gives masses to the gauginos [6].

For the MSSM scalars, the masses come from the two-loop order.

$$m_\phi^2 = 2\Lambda^2 N_5 \sum_{a=1}^3 C_a(i) \left(\frac{\alpha_a}{4\pi} \right)^2 \quad (2.93)$$

where $C_a(i)$ is the quadratic Casimir group theory invariants for the superfields. For the MSSM supermultiplets, we have:

$$\begin{aligned} C_3(i) &= \begin{cases} 4/3 & \text{for } Q, \bar{u}, \bar{d} \\ 0 & \text{for } L, \bar{e}, H_u, H_d \end{cases} \\ C_2(i) &= \begin{cases} 3/4 & \text{for } Q, L, H_u, H_d \\ 0 & \text{for } \bar{u}, \bar{d}, \bar{e} \end{cases} \\ C_1(i) &= 3Y_i^2/5 \text{ for each field with weak hypercharge } Y_i \end{aligned} \quad (2.94)$$

Equations 2.91 and 2.93 are equivalent to the estimation in equation 2.84 if the messenger masses are in order of $M_{\text{mess}} \approx y_I \langle \phi_S \rangle$.

2.4.2. The Lightest Supersymmetric Particle

In the Introduction, we mentioned the spin-2 graviton and its superpartner, the spin-3/2 gravitino. They should be included in the complete SUSY models of Nature. And if the SUSY were unbroken, they are both massless. In the SUSY models, when SUSY is spontaneously broken, the gravitino acquires mass by absorbing the goldstino. This is called the *super-Higgs* mechanism, similar to the ordinary Higgs mechanism of the SM. The mass of gravitino is calculated as:

$$m_{3/2} \sim \langle F \rangle / M_P \quad (2.95)$$

Equation 2.95 shows that if SUSY is unbroken, i.e. $\langle F \rangle \rightarrow 0$, the gravitino will be massless. Using predictions for $\langle F \rangle$ in gauge-mediated and gravity-mediated models, equation 2.95 gives the mass of gravitino in gauge-mediated that is much lower than in gravity-mediated models. The GMSB models also predict $M_{\text{mess}} \ll M_P$, i.e. that the gravitino's mass is much lower than the masses of the MSSM particles. It is clear that the gravitino is the Lightest Supersymmetric Particle in the GMSB models. If R -parity is conserved, all MSSM sparticles will follow decay chains leading to the gravitino.

2.4.3. The Next-to-Lightest Supersymmetric Particle

From equation 2.91 and 2.93, we see that since $\alpha_1 < \alpha_2, \alpha_3$ (for example, at the electroweak scale, $Q_0 = m_Z$: $\alpha_3^{-1}(m_Z) = 8.5$, $\alpha_2^{-1}(m_Z) = 29.57$, $\alpha_1^{-1}(m_Z) = 59.00$), the superparticles with only $U(1)_Y$ interactions will be the lightest among gauginos and sfermions. These superparticles are the bino and the right-handed sleptons $\tilde{e}_R, \tilde{\mu}_R, \tilde{\tau}_R$. So the corresponding mass eigenstates (neutralino, or sneutrino, or sleptons) will be the plausible candidates for the Next-to-Lightest Supersymmetric Particle. Depending on the parameter choice, the NLSP are either the neutralino, or sneutrino, or slepton. We will only discuss the case of slepton.

Finally, for GMSB, one arrive at the spectrum which depends on the six parameters:

$$\Lambda, M_{\text{mess}}, \sqrt{\langle F \rangle / k}, N_5, \tan\beta, \text{sgn}\mu \quad (2.96)$$

Equation 2.82 shows that the mixing grows with $\tan\beta$. If $\tan\beta$ is not very large, i.e. the mixing is small, the masses of $\tilde{e}_R, \tilde{\mu}_R$ are close to the mass of $\tilde{\tau}_1$, the three-body slepton decays, like $\tilde{e}_R \rightarrow e\tau^\pm \tilde{\tau}_1^\mp, \tilde{\mu}_R \rightarrow \mu\tau^\pm \tilde{\tau}_1^\mp$ are suppressed by kinetic condition. Two-body decays are allowed: $\tilde{e}_R \rightarrow e\tilde{G}, \tilde{\mu}_R \rightarrow \mu\tilde{G}$ and $\tilde{\tau}_1 \rightarrow \tau\tilde{G}$. This picture is called the "slepton co-NLSP" scenario. If $\tan\beta$ is large enough, the three-body slepton decays are allowed, and $\tilde{\tau}_1$ is the only NLSP and is dominated by the right-handed component $\tilde{\tau}_R$. This picture is called the stau "NLSP" scenario. In any case, the $\tilde{\tau}_1$ decays into τ

and \tilde{G} with a width:

$$\Gamma(\tilde{\tau}_1 \rightarrow \tau \tilde{G}) = 2 \times 10^{-3} k^2 \left(\frac{m_{\tilde{\tau}_1}}{100 \text{ GeV}} \right)^5 \left(\frac{\sqrt{\langle F \rangle}}{100 \text{ TeV}} \right)^{-4} \text{ eV} \quad (2.97)$$

where k is a coefficient less than 1 and depends on how supersymmetry breaking is communicated to the messengers.

The equation above shows that the lifetime of $\tilde{\tau}_1$ depends on $\sqrt{\langle F \rangle/k}$. If $\sqrt{\langle F \rangle/k}$ is larger than about 10^3 TeV, then the $\tilde{\tau}_1$ is long-lived, that means it can travel through the detector before its decay. Figure 2.6 displays a spectrum of mass and lifetime of the particles in the mGMSB. In this spectrum, the stau is the NLSP with a mass of 124 GeV/c² and a lifetime of 184 ns and marked by the blue star.

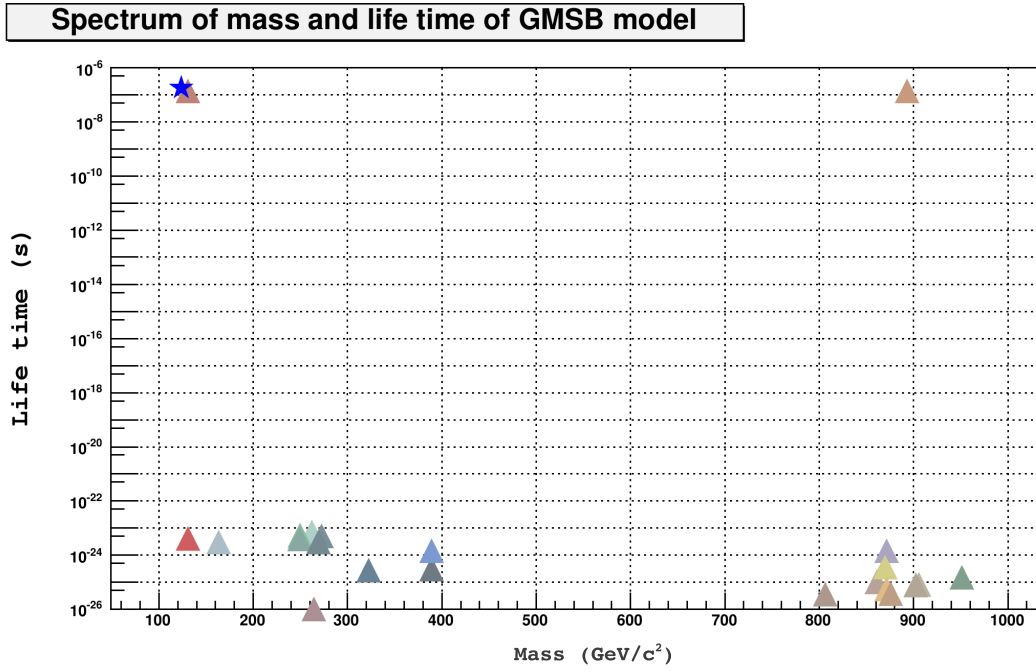


Figure 2.6.: A mass spectrum and life time of the particles in the mGMSB, where the stau is the NLSP marked by the blue star. The stau has a mass of 124 GeV/c² and a lifetime of 184 ns.

Now, back to equations 2.93 and 2.94, we see that the $\tilde{\tau}_R$ get mass only from the interaction of $U(1)_Y$ group, i.e. it has only $U(1)$ quantum numbers; in other words, $\tilde{\tau}_1$ has only electromagnetic interactions with medium atoms. Hence, the staus ($\tilde{\tau}_1$) will deposit little energy in the hadron calorimeter, but leave signals in the tracking and muon

systems. If they have high speed, they will penetrate through the entire spectrometer and are misidentified as muons.

As presented in section 2.3.3, the conservation of R -parity in the SUSY models allows the staus to be produced in pair in the pp collisions. Figures 2.7 presents the Feynman diagram for stau pair production via a Drell-Yan like processes at leading order (LO) in perturbative QCD [12] (figure (a)) and one of the Feynman diagrams at next-to-leading order (NLO) (figure (b)).

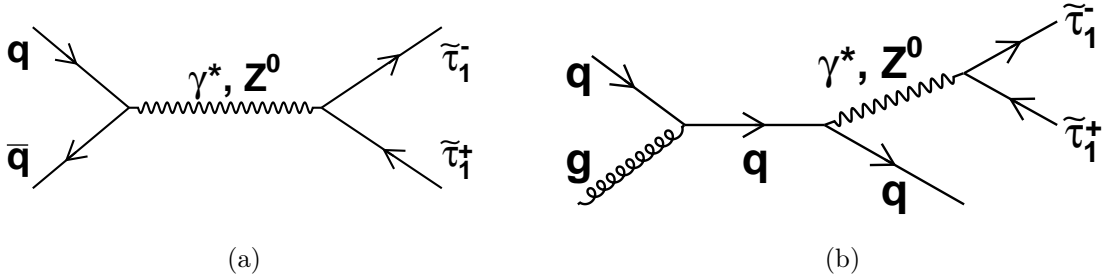


Figure 2.7.: Feynman diagrams for stau pair production at leading order in perturbative QCD (a) and at next-to-leading order (NLO) (b) [12].

For the search of staus, physicists exploit mainly two features:

- Staus are slower than muons, therefore their time of flight is longer.
- Staus are very massive, so they would have anomalously high ionizing tracks.

These above points show that we have the ability to produce and detect staus at LHC. As was mentioned in the Introduction, this thesis is dedicated to the search of stau in LHCb detector by combining the signals from the different sub-detectors.

Part II.

The LHCb experiment

Chapter 3.

Large Hadron Collider

The Large Hadron Collider (LHC) ([13], [14]) is the largest collider in the world in 2013, both because of its size and the energy of the accelerated particles. It was constructed by the European Organization for Nuclear Research (CERN) from 1998 to 2008, with the aim of testing the Standard Model and physics beyond it. The main subjects studied on this machine are to search for the existence of the hypothesized Higgs boson, to provide precise measurements of CP violation, to study the state of matter called quark-gluon plasma, to search for monopoles, etc. In addition, with the pp collisions whose centre-of-mass energy can go up to 14 TeV, one has the opportunity to look for new physics, like Supersymmetry, dark matter and dark energy.

The LHC is built on the French and Swiss border, in a circular tunnel of 27 km in circumference and around 50 m to 175 m underground to avoid a high flux of cosmic rays and radiation hazard. It is designed to collide two counter-rotating beams of protons or heavy ions; each beam can attain 7 TeV. Each beam consists of 2808 bunches (n_b), and each bunch has 10^{11} protons (N_b). The time between two consecutive beam crossing is 25 ns. The luminosity of LHC is given by

$$L = \frac{N_b^2 n_b \nu}{F} \quad (3.1)$$

where ν is the frequency of revolution and F is a factor that groups the terms describing the beam geometry. The maximum luminosity of the LHC is $10^{34} \text{cm}^{-2}\text{s}^{-1}$.

Figure 3.1(a) shows the scheme of the LHC with its experiments and figure 3.1(b) presents the tunnel of LHC. Seven experiments constructed on LHC are:

- **ALICE** (A Large Ion Collider Experiment) [15] focuses on studying the state of matter known as quark-gluon plasma, which is believed to have existed soon after the Big Bang. Alice uses the lead ion collisions.

- **ATLAS** (A Toroidal LHC ApparatuS) [16] and **CMS** (Compact Muon Solenoid) [17] are designed for the main aim of discovering the Higgs bosons. The two experiments are required to cross-check their results. However, many other subjects are being exploited with these detectors.

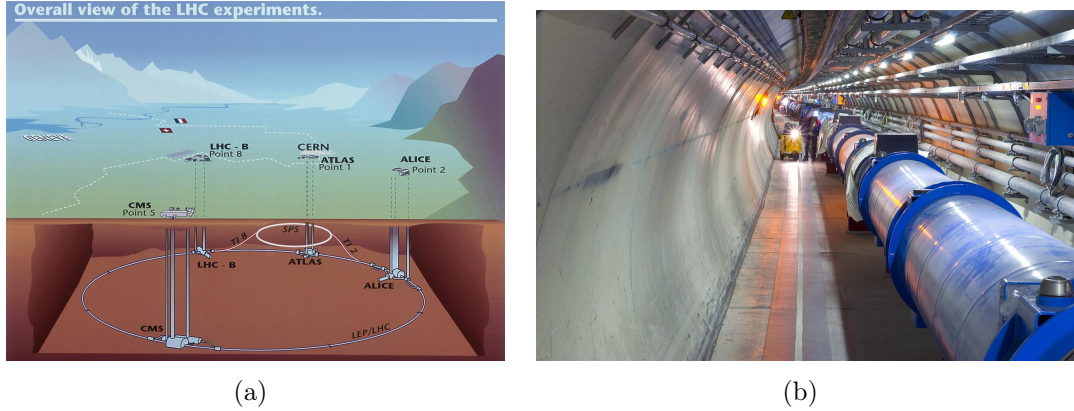


Figure 3.1.: The LHC scheme (a) and the LHC tunnel (b).

- **LHCb** (Large Hadron Collider beauty) [18] measures the B decays to study CP violation, a high vertex resolution is therefore required. Hence, the luminosity at LHCb is reduced to an optimal luminosity of $2 \times 10^{32} \text{cm}^{-2}\text{s}^{-1}$, which is much lower than the designed LHC luminosity.
- **TOTEM** (TOTal Elastic and diffractive cross section Measurement) [19] is dedicated to measure the total pp cross section and to study elastic and diffractive scattering at the LHC. The TOTEM detector is located within the CMS detector.
- **LHCf** (Large Hadron Collider forward) [20] consists of two small detectors installed on sides of the ATLAS detector, about 450 feet from the collision point. LHCf study the production of neutral particles (π^0, γ) at very forward angles in pp and nucleus-nucleus collisions. This study will give important clues for the understanding of the development of the atmospheric showers initiated by very high energy cosmic rays.

- **MoEDAL** (Monopole and Exotics Detector At the LHC) [21] shares the cavern with the LHCb detector, and it is installed close to the VELO sub-detector of LHCb. The goal of MoEDAL is to search for the direct production of magnetic monopoles at the LHC and highly ionizing, stable (or quasi-stable) massive particles.

The first collisions of the LHC took place on 30th March 2010. The pp collisions were produced at 7 TeV (i.e. 3.5 TeV per each beam) during 2011 and at 8 TeV during 2012. The LHC promises a new era of discoveries in High Energy Physics.

Chapter 4.

LHCb detector

The LHCb (Large Hadron Collider beauty) detector ([14] [22]) is designed to provide the precision measurements of CP violation and rare decays of B hadrons, i.e. the hadrons which contain the "beauty" quark (also called *bottom* quark and symbolized as b). Since the two B hadrons originating from a $b\bar{b}$ pair produced in the pp collisions at LHC fly in a same tight forward or backward cone, LHCb detector is designed as a single-arm forward spectrometer. The layout of the LHCb detector in the yz plane is shown in figure 4.1.

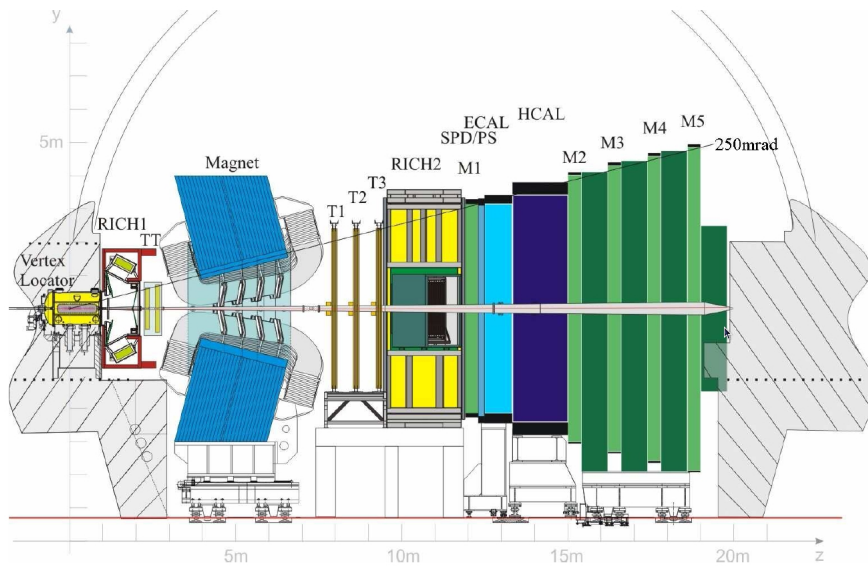


Figure 4.1.: The global LHCb detector

The LHCb detector stretches over 20 meters along the beam pipe and has a pseudo-rapidity acceptance $1.9 < \eta < 4.9$. It is composed of a magnet, a tracking system and a particle identification system. The tracking system includes the Vertex Locator, the Silicon trackers (TT and IT) and the outer trackers (OT). The particle identification system includes the RICHs, the calorimeters and the muon chambers.

4.1. Magnet

The LHCb warm dipole magnet is placed between the Tracker Turicensis (TT) and the three tracking stations (T1, T2, T3) in order to measure the momentum of charged particles with a precision of about 0.4% for momenta up to 200 GeV/c. It has an integrated field of 4 Tm and covers an acceptance of ± 250 mrad vertically and of ± 300 mrad horizontally. This magnet is composed of two saddle-shaped coils arranged inside an iron yoke of window-frame configuration. The total weights of the yoke and the two coils are 1500 and 54 tons, respectively. The magnet gap is wedge-shaped in both vertical and horizontal planes in order to fit to the detector acceptance. Figure 4.2(a) presents the LHCb magnet installed in the LHCb cavern. At a given z position from 3 m to 8 m, the magnetic field B is not totally uniform, it can vary $\pm 1\%$ in a plane xy of 1 m^2 . The main component, B_y , is shown in figure 4.2(b).

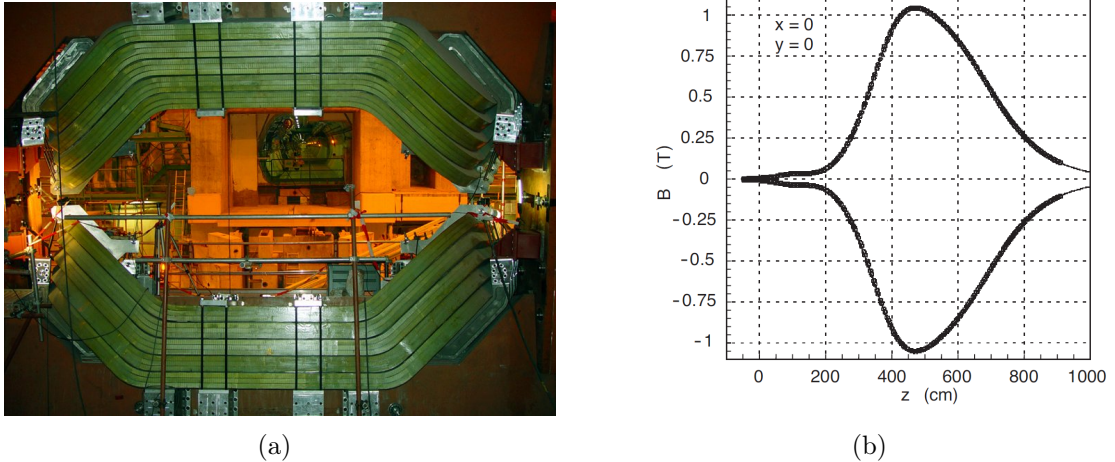


Figure 4.2.: LHCb magnet in xy plane in (a); the vertical magnetic field along the z -axis in (b).

The integrated field in the upstream TT region (0 - 2.5 m) is 0.1159 Tm and in the downstream TT region (2.5 - 7.95 m) is 3.614 Tm. However, the maximum field permitted at HPD's position of RICH1 is 20×10^{-4} T and of RICH2 is 9×10^{-4} T to ensure the operation of the HPDs. The measurement of the magnetic field attains a precision of about 4×10^{-4} . This satisfies the requirement about the resolution in momentum measurements of charged particles.

4.2. The tracking system

The task of the tracking system is to reconstruct the particle trajectory whose curvature allows to deduce the momentum and the sign of the curvature with respect to the

magnetic field direction gives the charge of particle. The LHCb tracking system consists of three sub-detectors: the Vertex Locator (VELO) covering the collision point, the Tracker Turicensis (TT) before the magnet and the three tracking stations T1-T3 behind the magnet. The VELO and TT are silicon pad and micro-strip detectors. In the T1-T3 stations, two different techniques are employed: silicon micro-strips for the region close to the beam pipe (Inner Tracker) and straw-tubes for the outer region of the stations (Outer Tracker) where the occupancy is less severe.

4.2.1. Vertex Locator

The VErtex LOcator (VELO) is placed close to the beam pipe (~ 8 mm) and surrounds the collision point. It provides a precise measurement of the track coordinates in the region close to the interaction point in order to form the primary and decay vertices. The resolution of the vertices depends on the number of tracks; for example, for a primary vertex of 25 tracks the resolutions are of 13, 12 and 69 μm in x , y , z dimensions respectively (this result is from 2011 data and for events that have only one reconstructed primary vertex). The VELO also allows to measure the deposited energies by the tracks in the silicon sensors that may be used to identify the particles.

The VELO is composed of 42 half-disc shaped modules that are spaced and perpendicular to the beam pipe over a length of ~ 1 m. Upstream of the VELO sensors, there are two pile-up veto stations. Each VELO module has two silicon sensors: one measures the radial distance r and another one measures the azimuthal angle ϕ in the cylindrical geometry. Each silicon sensor is 300 μm thick and has 2048 strips which are read out by 16 Beetle FE chip, providing analogue data. The modules are divided into two halves (21 modules for each half) that are retractable during the beam injection to avoid the very high radiation damage to the sensors and to increase the aperture around the beam as required by LHC machine. These two halves will be moved to the closed position during data taking with the stable beams. Figure 4.3 shows the arrangement of the silicon sensors in the xz plane, and the relative positions of the sensors when the VELO is fully closed or opened.

To enable the sensors to be close to the beams (~ 8 mm), the VELO vessel has to be integrated directly into the beam pipe. However, in order to prevent any accident from outgassing of the VELO modules which can jeopardize the LHC vacuum, the VELO vessel is maintained with a secondary vacuum which is separated from the machine vacuum by a thin wall of corrugated aluminium (RF foils). These RF foils form two boxes that enclose the VELO modules. The RF foils face to the beams are 0.3 mm thick, while the side walls of these boxes are 0.5 mm thick. A half of modules and a RF box are shown in figure 4.4(a). The two halves of detector can overlap each other when they are in the closed position, as in figure 4.4(b). These RF boxes are also intended to provide a shield against radio-frequency noises from the LHCb beams that affect to the VELO electronics.

The modules are put inside a vacuum vessel with a length of 1.4 m and a diameter of 1.1 m. The overview of the vessel is shown in figure 4.5.

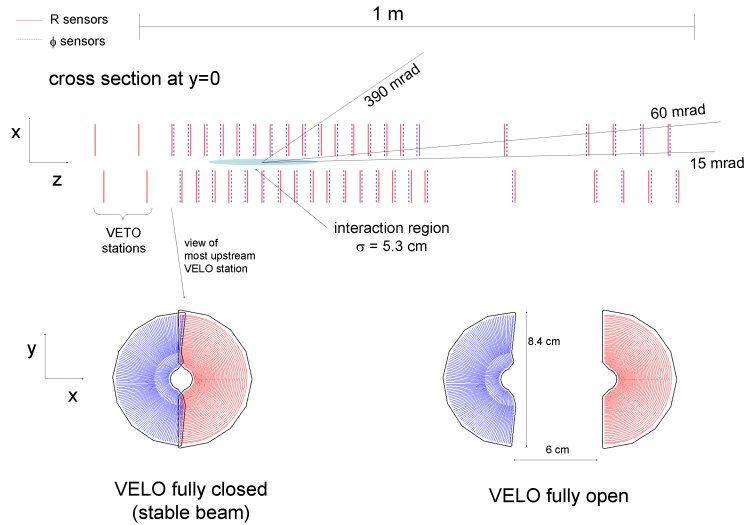


Figure 4.3.: The top figure shows the arrangement of the silicon sensors in the xz plane, at $y = 0$, when the VELO is fully closed. The bottom figures describe the relative positions of a right sensor and a left sensor when the VELO is fully closed or opened.

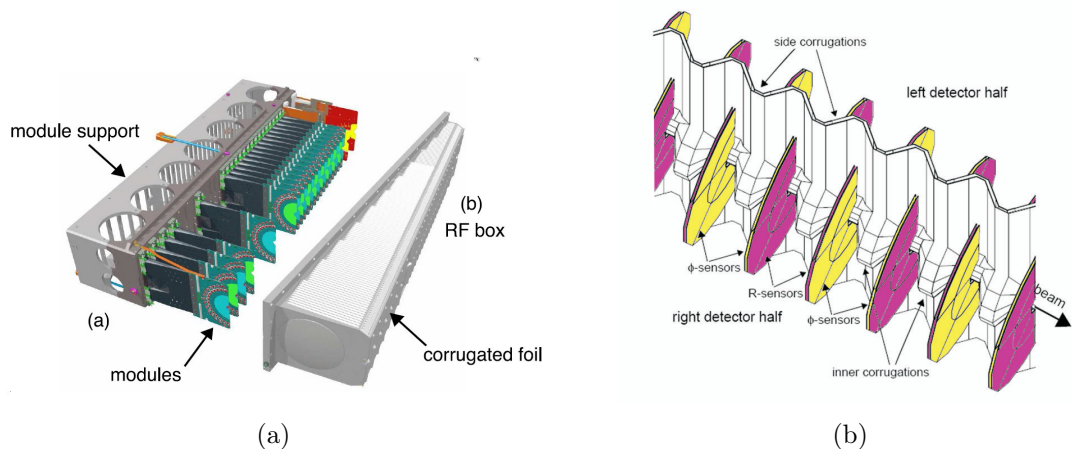


Figure 4.4.: In (a), the VELO modules and the RF box. In (b), the overlap of the RF-foil corrugated faces when the detector halves are in the fully closed position. The other edges of the boxes are cut away. The R and ϕ -sensors are in different colours.

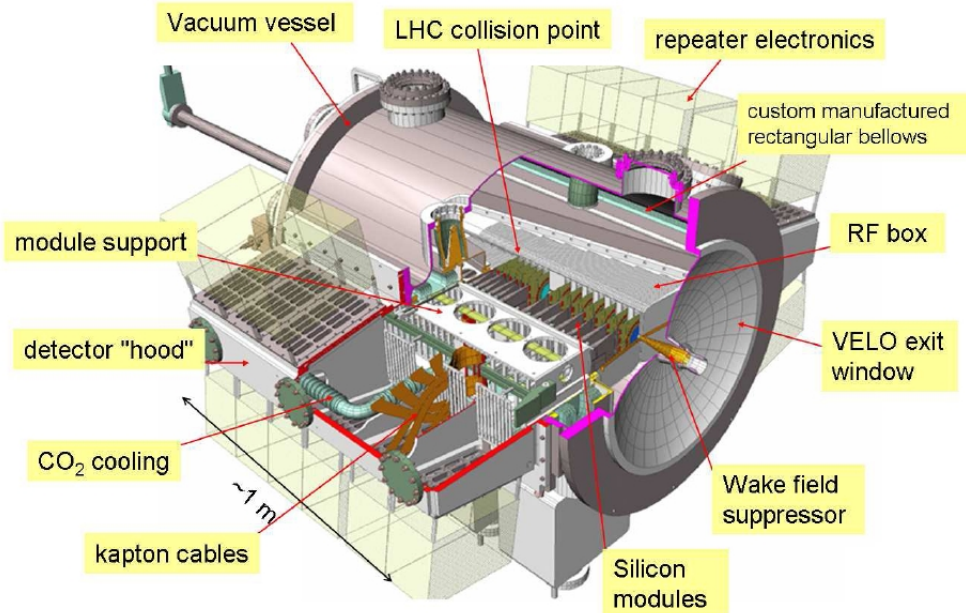


Figure 4.5.: Overview of the VELO vacuum vessel.

4.2.2. Silicon Tracker

The Silicon Tracker consists of two parts: the Tracker Turicensis (TT) (or the Zürich Tracker) and the Inner Tracker (IT). Both TT and IT use silicon micro-strip sensors with a strip pitch of around $200\ \mu\text{m}$. The TT is located about 2 m from the interaction point, upstream of the magnet. The IT is the innermost part of the three tracking stations T1 \div T3, which are placed further away (8 m) from the interaction point, downstream of the magnet. Both IT and TT detectors are in the very high density regions of particles, a high spatial resolution and a fast time response are therefore required. This motivates to choose the silicon micro-strips technology.

Tracker Turicensis

The TT consists of two stations (TTa and TTb) separated by a distance of 27 cm along the z -axis, as shown in figure 4.6. Each station has two silicon layers of 138 \div 150 cm in width and 130 cm in height covering the full acceptance of LHCb. The strips in the four layers are arranged in different ways: in the first and last layers, the strips are vertical; in the second and third layers, the strips are rotated by the stereo angles of -5° and $+5^\circ$ respectively, these angles correspond to u and v coordinates. This arrangement will permit to remove the track amplitudes.

Each layer of TTa station contains 15×2 half-modules while each layer of TTb station contains 17×2 half-modules. The structure of the second layers is shown in figure 4.7(a). Each half-module is a column of seven sensors; for the half-modules closest to the beam,

where the particle density is highest, the seven sensors are divided into three sectors (4 sensors in L sector, 2 sensors in M sector and 1 sensor in K sector), these three sectors are respectively connected to three readout hybrids via Kapton interconnect cables. These half modules are called the 4-2-1 type. For the other half-modules, the seven sensors are organized into two readout sectors (4 sensors in L sector and 3 sensors in M sector). It is called the 4-3 type half module. The 4-2-1 and 4-3 half-modules are presented in figures 4.7(b) and 4.7(c).

The TT silicon sensors are single sided p^+ -on- n sensors. Each sensor is 500 μm in thickness, 9.64 cm in width and 9.44 cm in length; it includes 512 strips with a strip pitch of 183 μm .

The TT stations are vertically split up into two halves. These halves are housed inside light tight, electrically and thermally isolated boxes made of light weight aluminium clad foam. These boxes are mounted on rails and are retractable horizontally in order to avoid the high radiation during the beam injection. The boxes are opened on the ($z - y$) side so that the two halves of a station can join together for whole detector. This structure is shown in figure 4.8. The temperature in the boxes is maintained below +5°C and the boxes are flushed with nitrogen to avoid condensation on the surfaces close to the cooling system.

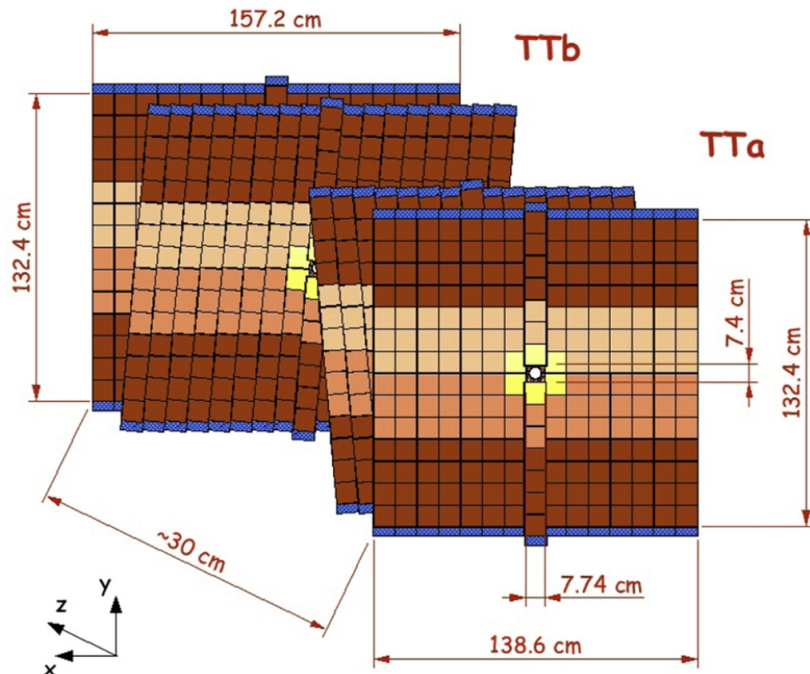


Figure 4.6.: Two stations of the TT.

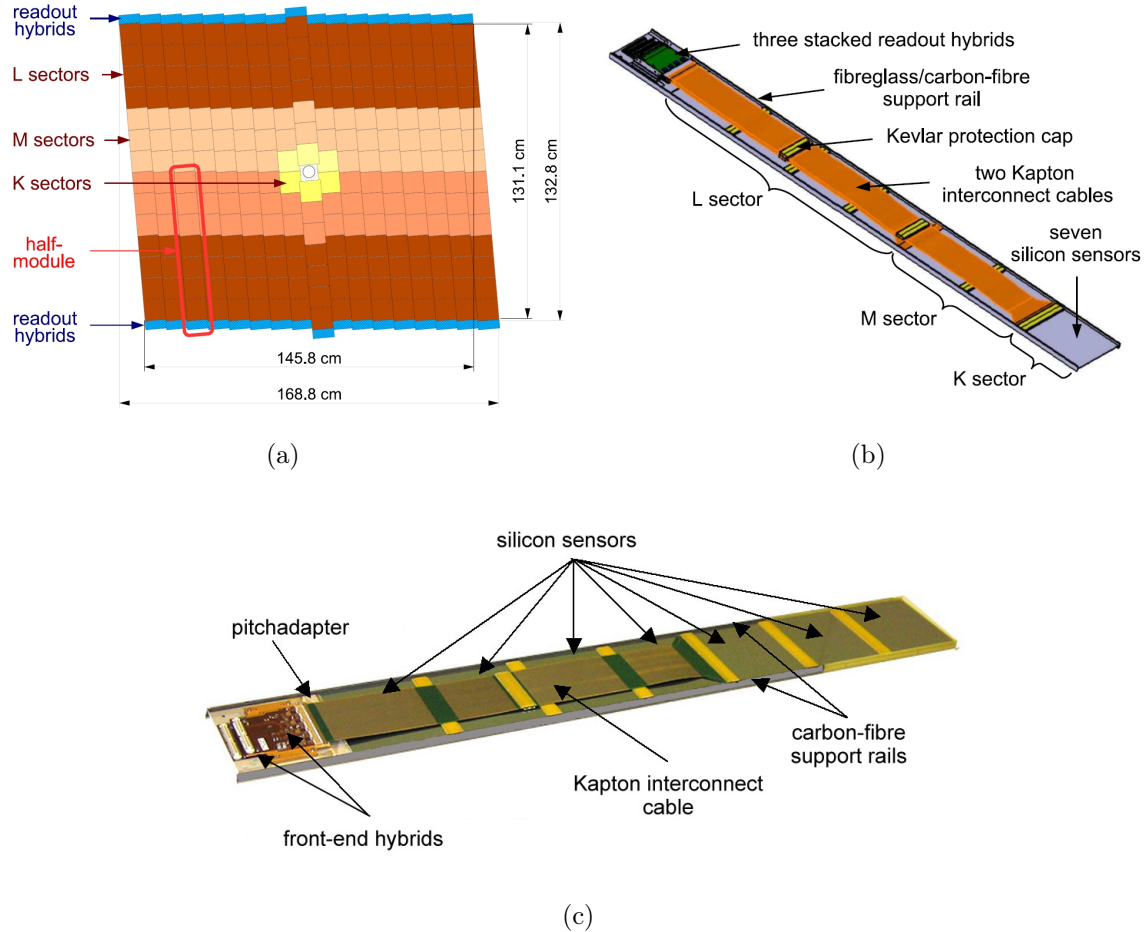


Figure 4.7.: The second layer of TT (a) and the two types of the TT half-modules: the 4-2-1 type in (b) and the 4-3 type in (c).

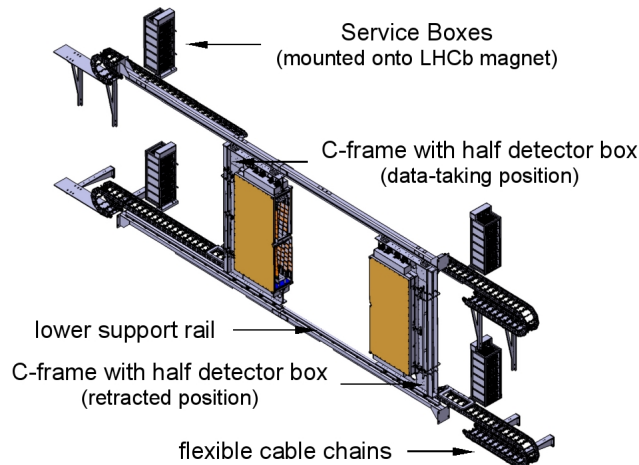


Figure 4.8.: The structure of the TT stations.

Inner Tracker

There are three IT stations close to the beam pipe. Each of them is composed of four individual detector boxes that are placed around the beam pipe as shown in figure 4.9.

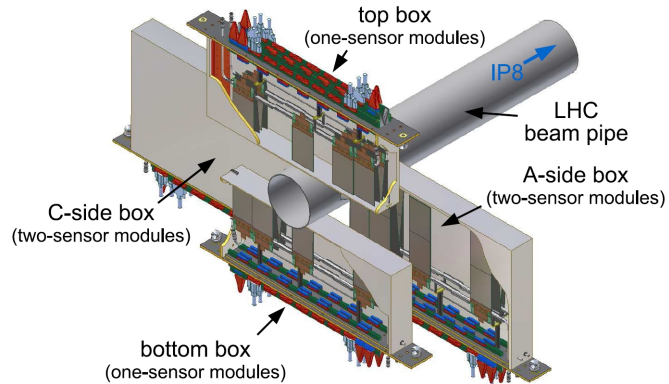


Figure 4.9.: The four individual detector boxes of an IT station.

Similar to the TT boxes, the IT boxes are also electrically, thermally and light tight insulated, maintained below $+5^{\circ}\text{C}$ and flushed by nitrogen. Each detector box has four detection layers arranged in an $x - u - v - x$ topology similar to that in the TT. Each layer has seven detector modules. Figure 4.10 shows the layout of an x and u layers with the silicon modules in the cross-shaped configuration. The modules in the boxes above and below the beampipe consists of a single silicon sensor and a readout hybrid, while the modules inside two boxes on either sides of the beampipe consists of a double of silicon sensors and a readout hybrid. The sensors are single sided p^+ -on- n Si strip detector. Each sensor is 7.6 cm in width and 11 cm in length. The thickness is of 320 μm for the single sensors and of 410 μm for the double sensors to maintain the ratio S/N above 15. Each sensor has 384 readout strips with a strip pitch of 198 μm that results in a resolution of about 57 μm .

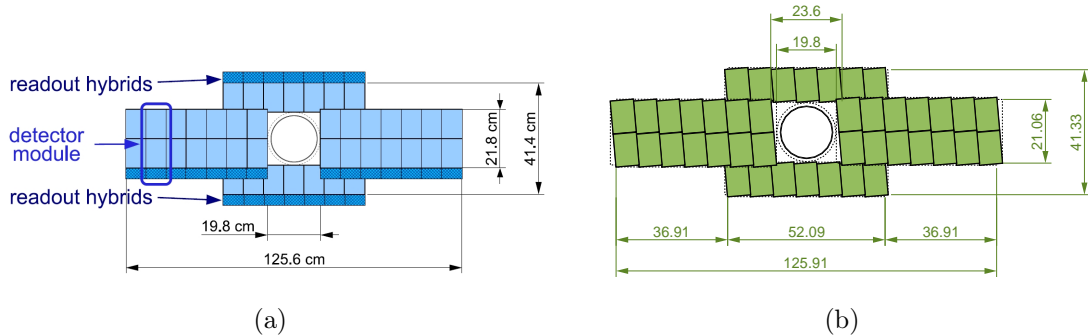


Figure 4.10.: Layouts of the x layer in (a) and of the u layer in (b).

4.2.3. Outer tracker

In the three T stations, the Outer Tracker (OT) covers a large region outside the acceptance of the Inner Tracker. The momentum resolution in the OT is required to be of $\delta_P/P \approx 0.4\%$ for the reconstruction of the b-hadron mass, like $B_s^0 \rightarrow D_s^-\pi^+$. Each station consists of four layers of drift tubes arranged in the $(x - u - v - x)$ configuration as in the TT and IT. Each layer is built from 14 long modules (L) with a size in x and y of $0.34\text{ m} \times 4.85\text{ m}$ and 8 short modules (S1, S2, S3) above and below the IT. This structure is shown in figure 4.11.

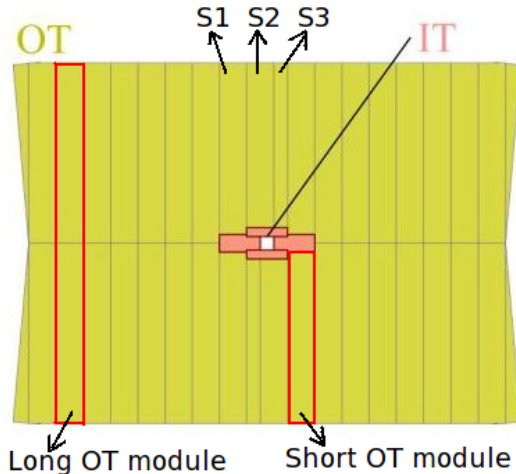


Figure 4.11.: The OT layer composes of 14 long modules and 8 short modules.

The dimensions of S1, S2, S3 modules in x and y dimensions are $0.34\text{ m} \times 2\text{ m}$, $0.34\text{ m} \times 2.2\text{ m}$ and $0.17\text{ m} \times 2.2\text{ m}$, respectively. Each module of a standard width (0.34 m) is made of two staggered layers (monolayers), and each monolayer has 64 drift tubes (or straws). This means that each module of the types S1 or S2 contains 128 straws, each module of type S3 has only 64 straws. For L modules, the monolayers are cut into two parts at the middle of its height, thus each L module contains 256 straws.

Figure 4.12 shows a module of 64 straw tubes. Each straw has an inner diameter of 4.9 mm and a length which is chosen according to its location. The cell wall (the cathode) is made of two windings, the inner one is Kapton-XC, i.e. carbon doped polyimide which is electrically conductive, and the external foil is made of a Kapton-Aluminium laminate composed of $15\text{ }\mu\text{m}$ polyimide and $12.5\text{ }\mu\text{m}$ Aluminium. The anode is a $25.4\text{ }\mu\text{m}$ gold plated tungsten wire. The drift gas is a mixture of Argon (70%) and CO_2 (30%) giving a drift time below 50 ns and a spatial resolution of $200\text{ }\mu\text{m}$ at the nominal working high voltage value of 1500 V. Each monolayer of straw tubes is glued to a sandwich structure made of 10 cm Rohacel and $120\text{ }\mu\text{m}$ Carbon fibre skins.

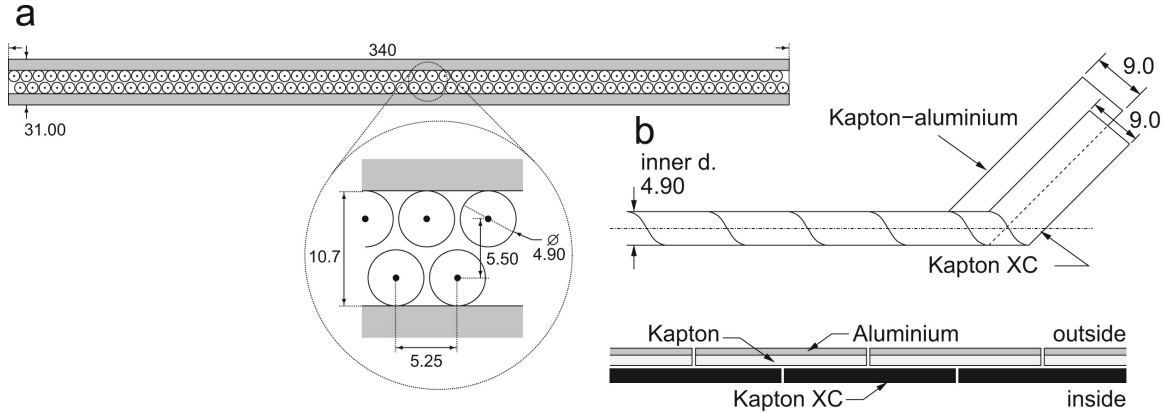


Figure 4.12.: A module of 64 straw tubes in (a); the structure of a straw in (b).

4.2.4. Track reconstruction

For the track reconstruction, all hits in the sub-detectors (VELO, TT, IT and OT) are combined to form the trajectories. First, the initial track candidates are formed from the track segments, called *seeds*, in the VELO and T stations. Then, the trajectories of the tracks are refitted using the Kalman filter method. Depending on the trajectories given by the tracking system, the tracks are divided into five types, as shown in figure 4.13.

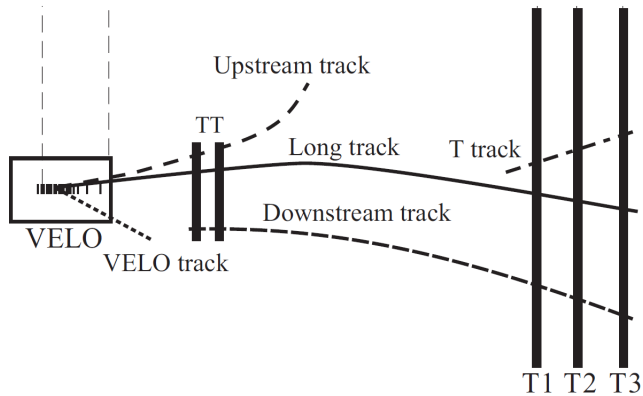


Figure 4.13.: Five track types in LHCb.

- **VELO tracks** traverse the VELO only. They are mainly backward tracks or large polar angle tracks. These tracks are useful for reconstructing the primary vertex.
- **Long tracks** traverse all the trackers, from the VELO to the T stations. Therefore, the measurements of their momentum have the highest accuracy. They are the most important tracks.

- **Upstream tracks** have their hits in the VELO and TT only. Due to their low momentum, they are bent out of the detector acceptance by the magnet field before reaching the T stations.

- **Downstream tracks** have hits in the TT and T stations only. They are the decay products of the particles that decay outside the VELO acceptance.

- **T tracks** have the hits in the T stations only. They can be used for RICH2 pattern reconstruction or for the internal IT/OT alignment.

4.3. The particle identification system

4.3.1. RICH

The Ring Imaging Cherenkov detectors (RICH) are used for particle identification. In LHCb, two RICH detectors are employed depending upon the momentum of the particles.

When a charged particle traverses a medium of refraction index (n) with a velocity (v) greater than the velocity of light in that medium, i.e. $v > c/n$ with c being the velocity of light in vacuum, Cherenkov lights are emitted in a cone. The emission angle θ_c , between the emitted light direction and the particle direction, is given by the formula

$$\cos\theta_c = \frac{1}{n\beta} \quad (4.1)$$

where $\beta = v/c$. Thus, the particle's velocity can be deduced from the measurement of this angle. By using the velocity and the momentum measured by the tracking system, the particle's identification can be achieved. In a medium, the Cherenkov light is only emitted when the particle's speed β is above the threshold $\beta_t = 1/n$. Therefore, the refraction index of the medium is required to be large for the identification of low momentum particles while a small index is more suitable for high momentum particles. In the two RICH detectors of LHCb, three different radiators were chosen for particle identification in a large momentum range: aerogel ($n = 1.03$), C_4F_{10} gas ($n = 1.0014$), CF_4 gas ($n = 1.0005$). Figure 4.14 shows the Cherenkov angle versus particle momentum in the three RICH radiators.

The **RICH1** is placed between the VELO and the TT and covers the full LHCb acceptance from ± 25 mrad to ± 300 mrad in horizontal and ± 250 mrad in vertical. It uses aerogel and C_4F_{10} gas which can identify the charged particles of the momentum range from 1 GeV to 40 GeV. The photons emitted inside the radiators by the tracks are reflected onto the Hybrid Photon Detector (HPD) located outside the LHCb acceptance by a system of spherical and flat mirrors. The schematic layout of the RICH1 is presented in figure 4.15(a).

The **RICH2** is located next to the T3 station. It contains CF_4 gas which allows to identify the charged particles of high momentum, from ~ 15 GeV up to 100 GeV. Since the particles of high momentum are mostly produced in the region around the beam, RICH2 only covers a reduced acceptance from ± 15 mrad to ± 120 mrad horizontally and to ± 100 mrad vertically. As in RICH1, an optical system of spherical and flat mirrors is used to project the photons onto the HPDs placed outside the LHCb acceptance. Figure 4.15(b) shows the layout of the RICH2.

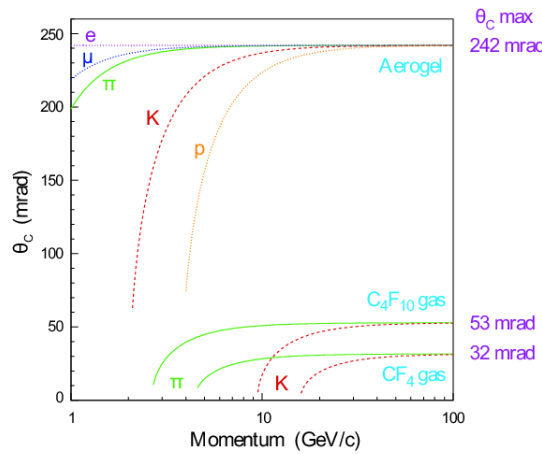


Figure 4.14.: Cherenkov angle versus the particle momentum in the three RICH radiators.

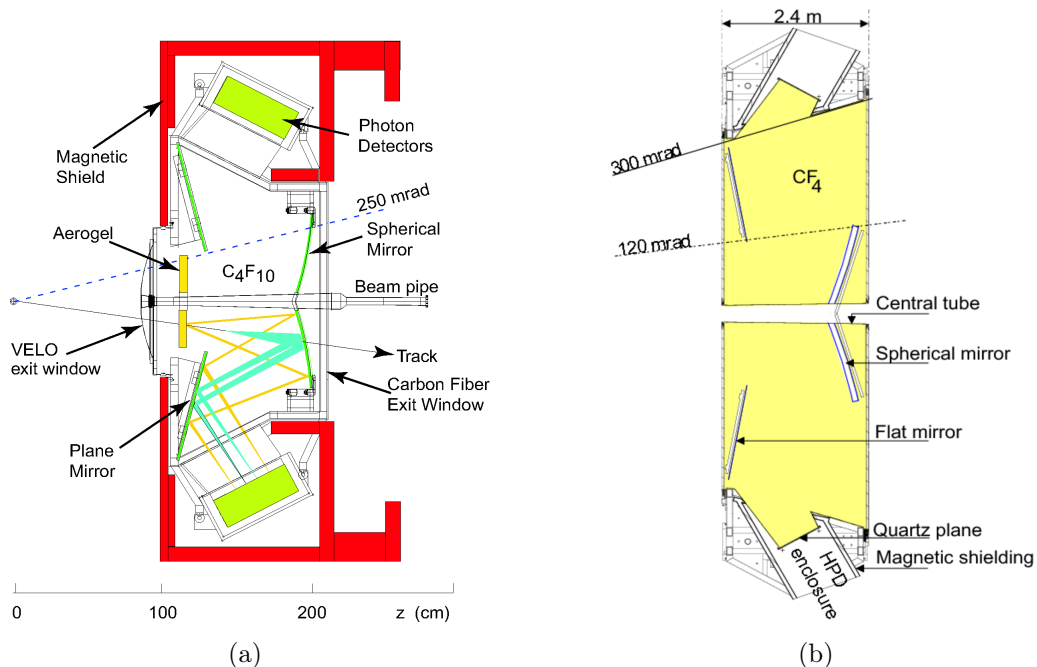


Figure 4.15.: The schematic layouts of the RICH1 in (a) and the RICH2 in (b).

The Hybrid Photon Detector (HPD):

The HPDs are vacuum photon detectors and aim to detect and measure the spatial positions of the emitted Cherenkov photons. They are sensitive to single photons in the wavelength range of 200÷600 nm. The HPD is depicted in figure 4.16(a). It puts together in a single device the photocathode technology and the solid state technology. The Cherenkov photons arriving on the photocathode of the HPD release photoelectrons which are accelerated by a voltage of about -20 kV; these photoelectrons are brought to the silicon array where they dissipate their kinetic energy in the creation of 3000 to 5000 electron-hole pairs. The light pattern which was incident on the photocathode is thus imaged onto the silicon detector by the use of the electrostatic optics. The silicon sensor is segmented in an array of 1024 pixels of size $500\mu\text{m} \times 500\mu\text{m}$ and arranged as a matrix of 32×32 . The photocathode image is de-magnified by a factor of 5 onto the silicon sensor. This corresponds to a pixel size at the HPD entrance window of $2.5 \times 2.5\text{ mm}^2$. The sensor is bump-bonded to the readout chips which provide a preamplifier, a shaper and a discriminator circuit for each pixel.

The total number of HPDs in LHCb is 484, 196 which are in RICH1 and 288 in RICH2. These HPDs cover an area of 3.5 m^2 . Figure 4.16(b) shows the picture of one tube.

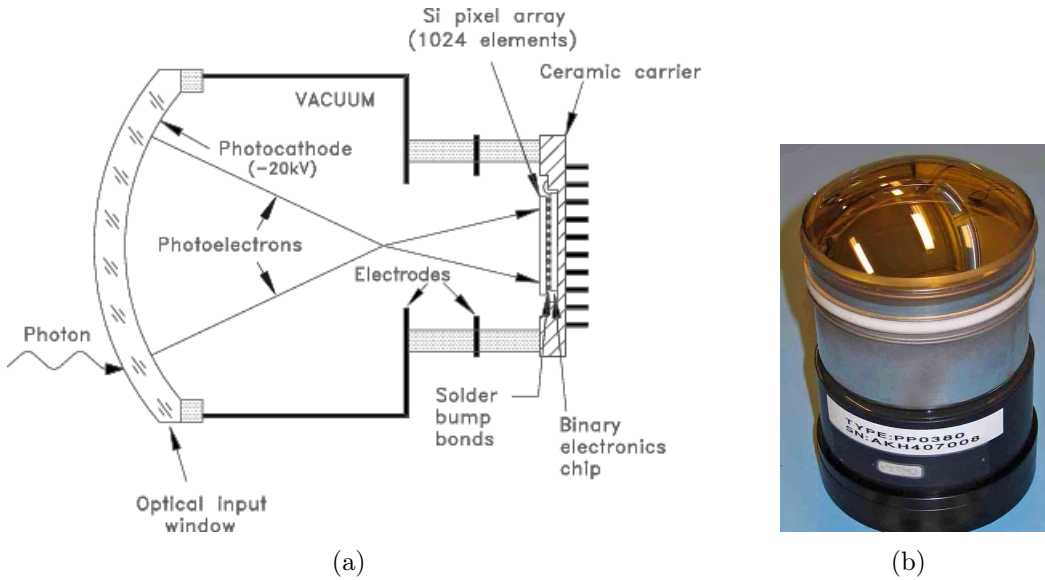


Figure 4.16.: The schema of a HPD in (a); The HPD used for RICHs of LHCb in (b).

Particle identification by RICHs:

Since the photons are generated in a cone whose axis of symmetry is the track, their impact points on the planes of HPDs form a ring whose radius is measured. Finding

the emission point by inverse ray-tracing is impossible because of the spherical focusing mirror, thus this point is assumed to be the middle point of the track segment inside the radiator. In principle, the emission angle may be determined from the ring radius and the emission position, thus allowing to identify the particle. However, in an event, the signal in RICH detector is a set of rings, with many overlaps in the region of high track density. The RICH information is treated globally for an event [23], [24], the starting point being the assumption that all particles in that event are pions. For each individual track the hypothesis is successively changed to e, μ, π, K, p and the "below Cherenkov threshold" particle, the other tracks' hypotheses being unchanged. When the change in the event likelihood is the largest, the mass hypothesis for this track is set. The procedure is repeated until all tracks have been set to their optimal value. The final results are differences in the log-likelihood values (DLL) which give for each track the change in the overall event log-likelihood when the track is changed from pion to muon, electron, kaon, proton and below Cherenkov threshold particle.

4.3.2. Calorimeters

The calorimeters are designed to absorb electrons, photons and hadrons. They provide energy and position measurements of the particles and allow to compute the transverse energy (E_T) that is used in the first trigger level (L0) to select the event of high E_T . In addition, the calorimeters also identify electrons, photons and hadrons.

In principle, when a particle interacts in the detector material, it produces a cascade of secondary particles which forms what is called the particle shower. This shower is finally absorbed by ionisation in the material. The collected signal is proportional to the total deposited energy of the particle. The LHCb calorimeters are sampling calorimeters in which the active materials are scintillators.

For the electromagnetic particles, the shower contains mainly photons, electrons and positrons created by Bremsstrahlung radiation and pair production. The rate of energy loss of particle in the material is given by

$$\frac{dE}{dx} = -\frac{E}{X_0} \quad (4.2)$$

where E is the energy of particle and X_0 is a distance, called *radiation length*, over which a charged particle loses an average 37% of its energy through showering. The radiation length X_0 depends on the mass (m) and charge (z) of incident particle, the density (ρ), the atomic number (Z) and the mass number (A) of the material.

$$X_0 \propto \frac{m^2 A}{\rho z^4 Z^2} \quad (4.3)$$

For hadrons, the shower contains mainly pions and nucleons produced in hadron-nuclei scattering and decay of excited nuclei. The hadronic shower development depends on the nuclear interaction length of material (λ_I).

$$\lambda_I = \frac{35A^{1/3}}{\rho} \quad (4.4)$$

The material chosen for the calorimeters should have the radiation length and the nuclear interaction length as small as possible to ensure the compactness of the detector.

In LHCb, the electromagnetic calorimeter system consists of three different components: the Scintillating Pad Detector (SPD), the Pre-Shower Detector (PS) and the Electromagnetic Calorimeter (ECAL) itself. The Scintillating Pad Detector (SPD) allows to determine whether particles hitting the calorimeter system are charged (electron, hadrons) or neutral (photon). After the SPD, electromagnetic showers from photons and electrons are initiated in a 12 mm thick lead wall ($2.5 X_0$) placed between the SPD and Pre-Shower (PS).

Then, the electromagnetic showers continue to develop in the PS, whereas the hadrons have low probability to create showers. Therefore, detecting this shower of electrons in PS help to discriminate between electrons and hadrons. Finally, the showers of the electrons and the photons continue to develop wide and are absorbed in ECAL.

For the hadrons, their showers can start at the end of ECAL and are absorbed inside HCAL. Figure 4.17 presents the interaction of particles and the evolution of their showers in the calorimeters.

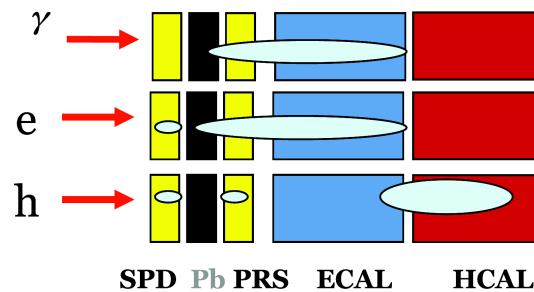


Figure 4.17.: Interaction of particles and the evolution of their showers in the LHCb calorimeter system.

SPD/PS:

Both SPD and PS consist of 15 mm thick scintillator pads. A $2.5 X_0$ lead converter ($\simeq 12$ mm) is sandwiched between the SPD and the PS initiating the electromagnetic showers. The scintillator light in the pads is first wavelength-shifted and then transmitted to the multianode photomultiplier tubes (MAPMT) by the clear fibres placed outside the acceptance. The SPD and PS planes are subdivided into three sections: the inner section (3072 cells of 4 cm \times 4 cm size), the middle section (3584 cells of 6 cm \times 6 cm size) and the outer section (5376 cells of 12 cm \times 12 cm size). The sensitive area of the detectors is 7.6 m wide and 6.2 m high. The total length of both SPD and PS in z -axis is of 18 cm.

ECAL:

The shashlik technology was employed for the ECAL in LHCb: the calorimeter has the sampling scintillator/lead structure which is read out with plastic WLS fibres. This kind of detector provides an adequate energy resolution, fast time response and hard radiation resistance.

The ECAL starts at 12.5 m in z -direction, has a total length of 1.8 m and covers an acceptance from 25 mrad to 300 mrad horizontally and 250 mrad vertically. The ECAL is subdivided into inner, middle and outer sections (see figure 4.18 where a quarter of the ECAL is shown) and is built from individual modules (shown in figure 4.18 as the small squares). Each module is made from 66 lead plates (2 mm) interspaced with scintillator tiles (4 mm thick). The total thickness of a module is 25 radiation lengths and 1.1 interaction length. Wavelength shifting fibres penetrate the entire stack and at the back are fused to clear fibres which bring the signal to the photomultipliers.

As particle density depends upon the distance from the beam pipe, three types of modules containing 3×3 , 2×2 or 1 readout cells for the inner, middle and outer sections, respectively, were used. These three types of modules produced for the ECAL of LHCb are depicted in figure 4.19.

The design resolution of the ECAL is $\sigma_E/E = 10\%/\sqrt{E} \oplus 1.5\%$, the first term of this resolution reflects the stochastic fluctuation, such as the intrinsic shower fluctuation, the photoelectrons statistics. The second term is due to the detector non-uniformity and calibration uncertainties; \oplus means that the two terms have to be added in quadrature, E is expressed in GeV.

HCAL:

The HCAL is positioned behind the ECAL and has a dimension of 8.4 m in height, 6.8 m in width and 1.65 m in length. The HCAL total weight is about 500 tons. The HCAL is subdivided into inner and outer sections as in figure 4.20(a). The HCAL cells have a

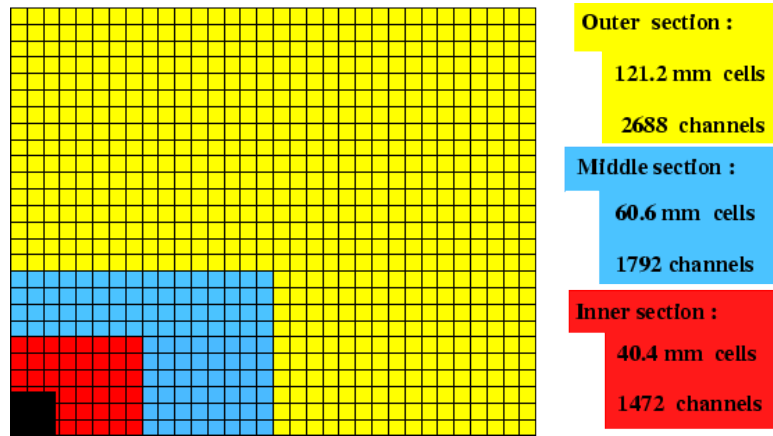


Figure 4.18.: The quarter of ECAL with inner, middle and outer sections.



Figure 4.19.: Three types of modules are used in ECAL.

size of 131.3×131.3 (mm 2) in the inner section and 262.6×262.6 (mm 2) in the outer section. This gives a resolution of $\sigma_E/E = (69 \pm 5)\%/\sqrt{E} \oplus (9 \pm 2)\%$ for HCAL, where E in GeV.

The special characteristic of the HCAL is that the active scintillator tiles are placed parallel to the beam axis. Along this axis we have six 202 mm long rows with interchanging order of iron spaces and scintillator tiles. The scintillator is 4 mm thick and the iron is 1 cm thick. Figure 4.20(b) shows a schematic of a cell structure. As in the ECAL, the scintillator light is captured and transmitted to the PMTs by the WLS fibres that lie along the cell. In the longitudinal direction, the total length of the tiles and iron plates is of $5.6\lambda_I$.

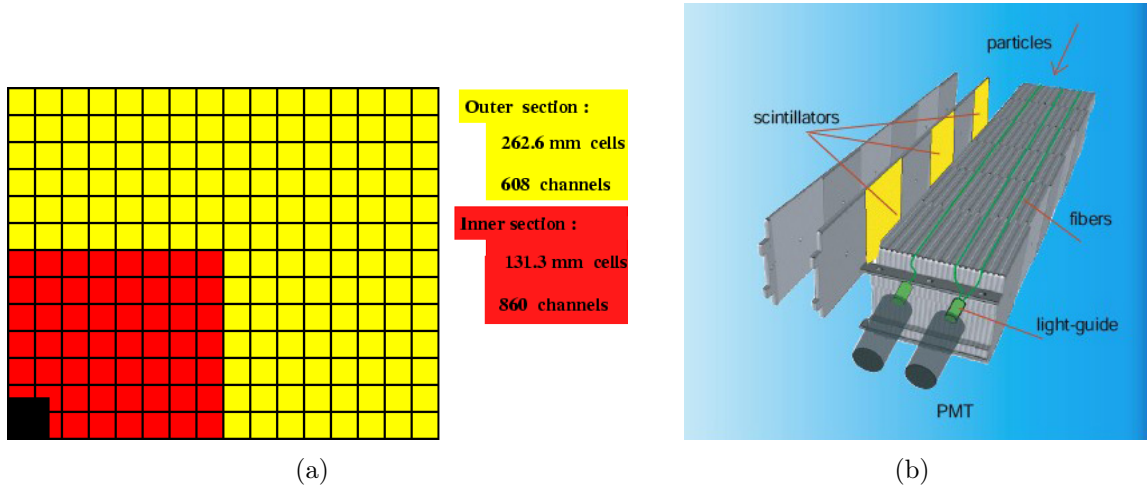


Figure 4.20.: The quarter of HCAL with inner and outer sections in (a); the schematic of the HCAL cell structure in (b).

4.3.3. The muon system

Among the detectable particles, the muons are the only particles which can traverse the whole detector because they only have electromagnetic interactions in matter. Therefore, the muon system is always the outermost part of the spectrometer. In LHCb, there are five muon stations M1 \div M5. M1 is located before the calorimeters to decrease the error on the momentum measurements due to scattering of muons in the calorimeters. M2 \div M5 are placed after the calorimeters and separated by 80 cm thick iron plates to filter any remaining hadronic background. Only the muons with momenta higher than 6 GeV/c cross all the five stations. The order of the muon chambers in z -axis is presented in figure 4.21.

The muon system covers an acceptance from 20 (16) mrad to 306 (258) mrad in horizontal (vertical). The three stations M1 \div M3 have a high horizontal resolution in the bending plane that allows to determine the track direction and to compute the transverse momentum of muon candidate with a resolution of 20%. M4 and M5 have a limited spatial resolution and are used to identify the penetrating particles. The measured P_T is used for high- P_T muon trigger at the first level (L0) and the muon identification is used for high level trigger (HLT) and offline analysis.

Detector technology:

All muon detectors are multi-wire proportional chambers (MWPC), except the inner region of the station M1 which employs the triple-GEM technology because a high particle rate in this region can affect the safety limit for detector ageing.

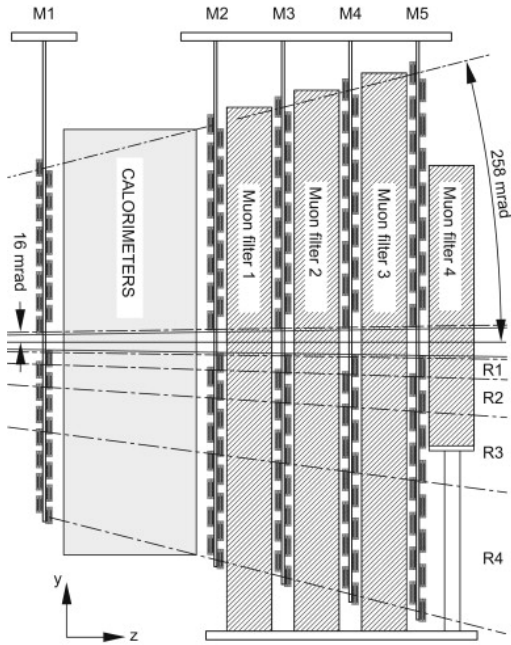


Figure 4.21.: View of the muon system.

MWPC: The total number of MWPCs is 1368. Figure 4.22 shows one quadrant of a station in the xy plane, each rectangle represents one chamber.

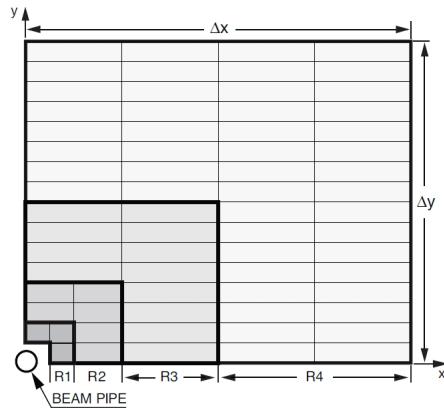


Figure 4.22.: One quadrant of a station in the xy plane, each rectangle represents one chamber.

The MWPCs in M2-M5 are made of five wire panels defining four gaps, as shown in figure 4.23, each gap is 5 mm in width and filled with a gas mixture of Ar/CO₂/CF₄ in a proportion of 40:55:5. In M1, the MWPCs have only three wire panels defining two gaps to minimize the material in front of the calorimeters. The anode wires are made from gold plated tungsten of 30 μm diameter, and are spaced by 2 mm from their neighbours. The spacing between anode and cathode is of 2.5 mm. These MWPCs permit a time

resolution of 5 ns. Thus, a time window of coincidence for all stations smaller than 25 ns as required by the beam coming rate is possible.

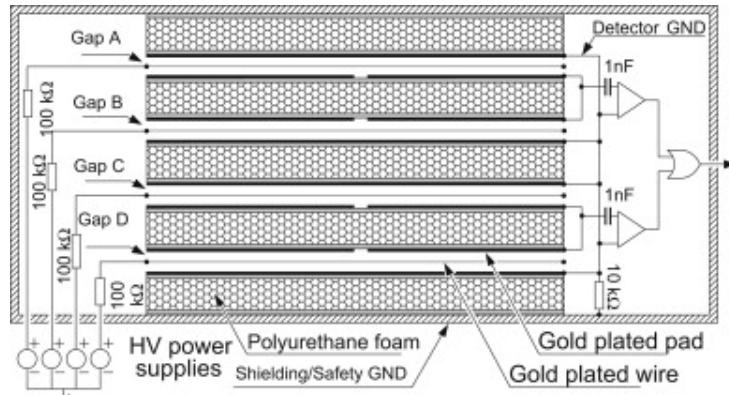


Figure 4.23.: Cross section of MWPC showing the five panels defining four gaps.

Gas Electron Multiplier (GEM) detector: The triple-GEM detector is made from three GEM foils sandwiched between anode and cathode planes. The schematic cross section of the triple-GEM detector is shown in figure 4.24.

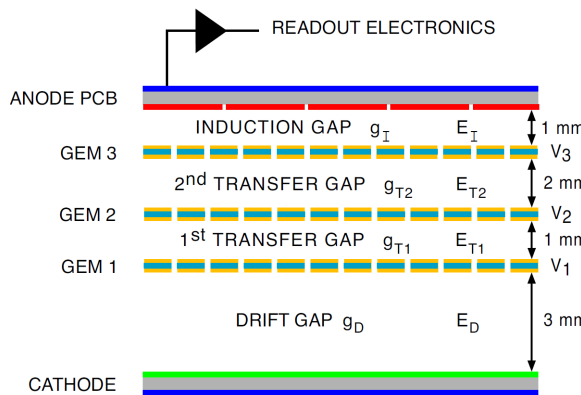


Figure 4.24.: Cross section of the strip-GEM chamber.

The GEM foils are made from 50 μm thick Kapton with two sides coated by 5 μm of copper. The gas used in this detector is a mixture Ar/CO₂/CF₄ with a ratio 45:15:40, this allows a time resolution better than 3 ns. The ionisation electrons produced in the drift gap are attracted and multiplied by electric fields through three GEM foils. When these electrons cross the last GEM foil, they drift to the anode, where the signal is recorded.

Muon identification:

For each long track reconstructed by the tracking system, we extrapolate this track and search for the hits around the extrapolated segment in the "Field of Interest" (FOI) in the muon stations, the "Field of Interest" being the region around the intersections of the extrapolated segment of track with these stations. The stations which are required to have at least one hit in the FOI depend on the muon momentum range. Table 4.1 lists the detailed requirements [25].

Momentum (GeV/c)	Required muon stations
$3 < P < 6$	M2 + M3
$6 < P < 10$	M2 + M3 + (M4 or M5)
$P > 10$	M2 + M3 + M4 + M5

Table 4.1.: The muon stations are required to have hits in the FOI in order to identify muons.

4.4. Trigger

For pp collisions at 14 TeV, the cross-section of $b\bar{b}$ pair production ($\sigma_{b\bar{b}}$) is around 500 μb while the inelastic cross section (σ_{inel}) is 80 mb . The LHCb detector operates at an average luminosity of $2 \times 10^{32} \text{cm}^{-2}\text{s}^{-1}$. This means that the inelastic pp collisions take place at a rate of 16 MHz, whereas the rate of $b\bar{b}$ pairs is about 100 kHz.

In LHCb, visible pp interactions are defined as collisions producing at least two charged particles with sufficient informations in the VELO and T stations to be reconstructed. They correspond to about $\sim 79\%$ of the inelastic rate, i.e. 12.7 MHz.

The events cannot be written to the storage at such 16 MHz or 12.7 MHz rate because they will occupy a huge data volume, and in addition, most of them are uninteresting background while the fraction that contains the B decays in which we are interested is very small. Hence, we need to reduce the data volume, in other words, we have to select the data part of signal and reject the huge part of background. In LHCb, this task is achieved by a trigger system with two levels: Level-0 (L0) and High Level Trigger (HLT). The input and output rates for two levels are listed in table 4.2.

How do we trigger on B decays? Since the B mesons have a large mass, they produce the decay products with a high transverse momentum (p_T) and transverse energy (E_T). In addition, the long B lifetime allows to produce the tracks with a large impact parameter with respect to the primary vertex. The trigger system will look for events having these characteristics.

Level	input rate	output rate
L0	16 MHz	1 MHz
HLT	1 MHz	3 kHz

Table 4.2.: The input and output rates for three levels.

✓ **Level 0 trigger (L0)** aims to reduce the rate of 16 MHz (crossing rate) to a rate of around 1 MHz that can be handled by the DAQ, while keeping a high efficiency for B events. The L0 contains the decision unit which receives the information from the VELO pile-up system, the L0 calorimeter trigger and the L0 muon trigger, then makes the L0 trigger decision.

Purpose of the pile-up system is to veto the multiple visible interactions. It uses four r -sensors of the two VETO stations placed upstream the VELO to measure the radial position of backward tracks. It reconstructs the positions of the primary vertex candidates along the beam line and counts the backward track multiplicity. The number of hits in two stations are counted for each vertex to chose a vertex having the second highest number of hits. Then, the number of tracks in this vertex and the multiplicity are sent to the decision unit.

The L0 calorimeter trigger selects the high E_T particles based on the sum of energy deposits in clusters of 2×2 cells in the ECAL and HCAL. The types of the particles (photon, electron or hadron) are also identified by calorimeters. Then, for each type of particles, the largest cluster is sent to the decision unit.

The L0 muon trigger selects the muon track of high p_T . For each quadrant, the two muon candidates of highest p_T are sent to the decision unit.

The decision unit uses the information sent from the three trigger sub-systems to decide to accept an event or to reject it.

The L0 is implemented in the hardware of the detector. The time delay between a pp interaction and the corresponding L0 trigger decision is $4 \mu\text{s}$. This time includes the time of flight of the particles, the cable delays, the delays in the front-end electronic ($2\mu\text{s}$), the time for processing data in the L0 trigger ($2\mu\text{s}$).

✓ **High Level Trigger (HLT)** is a software trigger; it is an C++ application, called *Moore*, which runs on about 2000 computing nodes of the Event Filter Farm. The HLT uses all the information of an event sent from the L0 output to execute the selection algorithm. The HLT is composed of two levels: HLT1 and HLT2.

Purpose of the HLT1 is to confirm the trigger on high p_T particle sent by the L0 trigger. Using more information in the regions around the candidate direction from the VELO and trackers, the HLT reconstructs the track and sees if the particle candidate matches with the track. The position of the primary vertex, the momentum of the tracks and the impact parameter (IP) with respect to the primary vertex are also reconstructed.

As said before, the track of the particle candidate has to have a large IP to match with the B decay products. Therefore, for B decays the HLT1 will select the events with at least one track which has a high p and a high p_T , a good track quality and large IP. The HLT1 receives an input rate of 1 MHz and gives an output rate of 50 kHz.

The HLT2 runs a complete reconstruction of the events. It searches for displaced vertices by using tracks in the Velo as seeds. Then, it applies the cuts on the invariant mass or the IP to reduce the output rate to the level at which the event can be written to the storage. The HLT2 receives an input rate of 50 kHz and gives out an output rate of 3 kHz.

4.5. Analysis framework and applications

All LHCb applications [26] for data processing are implemented in the GAUDI framework which provides the necessary interfaces and services for these applications. The different applications address the event generation, the detector and interaction simulations, the digitisation, the trigger, the reconstruction, the physics analysis and the visualization. These applications can be combined together or used individually.

✓ **LHCb project** is built on top of the Gaudi framework. It includes the general purpose classes that are used throughout the LHCb applications. These classes are for the general purpose main program and standard options, the core base classes, the event data model, the detector description and conditions, etc.

In LHCb, all the applications (Gauss, Boole, Brunel, DaVinci and Panoramix) are based on the Gaudi framework and on the LHCb project.

✓ **Gauss** mimics what will happen in LHCb detector to allow to understand the experimental conditions and the performance of the detector. It consists of two independent phases: generation and simulation. The generator phase use Pythia program to generate the event by simulating the pp collision. For the produced b-hadrons, their decays are controlled by the EvtGen program. The simulation phase uses Geant4 toolkit to simulate the interactions of particles with materials of the detector, the tracing of charged particles in the magnet field and the decay of short lifetime particles. Pythia, EvtGen and Geant4 are all controlled by GAUSS. However the two generation and simulation phases can be used separately.

✓ **Boole**: In real world, the output of the detector electronic system is an electrical signal. Therefore, in order to simulate the real data, the energy depositions of the particles during their crossing of the sensitive materials need to be digitized into the electrical signals. This task is achieved by the Boole application.

✓ **Moore** is the High Level Trigger application. For real data, Moore can run either online on the trigger farm that processes the online data from the LHCb DAQ system,

or in the offline reconstruction. For MC data, it can run after the output of the detector digitization (Boole).

✓ **Brunel** is the event reconstruction application for LHCb. Its task is to reconstruct the tracks and to identify the particles.

✓ **DaVinci** is the physics analysis application for LHCb. From the reconstructed tracks and identified particles given by Brunel, DaVinci will reconstruct the decayed particles and the decay vertices, the primary vertices. This allows to reconstruct the entire event.

✓ **Panoramix** is an application for the graphic display of the event. This application can be used after or parallel with any other application in the simulation and reconstruction sequence.

Part III.

Monte-Carlo and Results

Chapter 5.

Monte-Carlo

We have seen in chapter 2 that the staus do not have any interactions other than the electromagnetic one. In the standard world, the only charged and long-lived particles which only have electromagnetic interactions with the atoms of the medium are electrons and muons. Since the electrons have a very light mass, leading to strong Bremsstrahlung, the only standard particles which can be compared to the staus are the muons. Moreover, if the high energy staus are long-lived enough to decay outside of the detector volume, the main background that we have to face in a stau search will therefore be the muons.

In this chapter, we will present the Monte-Carlo study for staus and muons. We will start with the calculation of the stau mass and its lifetime, next consider the production of stau pairs in pp collisions and their simulation in the LHCb detector. Then, we will identify the background source to stau pairs and have a detailed look at the responses of the sub-detector to the staus and its background, as well as their characteristics in the event. Finally, we will give a series of cuts to select stau pairs and the corresponding selection efficiencies.

5.1. Generation of stau pairs in pp collisions

The mGMSB stau's mass and lifetime:

In section 2.4 we have shown that the mGMSB depends on six parameters: the scale at which the SUSY breaking happens (Λ), the mass scale of the messengers (M_m), the number of the messenger supermultiplets (N_5), the ratio of the two vacuum expectation values of the two Higgs ($\tan \beta$), the sign of Higgs mass term ($\text{sgn}\mu$) and the decay constant ($\sqrt{\langle F \rangle / k}$). For large $\tan \beta$, the NLSP is the stau and it can be long-lived (see section 2.4.3). Using the above mentioned six parameters and the Spheno program [27], we can generate the masses and the lifetimes of the superparticles of the mGMSB model. The table 5.1 shows these parameters as proposed in the SPS7 benchmark [28] and the corresponding masses and lifetimes of the staus.

Λ (TeV)	M_m (TeV)	N_5	$\tan\beta$	$\text{sign}(\mu)$	$1/k$ (TeV)	$m_{\tilde{\tau}}$ (GeV/c ²)	lifetime (ns)
40	80	3	15	1	4000	124	182
50	100	3	15	1	4000	154	150
60	120	3	15	1	4000	185	125
70	140	3	15	1	4000	216	107
80	160	3	15	1	4000	247	98
90	180	3	15	1	4000	278	83
100	200	3	15	1	4000	309	75

Table 5.1.: The six GMSB parameters and the corresponding masses and lifetimes of staus.

Generation of stau pairs in pp collisions:

Staus are produced in pairs and these pairs will be generated, simulated and reconstructed by LHCb software which was presented in the second part of this manuscript. The stau pairs originate from fermion and antifermion annihilation.

Generator phase: This step uses the above masses of the staus as input for the generation program PYTHIA [29]. PYTHIA generates the stau pairs at LO in pp collisions [12] at a centre-of-mass energy $\sqrt{s} = 7$ TeV for Monte-Carlo 11 (MC11) and $\sqrt{s} = 8$ TeV for MC12. The parton distribution function (PDF) CTEQ5L [30] was used in PYTHIA.

For the calculations, we will use the cross sections for stau pair production calculated by the program Prospino2.1 [31], [32]. Prospino2.1 is a program which computes the cross sections at next-to-leading order for the production of supersymmetric particles at hadron colliders. The program is written for the collisions at both LHC and Tevatron. In this work, a special Prospino2.1 version that was developed by the ATLAS collaboration has been employed. This allows the estimation of the cross sections and their uncertainties by varying the parton distribution CTEQ6.6 [33], the scale factor and the strong coupling. The original version only permits to compute the cross sections and the uncertainties by varying the scale factor. Table 5.2 shows the cross sections for stau pair production in the full acceptance corresponding to different stau masses at the center of mass energies $\sqrt{s} = 7$ TeV and 8 TeV. The cross sections are in femto-barns. The statistical and systematic uncertainties are relative, i.e. expressed in percentage (%).

Since the LHCb detector is designed for an acceptance of $1.9 < \eta < 4.9$ ($\eta = -\ln(\tan(\frac{\theta}{2}))$) and as we demand that both staus enter the detector, an acceptance factor (A) must be defined as the ratio between the number of stau pairs entering into the LHCb detector's acceptance and the number of stau pairs generated in 4π . These factors are estimated using PYTHIA and are given in table 5.3. This factor decreases for higher stau masses.

$m_{\tilde{\tau}}$ (GeV/c ²)	σ (fb) at $\sqrt{s} = 7$ TeV	σ (fb) at $\sqrt{s} = 8$ TeV
124	16.90 ± 0.07 (stat) $^{+5.0}_{-4.4}$ (syst)	21.20 ± 0.07 $^{+3.8}_{-4.8}$
154	7.19 ± 0.07 $^{+6.1}_{-4.6}$	9.20 ± 0.07 $^{+5.6}_{-4.3}$
185	3.44 ± 0.07 $^{+6.6}_{-4.9}$	4.50 ± 0.07 $^{+5.9}_{-4.7}$
216	1.79 ± 0.07 $^{+6.8}_{-5.3}$	2.39 ± 0.07 $^{+6.7}_{-4.8}$
247	1.0 ± 0.07 $^{+7.5}_{-5.8}$	1.35 ± 0.07 $^{+7.1}_{-5.4}$
278	0.57 ± 0.07 $^{+7.6}_{-6.2}$	0.80 ± 0.07 $^{+7.0}_{-5.9}$
309	0.34 ± 0.07 $^{+8.6}_{-6.0}$	0.49 ± 0.07 $^{+7.9}_{-5.9}$

Table 5.2.: Cross sections of the stau pair production at NLO in pp collisions of $\sqrt{s} = 7$ and 8 TeV in full acceptance.

$m_{\tilde{\tau}}$ (GeV/c ²)	124	154	185	216	247	278	309
at $\sqrt{s} = 7$ TeV (%)	8.9	6.9	5.5	4.5	3.7	3.0	2.6
at $\sqrt{s} = 8$ TeV (%)	10.12	8.10	6.52	5.40	4.47	3.76	3.2

Table 5.3.: Acceptance factors of the stau pair in pp collisions of $\sqrt{s} = 7$ and 8 TeV.

Some characteristics of staus with the masses of 124 and 309 GeV/c² are presented here:

a) Invariant mass of stau pairs: In figure 5.1, the invariant masses of the stau pairs are displayed. Here, the masses of the pairs are calculated with the generated true mass of staus.

c) Velocity: The velocity distributions (β) are presented in figure 5.2. The distributions show that most of the staus can reach the outermost muon chamber following a muon in the LHCb inter-spill time of 25 ns.

d) Kinetic variables: The stau tracks possess very high momentum and transverse momentum as shown in figure 5.3 and this has some consequences as we will see.

b) Pseudorapidity: Figure 5.4 shows the distributions of the pseudorapidity (η) for staus produced in the LHCb acceptance. For the high masses, individual stau tends to be produced with a large angle with respect to the beam direction and that explains the drop in the acceptance for high stau masses.

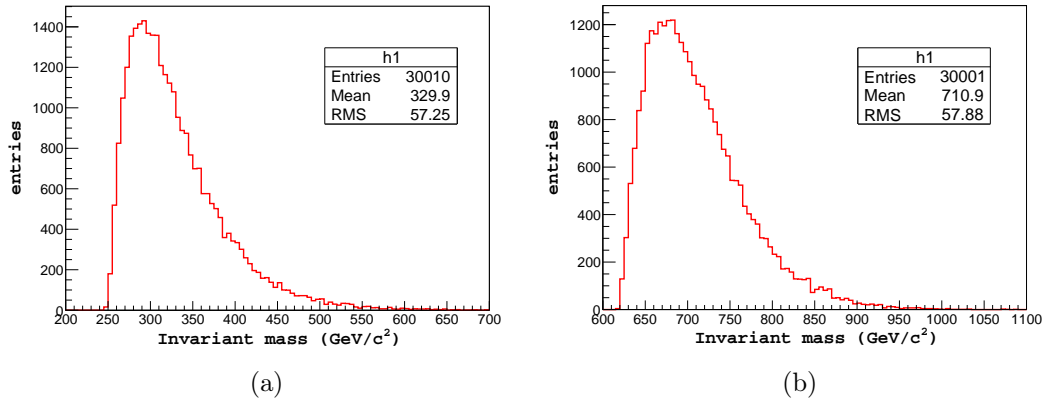


Figure 5.1.: Invariant masses of the stau pairs. Figures (a) and (b) correspond to the two masses of 124 and 309 GeV/c² respectively.

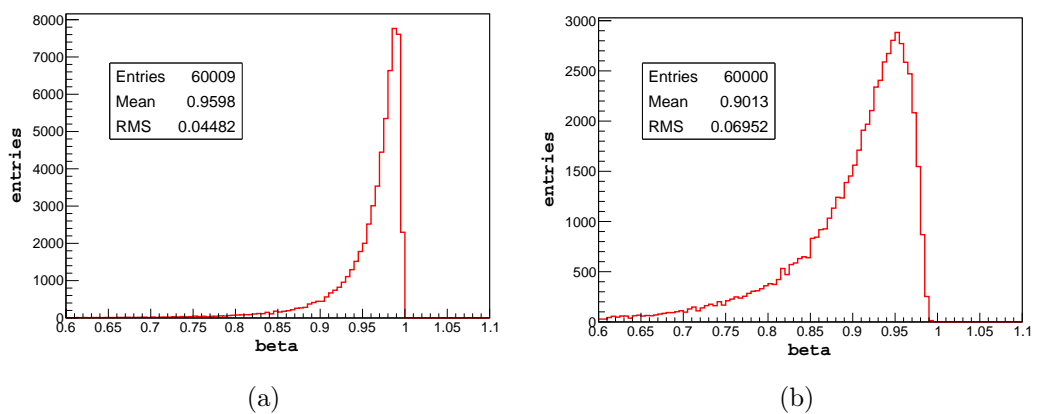


Figure 5.2.: Velocity of the staus generated in pp collisions at 7 TeV. The stau masses are 124 GeV/c² and 309 GeV/c² in figure (a) and (b) respectively.

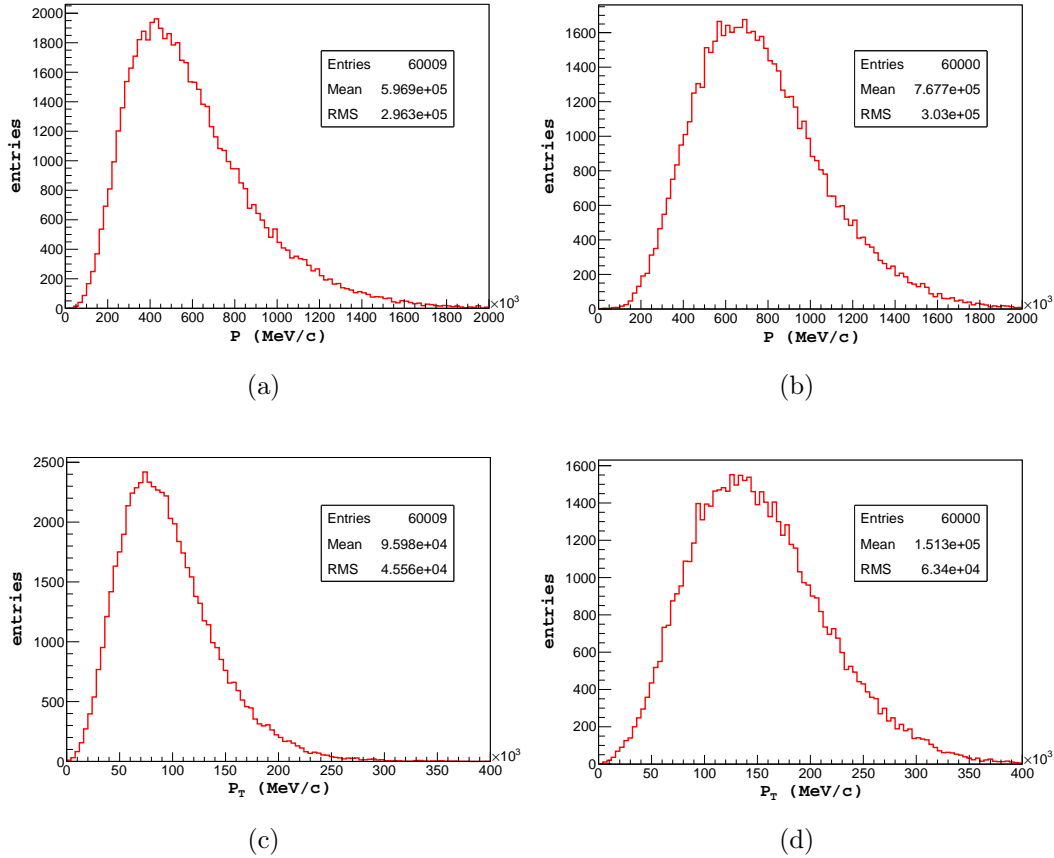


Figure 5.3.: P and P_T of the staus generated in pp collisions at $\sqrt{s} = 7$ TeV, figures (a, c) and (b, d) correspond to the staus of 124 and 309 GeV/c^2 .

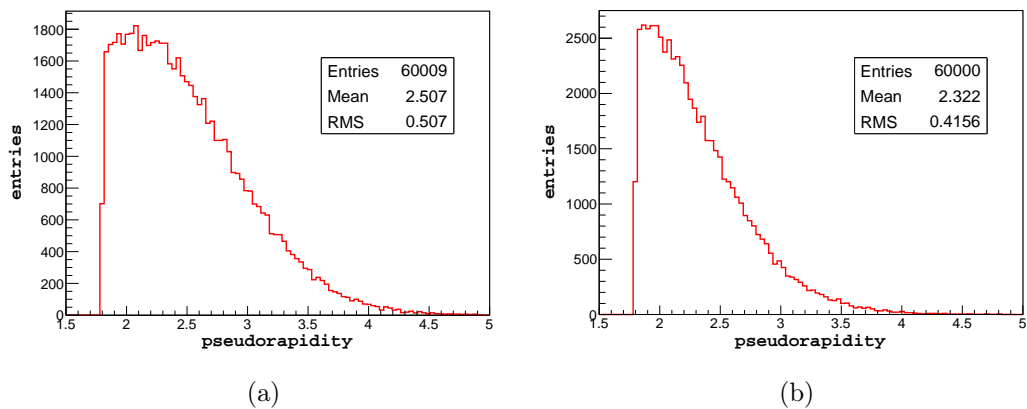


Figure 5.4.: Distributions of the pseudorapidity (η) for staus of 124 GeV/c^2 mass (a) and of 309 GeV/c^2 mass (b) passing through the LHCb acceptance.

5.2. Simulation of staus and their backgrounds

The simulation of stau interactions in the LHCb detector is achieved with the Geant4 program [34] which is implemented in the LHCb software. Since the staus have only electromagnetic interactions in media (see section 2.4.3), the following processes were assigned to them: multiple scattering, ionization and Cherenkov effect. Bremsstrahlung of staus can be neglected because of their mass. The staus are therefore believed to have the same interactions in the detector as muons, except for the radiation.

In this thesis, we study the stau pairs which are produced directly in the pp collisions with both staus entering into the LHCb detector. We simulated the stau events for the seven different masses given in table 5.1.

5.2.1. Identification by the muon chambers

As mentioned above, staus have the same interactions as muon's in the detector and have a lifetime long enough to travel through the LHCb detector. Therefore, stau tracks should be identified as muon tracks in the muon chambers and this is the main criteria for the stau search. By examining the reconstruction of staus in the MC samples, we see that the variable *IsMuon* has been always set to 1 for stau tracks. Therefore, the background to stau pairs are the muon pairs of high energies from the decay $Z, \gamma^* \rightarrow \mu^+ \mu^-$.

5.2.2. Backgrounds and a first attempt to reduce them

In this section, we will indicate the domain of the decay $Z, \gamma^* \rightarrow \mu^+ \mu^-$ that will affect the stau search. As we do not know the true mass of the stau *a priori*, when we calculate the invariant masses of the stau pairs, we will use the muon mass for the staus. By using the muon mass instead of using the generated mass of 124 GeV/c², the stau pairs will have an invariant mass distribution in figure 5.5(a). Figure 5.5(b) shows the invariant mass distribution of the decay $Z, \gamma^* \rightarrow \mu^+ \mu^-$ from the data taken by the LHCb detector in 2011. This distribution is dominated by the Z peak at about 91 GeV/c² with a cross section of about 75 pb for muon pairs inside the LHCb acceptance at 7 TeV pp collisions [35], while the cross section for the stau pair production is much lower (see table 5.2). By comparing the two histograms of figure 5.5, we see that only the domain of the invariant mass $M_{\mu\mu} > 100$ GeV/c² of the decay $Z, \gamma^* \rightarrow \mu^+ \mu^-$ will significantly affect the stau's signals.

Figure 5.6(a) shows the transverse momentum distribution of the staus with a mass of 124 GeV/c². Most of the stau's P_T are higher than 50 GeV/c, while most of muons from $Z, \gamma^* \rightarrow \mu^+ \mu^-$ are less than 50 GeV/c (figure 5.6(b)). Hence, the background $Z, \gamma^* \rightarrow \mu^+ \mu^-$ can be further reduced by requiring that each muon of the pair has a transverse momentum larger than 50 GeV/c.

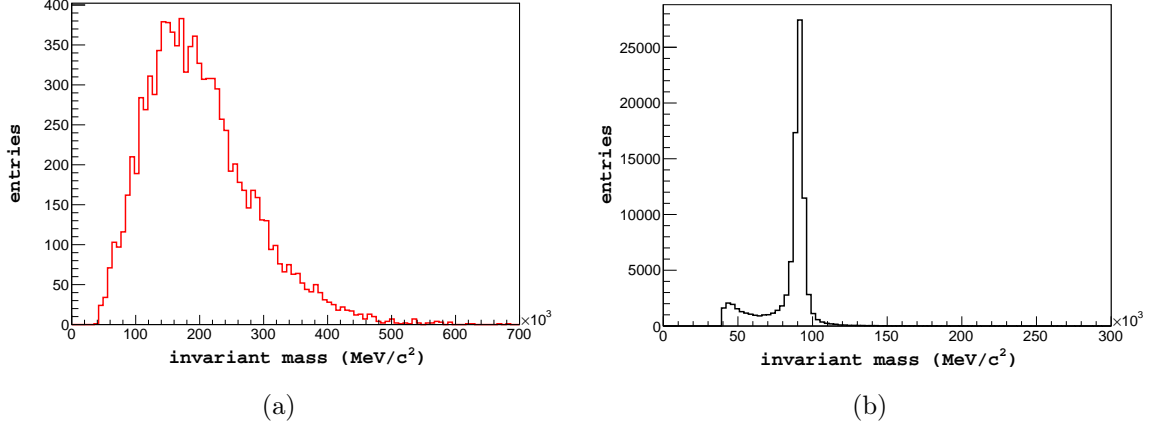


Figure 5.5.: Invariant mass distribution of stau pairs using the muon's mass (the true mass of the generated stau is 124 GeV/c²) in (a). Distribution of $Z, \gamma^* \rightarrow \mu^+ \mu^-$ decay selected from the 2011 data is shown in (b).

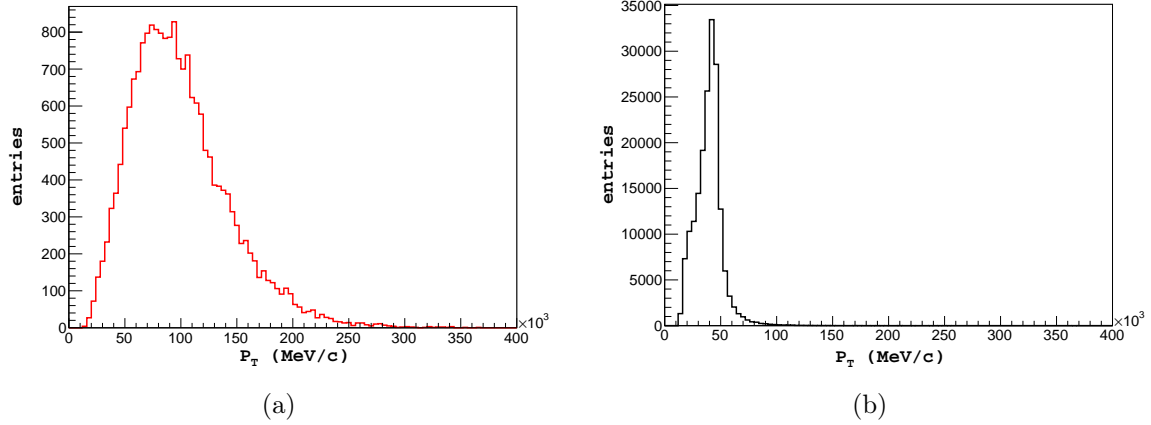


Figure 5.6.: P_T distribution of 124 GeV/c² staus in (a) and the one of real muons in (b).

In the domain: $M_{Z^0, \gamma^*} > 100$ GeV/c², $P_T^{\mu^\pm} > 50$ GeV/c, $1.9 < \eta_{\mu^\pm} < 4.9$, the theoretical estimations of the cross section for the $Z, \gamma^* \rightarrow \mu^+ \mu^-$ background are given in table 5.4. The cross section is calculated at $\sqrt{s} = 7$ TeV by the program DYNNLO [36] and at $\sqrt{s} = 8$ TeV by the program FEWZ [37]. Both programs use the parton distribution function MSTW08 [38].

	cross section (σ) (pb)		
at $\sqrt{s} = 7$ TeV	1.065	$+0.03$	$+0.07$
at $\sqrt{s} = 8$ TeV	1.24	$+0.04$	$+0.08$
		-0.02	-0.06
		-0.03	-0.06

Table 5.4.: Cross section for the decay $Z, \gamma^* \rightarrow \mu^+ \mu^-$ in pp collisions. The first uncertainty is from the choice of PDF, the second one is from the theory.

5.2.3. Triggering and stripping

Stripping: The stripping line of the decay $Z, \gamma^* \rightarrow \mu^+ \mu^-$ ($Z02MuMu$) is suitable to select the stau having the characteristics "like muons" in the detector. This line requires two opposite charged muons with an invariant mass $M_{Z^0, \gamma^*} > 40$ GeV/c 2 . This line demands each muon to have $P_T > 15$ GeV/c in the stripping 17 for 2011 data and $P_T > 3$ GeV/c in the stripping 20 for 2012 data.

Trigger: The staus and their muon background have large transverse momenta, therefore we will demand that at least one track of the pair has fired the trigger on single muon of high P_T with the three trigger lines: *L0Muon*, *Hlt1SingleMuonHighPT* and *Hlt2SingleMuonHighPT*. The *L0Muon* will require a muon with $P_T > 1.48$ GeV/c in 2011 [39] and $P_T > 1.76$ GeV/c in 2012 [40]. The *Hlt1SingleMuonHighPT* requires a muon with $P_T > 4.8$ GeV/c, while the *Hlt2SingleMuonHighPT* requires a muon with $P_T > 10$ GeV/c in both 2011 and 2012 [39], [40].

5.2.4. Reconstruction of the tracks

As stau pairs come from the primary vertex and can attain the outermost muon chamber, stau tracks should be reconstructed as long tracks. In order to ensure the track quality, the cuts on chi-square per degree of freedom ($\chi^2/\text{dof} < 3$) and relative momentum resolution ($\sigma_P/P < 0.1$) are applied. The distributions of these variables are shown in figures 5.7 and 5.8 for staus of $124 \text{ GeV}/c^2$ and $309 \text{ GeV}/c^2$ masses.

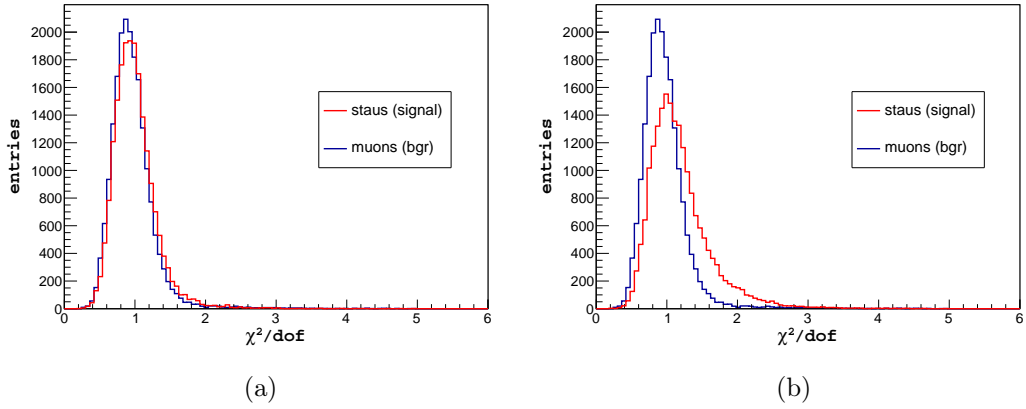


Figure 5.7.: The chi-square per degree of freedom (χ^2/dof) is shown for staus of $124 \text{ GeV}/c^2$ mass (figure (a)) and for staus of $309 \text{ GeV}/c^2$ mass (figure (b)).

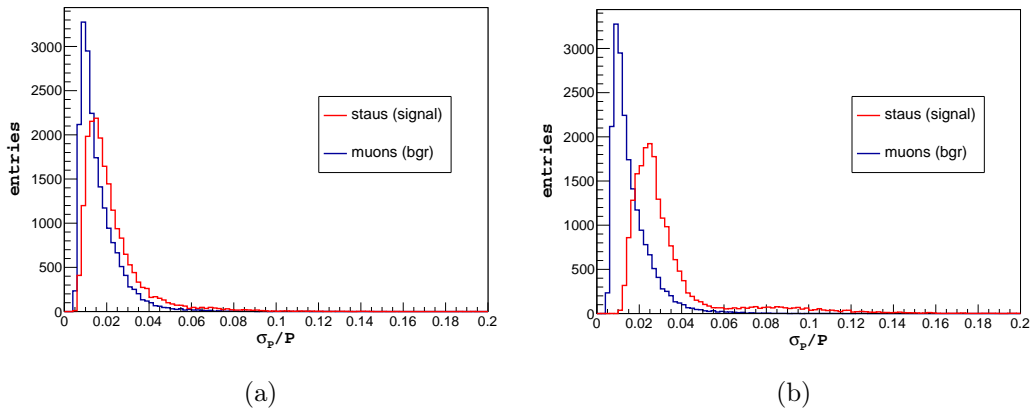


Figure 5.8.: The relative momentum error (σ_P/P) is displayed for staus of $124 \text{ GeV}/c^2$ mass (figure (a)) and for staus of $309 \text{ GeV}/c^2$ mass (figure (b)).

The tracks selected by the above cuts show their momentum and transverse momentum in figures 5.9 and 5.10 for staus of 124 and $309 \text{ GeV}/c^2$ masses, respectively. With a higher mass of stau, these kinetic variables are shifted towards higher values, leading

to a poorer momentum resolution (figure 5.8) and a larger χ^2/dof (figure 5.7) for the corresponding tracks.

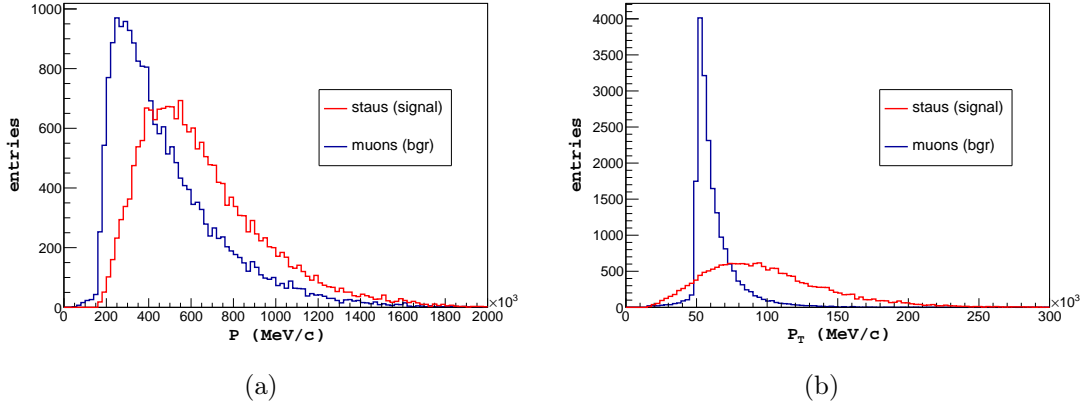


Figure 5.9.: P and P_T are reconstructed for tracks corresponding to staus of $124 \text{ GeV}/c^2$ mass.

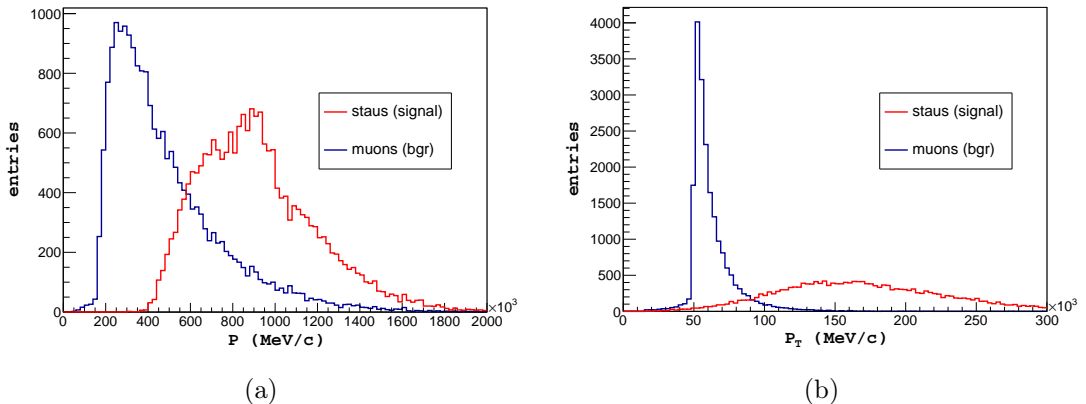


Figure 5.10.: P and P_T are reconstructed for tracks corresponding to staus of $309 \text{ GeV}/c^2$ mass.

5.2.5. Energy deposited in the VELO

The following three sections will describe the deposited signals in the LHCb sub-detectors. We will start with the VELO, then go on with the calorimeters and with the RICH detectors. In this section, we will discuss the deposited energies of staus and muons in the VELO silicon sensors, then consider the ability to identify staus against muons.

When a heavy charged particle travels through matter, it loses a part or all of its energy by ionizing or exciting atoms of the matter. This lost energy rate (dE/dx) is described by Bethe-Bloch formula [41]. Depending on their mass and charge, different particles leave different amounts of energy. This helps us to identify the particles. At very high momentum, a part of the energy lost by muons can come from radiation [41].

As described in section 4.2.1, the VELO is composed of 42 silicon sensors distributed over a length of 1 m along z axis with each sensor having a thickness of 300 μm . A long track originating from the primary vertex will leave its energy in some of the 42 sensors (N in total, $N < 42$). The lost energies in these N sensors follow a Landau distribution [41] with a long tail toward high values. To estimate the most probable value (MPV) of the Landau distribution, we use the truncated mean method: 40% of the highest depositions are discarded, then the average value of the remaining 60% is taken.

The VELO does not deliver directly the deposited energy, it gives Analog-to-Digital Converter (ADC) counts. In the reconstruction program (Brunel), the average value given by the truncated mean method will still be divided by a normalization factor of 47.1 and denoted by *VeloCharge*. This normalization transforms the deposited energy into a value in "MIP" unit, where one MIP corresponds to the energy deposited by a minimum ionizing particle. We will call this *VeloCharge* " ΔE ". An ADC count corresponds to a charge of around 380 electrons collected in the silicon sensors.

Figures 5.11 and 5.12 show the distributions of ΔE simulated by MC11 for muons and staus of 124 and 309 GeV/c^2 masses. The figures (a) shows the ΔE values as a function of the particle momentum and figures (b) show the projections of the 2D histograms (a) on the ΔE axis. Here, the kinetic range is very high ($P > 150 \text{ GeV}/c$), the muons should therefore have some energy loss by radiation. However, this lost energy is not expected to be high in the VELO since the VELO sensors are thin. Moreover, the truncated method rejected the 40% of the highest depositions which probably contain the energy lost by radiation. Hence, the deposited energy distribution of muons cannot go up to high momentum as seen in figures (a). For staus, the shape of the Bethe-Bloch formula can be seen. However, the resolution in ΔE is not sufficient to separate the staus and muons.

In figures (b), we see that the ΔE distributions of muons are higher than the ones of staus. The reason is that from the momentum of 150 GeV/c the muons passed the minimum ionisation point, while the heavier staus are approaching to this point [42].

In brief, the distributions in figures 5.11 and 5.12 show that the ability to identify the staus with VELO alone is very limited at this point. However, using this deposited energy in the VELO together with other sub-detector outputs will improve the situation.

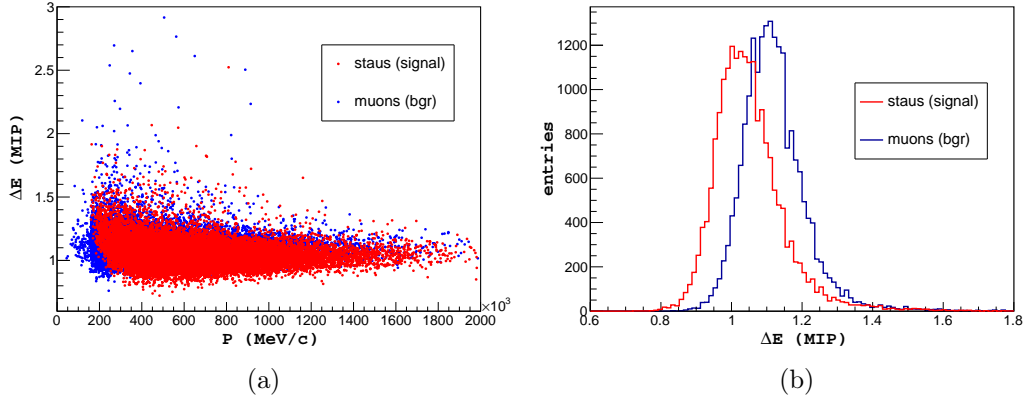


Figure 5.11.: ΔE deposited by the staus of $124 \text{ GeV}/c^2$ mass and the muons is plotted as a function of momentum (a). Projection of histogram (a) on the ΔE axis (b).

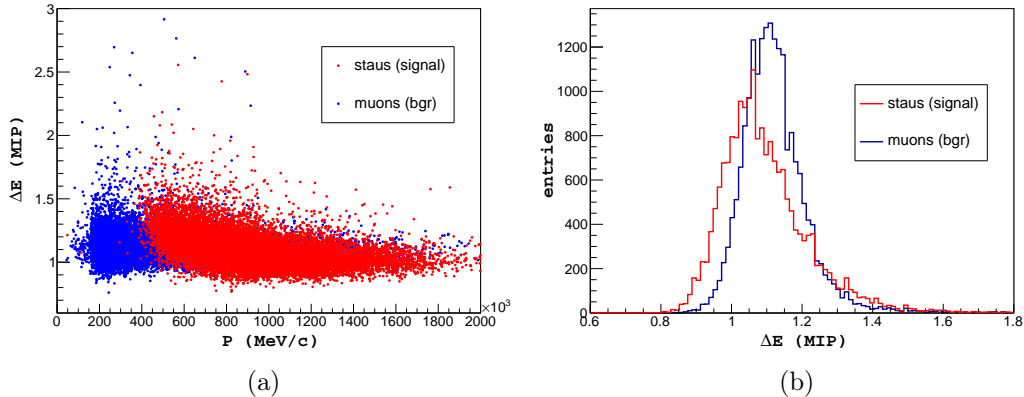


Figure 5.12.: ΔE deposited by the staus of $309 \text{ GeV}/c^2$ mass and the muons is plotted as a function of momentum (a). Projection of histogram (a) on the ΔE axis (b).

Calibration of the deposited energy in the VELO:

We now compare the ΔE deposition in the VELO from the real data and from the simulation: the purpose of this comparison is to "calibrate" the Monte Carlo response, i.e. to obtain a MC response which approaches as much as possible the real data. Two samples of muon tracks from MC and data are used. The tracks are ensured to come from $Z^0, \gamma^* \rightarrow \mu^+ \mu^-$ decays with a mass window $80 < M_{Z^0, \gamma^*} < 100 \text{ GeV}/c^2$ and have the required good quality. Then, they are selected in the kinetic range of our analysis ($P_T > 50 \text{ GeV}/c$). The data and MC samples show a compatibility of the momentum and transverse momentum distributions (figures 5.13 and 5.14).

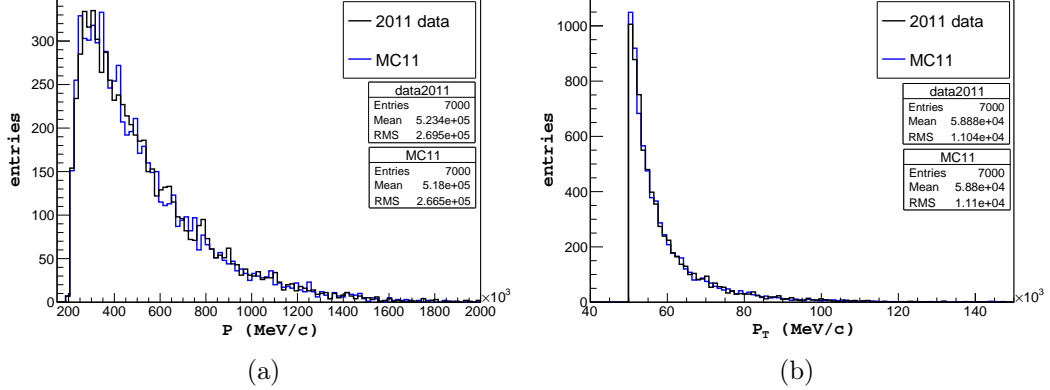


Figure 5.13.: Distributions of the momentum (a) and transverse momentum (b) of muon tracks from MC11 and 2011 data.

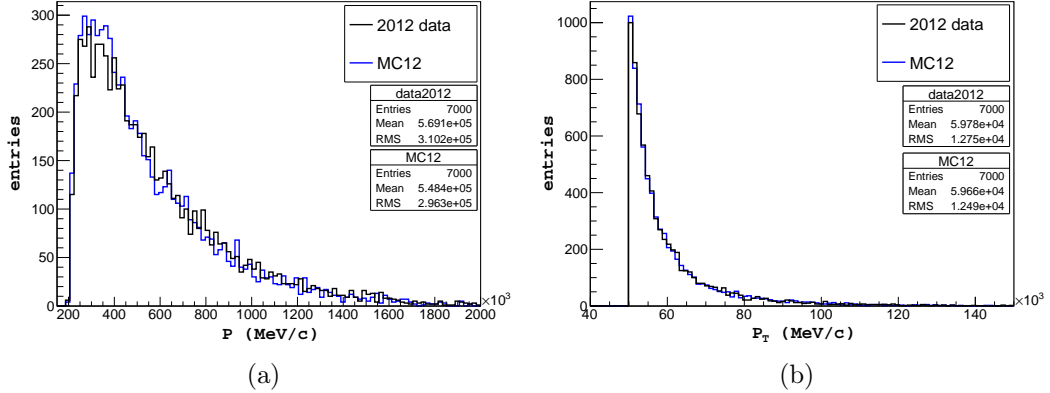


Figure 5.14.: Distributions of the momentum (a) and transverse momentum (b) of muon tracks from MC12 and 2012 data.

- For MC11 and 2011 data: The distributions of ΔE in VELO from MC11 and 2011 data are presented in figure 5.15(a). The shapes of the two distributions are not very different, but the MC values are higher than the data values. To make these two distributions compatible, the MC11 distribution was scaled by a factor of 0.93. The result after the scaling is shown in figure 5.15(b). We see in figure 5.15(b) that the width of the data distribution is still larger than that of the MC distribution. To make the two distributions more compatible, the MC values are re-generated by the convolution of the scaled MC values, i.e. the distribution in figure 5.15(b), and a Gaussian function. The Gaussian function has a mean which is the scaled MC value and a standard deviation which is the square root of the quadratic difference between two widths of the two distributions in figure 5.15(b). The result of the convolution is presented in figure 5.15(c).

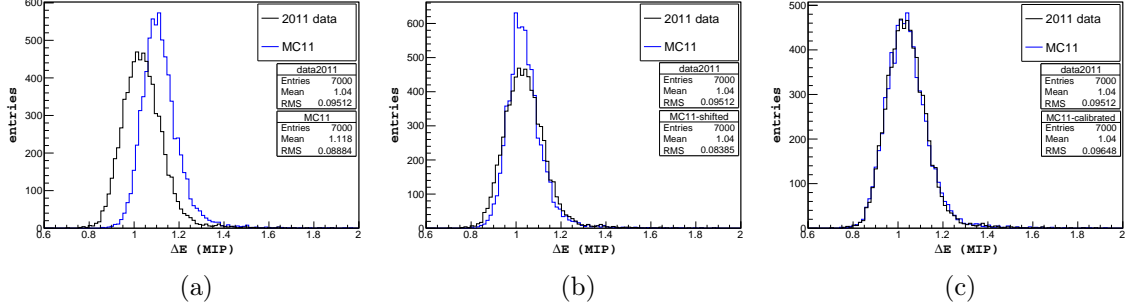


Figure 5.15.: In (a): distributions of ΔE in Velo from MC11 and 2011 data. In (b): the MC distribution was scaled by a factor of 0.93. In (c): the MC distribution was re-generated by a convolution of the scaled MC distribution with a Gaussian.

- For MC12 and 2012 data: Figure 5.16(a) shows two distributions of ΔE for MC12 and 2012 data. The shapes look more compatible than for 2011. However, the MC distribution is now lower than the data's one. The MC distribution was scaled by a factor of 1.058 and the result of this scale is presented in figure 5.16(b). Finally, to make two widths more compatible, a convolution is done as for the 2011 case. The result is shown in the last figure 5.16(c).

These calibrations are applied to the MC muons and the MC staus.

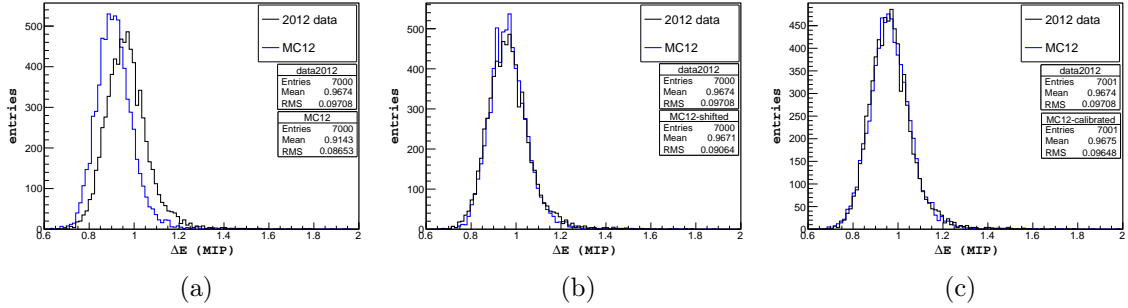


Figure 5.16.: In (a): distributions of ΔE in Velo from MC12 and 2012 data. In (b): the MC distribution was scaled by a factor of 1.058. In (c): the MC distribution was re-generated by a convolution of the scaled MC distribution with a Gaussian.

5.2.6. Deposited energies in the calorimeters

The staus and muons do not leave much of their energies in the calorimeters, contrary to electrons or photons in ECAL, and pions or kaons or protons or neutrons in HCAL. However, in such thick detectors, there is a difference between the amount of energy deposited by the muons and the staus. As mentioned before, staus possess a heavy mass, it is therefore hard for them to radiate. Their deposited energies in the calorimeters result from ionisation and the atom excitation only. For muons, the radiation can occur in these thick detectors. Hence, the total energy depositions of staus in ECAL and HCAL are expected to be lower than that of muons [43].

Figures 5.17 and 5.18 show the distributions of the total deposited energies of staus and muons in ECAL and HCAL, respectively. The left bi-parametric distributions show the deposited energies as a function of the transverse momentum, the right histograms are the projections onto the deposited energy axis. The staus used in these figures have a mass of $124 \text{ GeV}/c^2$. Clearly, the energy deposition distributions of muons are higher than that of staus, as expected. A large fraction of tracks have no deposition in calorimeters (the first bins of figures 5.17(b) and 5.18(b)) because these depositions are lower than the readout thresholds in the calorimeters. In particular, this fraction is higher when the polar angles of tracks become smaller.

These total deposited energies in ECAL and HCAL will be used in the analysis by the Neural Network to classify staus and muons.

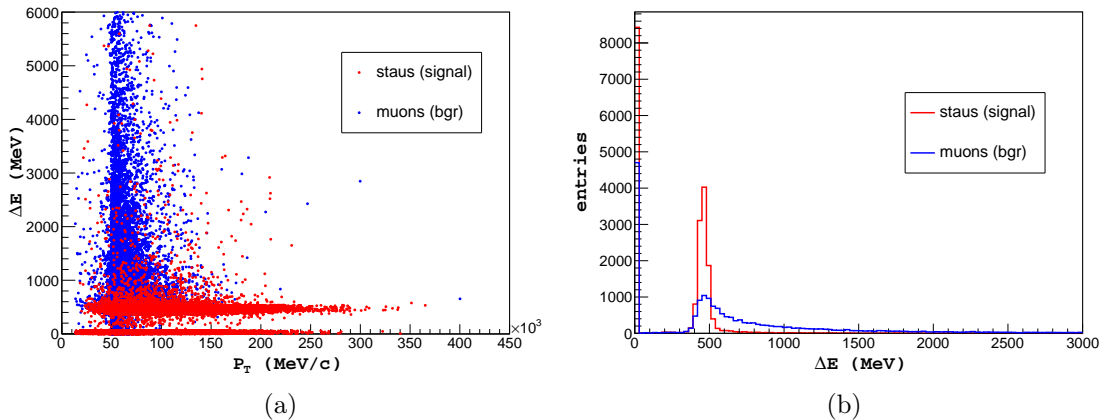


Figure 5.17.: The left figure (a) shows the deposited energies in ECAL as a function of the transverse momentum (P_T), the right histogram (b) is the projection on the deposited energy's axis. The staus used here have a mass of $124 \text{ GeV}/c^2$.

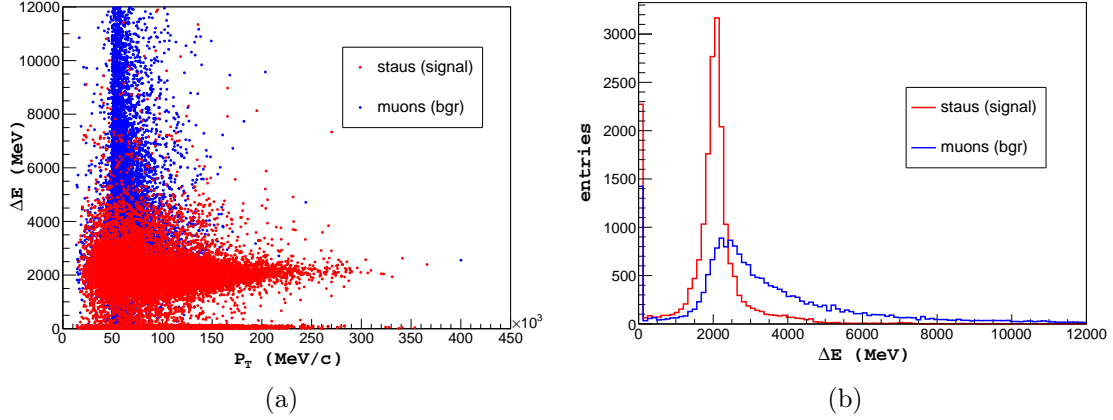


Figure 5.18.: The left figure (a) shows the deposited energies in HCAL as a function of the transverse momentum (p_T), the right histogram (b) is the projection on the deposited energy's axis. The staus used here have a mass of $124 \text{ GeV}/c^2$.

Calibration of the deposited energies in the calorimeters:

Here again, as for the VELO, we "calibrate" the response of the calorimeters in order to have adequate sub-detector responses to train the Neural Network.

We use again the same samples of $Z^0, \gamma^* \rightarrow \mu^+ \mu^-$ from MC and data that we have used for the calibration of the VELO; the muon tracks are selected with the same cuts as for the calibration of the VELO. The distributions of the total deposited energies in ECAL and HCAL by the selected muon tracks are shown in figures 5.19 and 5.21 for MC11 and 2011 data; and the corresponding histograms for MC12 and 2012 data in figures 5.20 and 5.22.

All the left figures show the distributions before calibrations. The MC distributions are always higher than the ones in data. To make them compatible, the MC distributions have to be shifted downwards. The results after shifting are shown in the right figures. The shifting factors are listed in table 5.5. These calibration factors are applied to the MC muons and MC staus.

	ECAL	HCAL
MC11	0.80	0.85
MC12	0.79	0.84

Table 5.5.: The factors have been used to scale the MC distributions of the total deposited energies in the calorimeters.

Although slight differences still exist between the "calibrated" MC distributions and the data, we find that these calibrated responses of the calorimeters are acceptable for the training of the Neural Network.

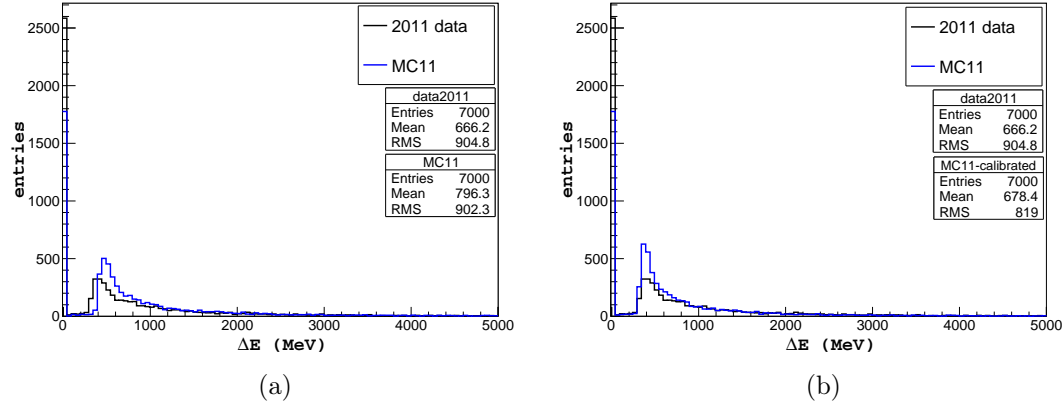


Figure 5.19.: (a): Original distributions of the total deposited energies of muons from MC11 and 2011 data in ECAL. (b): the MC11 distribution was scaled by a factor of 0.80.

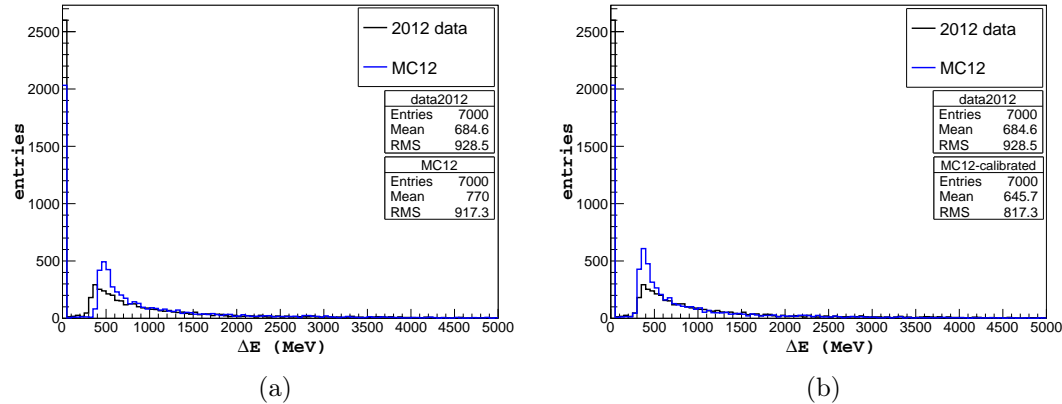


Figure 5.20.: (a): Original distributions of the total deposited energies of muons from MC12 and 2012 data in ECAL. (b): the MC12 distribution was scaled by a factor of 0.79.

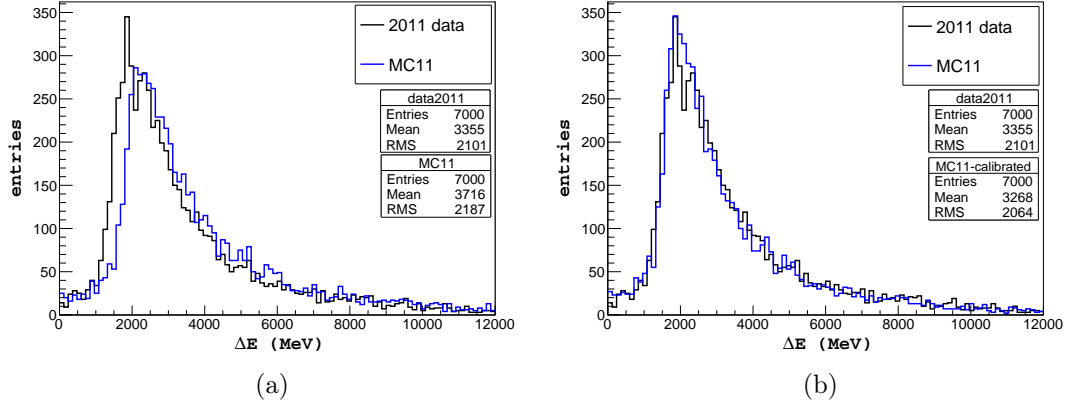


Figure 5.21.: (a): Original distributions of the total deposited energies of muons from MC11 and 2011 data in HCAL. (b): the MC11 distribution was scaled by a factor of 0.85.

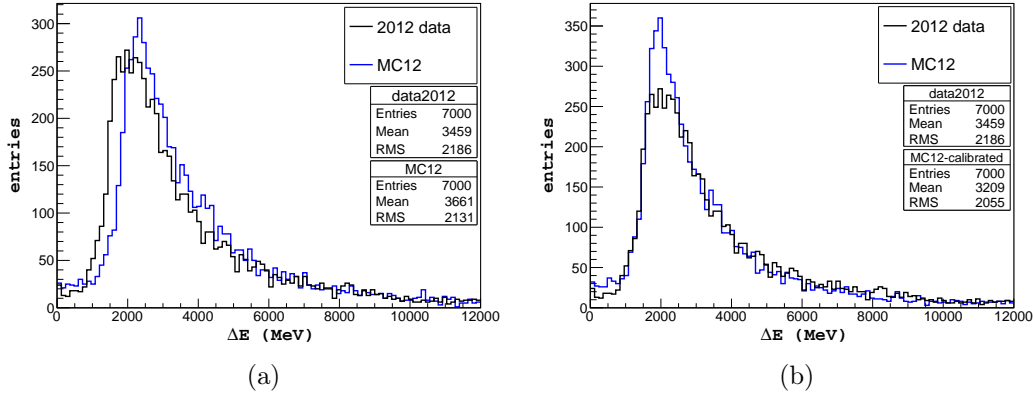


Figure 5.22.: (a): Original distributions of the total deposited energies of muons from MC12 and 2012 data in HCAL. (b): the MC12 distribution was scaled by a factor of 0.84.

Cuts on the deposited energies in calorimeters:

Muons and staus have small energy depositions in the calorimeters; on the contrary, the hadrons deposit a huge amount of energy. Therefore, the ratio between the sum of the total deposited energies of a track in the ECAL and HCAL and its momentum will be small for muons and staus, while this ratio is expected to be large for hadrons, i.e. pions and kaons. Indeed, figure 5.23(a) shows the distributions of this ratio for MC muon and stau tracks. The values are close to zero for staus, and a little bit higher for muons. In contrast, figure 5.23(b) shows that this ratio is large for the muons from the mis-ID

sources. The mis-ID sources are the pions and kaons that have enough energy to escape the calorimeters or decay into a muon in flight, and then are mis-identified as muons by the muon chambers. Figure 5.23(b) uses the mis-ID source generated by a "ParticleGun". The first bin corresponds to tracks which travel in the outer board of the calorimeters and do not give enough signals in the detectors.

The distributions in figure 5.23 show that this ratio $(E_{\text{ECAL}} + E_{\text{HCAL}})/P$ might provide a strong cut to reject the mis-ID background, as well as a part of muon background. We fix this cut to be $(E_{\text{ECAL}} + E_{\text{HCAL}})/P < 0.01$.

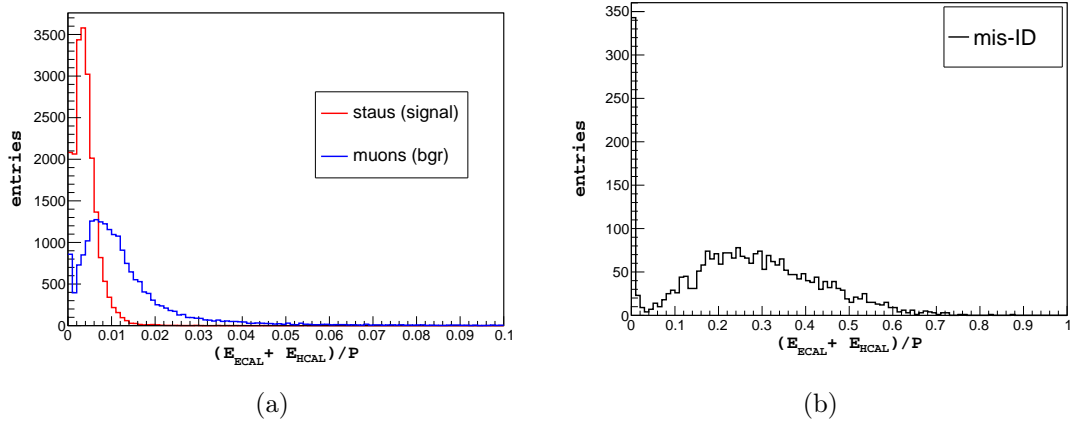


Figure 5.23.: Figure (a): the distributions of the ratio between the sum of the total deposited energies of the muon and stau tracks in the ECAL and HCAL and their momentum; the mass of stau is $124 \text{ GeV}/c^2$. Figure (b): the same variable for muons from the mis-ID source. Note the different scales on the horizontal axes.

5.2.7. Response of the RICHs

In this section, we will look at the response of RICHs to the muons and staus and "calibrate" the response of this detector to muons. Since the staus are very much heavier than muons, the Cherenkov momentum thresholds are very different for these two particles. The thresholds in the three radiators of the LHCb's RICHs for muons and staus are given in table 5.6.

The momentum thresholds in the above table indicate that most of the staus cannot radiate in the two gas radiators; a part of them can do it in the aerogel, but the velocity resolution in aerogel is very limited [44], [24]. The staus are therefore identified as "below-threshold particles" by RICHs.

In contrast, the muons have the ability to radiate in all of the three radiators. However, the RICHs of LHCb have been designed to distinguish between pions and kaons mainly; it is also difficult to distinguish muons from pions because of their close masses. Moreover,

with the momenta above 100 GeV/c, the radiation angles are saturated (see figure 4.14). Consequently, the muons may be mis-identified as one of the other basic particles (e, π, K, p) or a below-threshold particle. Figure 5.24 shows the particle identification (PID) given by RICHs for the true muons and the staus simulated by MC11, where the "PID" corresponding to the identified particles listed in table 5.7.

Radiator	n	β_{thresh}	$P(\mu)$ (GeV/c)	$P(\tilde{\tau})$ (GeV/c)						
				124	154	185	216	247	278	309
Aerogel	1.03	0.97087	0.441	502	623	749	875	1'000	1'126	1'252
C_4F_{10}	1.0014	0.99850	1.93	2'261	2'808	3'373	3'939	4'504	5'069	5'069
CF_4	1.0005	0.99950	3.34	3'919	4'868	5'848	6'827	7'807	8'787	9'767

Table 5.6.: The thresholds of momentum to generate Cherenkov light for muons and staus in the RICH radiators.

RICH PIDs	-1	0	1	2	3	4	5
particles	unknown	e	μ	π	K	p	below threshold

Table 5.7.: The PIDs corresponding to the identified particles by RICHs.

The treatment of the information given by RICH detectors has been developed in section 4.3.1. We have seen that a difference in the log-likelihood value (DLL) is assigned for each track. As this variable is a change in the overall event log-likelihood when the hypotheses of the track is changed, for instance, from pion to electron, or muon, etc... or the below threshold particle hypothesis. The delta log-likelihood for the below threshold particle hypothesis (DLLbt) can be extended down to a value like -150 in figure 5.25. The small peak near zero is attributed to muons being identified as "below threshold" particles. The staus will certainly not leave any Cherenkov signal and correspond to a positive DLLbt. Clearly, this variable gives a powerful mean to separate staus and muons.

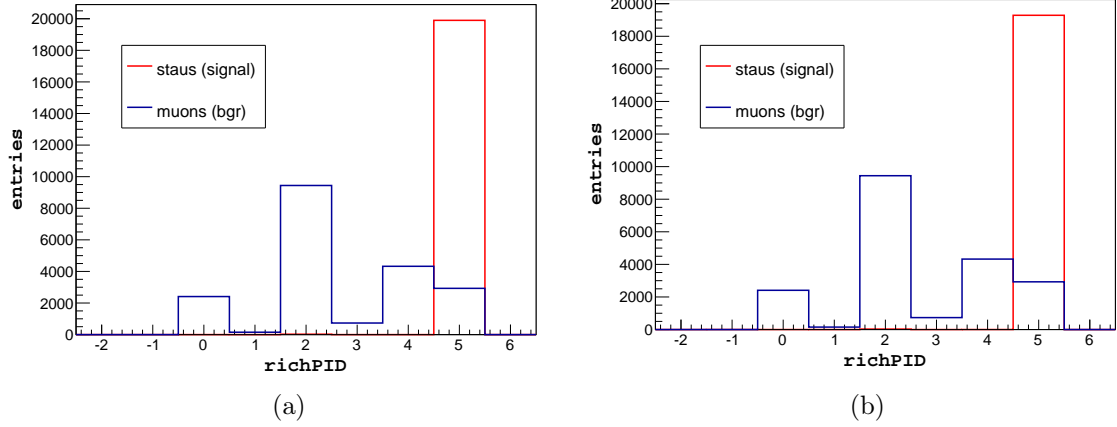


Figure 5.24.: Particle identification (PID) given by RICHs for the muons and staus simulated in MC11. The staus in figure (a) and (b) have the masses of $124 \text{ GeV}/c^2$ and of $309 \text{ GeV}/c^2$, respectively.

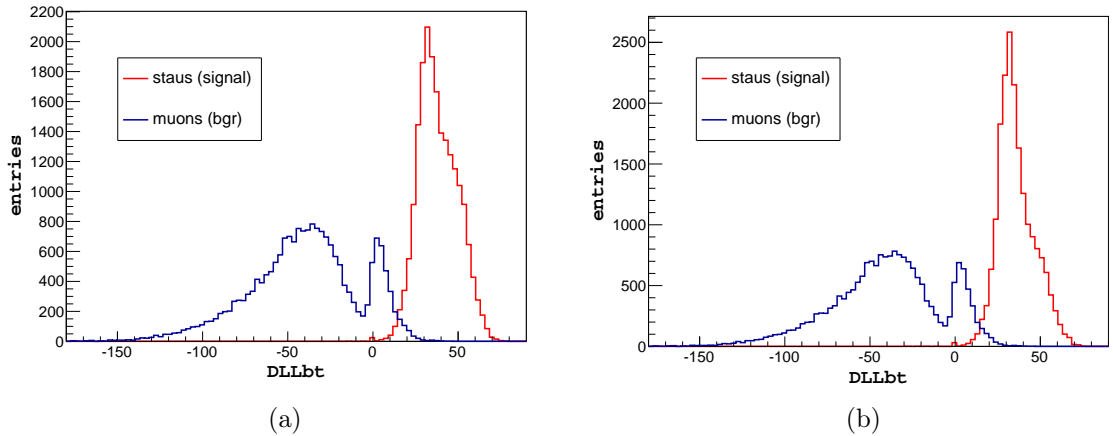


Figure 5.25.: Distribution of the delta log-likelihood for the below threshold particle hypothesis that the RICHs give to the muon and stau tracks simulated by MC11. The two figures (a) and (b) use staus of 124 and $309 \text{ GeV}/c^2$ masses, respectively.

Calibration of the DLLbt variable:

We will use the delta log-likelihood for the below threshold particle hypothesis as an input to the Neural Network, therefore the DLLbt distribution from MC must be compatible with the corresponding distribution from real data. Unfortunately, the distributions of this variable in MC11 and 2011 data are different as shown in figure 5.26(a). In this figure, the good quality muon tracks of $P > 150 \text{ GeV}/c$ and $P_T > 50 \text{ GeV}/c$ and selected from the Z^0 peak ($80 < M_{Z^0} < 100 \text{ GeV}/c^2$) are used. To make the DLLbt distribution

from MC similar to the one from the real data, we proceed as follows: we fill a three dimension histogram (P, η, DLLbt) by using the tracks from data. For a MC muon track, whose momentum (P) and pseudo-rapidity (η) are known, the content of the (P, η) cell in the 3D histogram is projected onto the DLLbt variable and the new value of DLLbt for the MC track is chosen randomly from this projected distribution. In the case where the content of the (P, η) cell is zero because of the poor statistics, the original DLLbt value of the MC track is kept. The result of this calibration for MC11 muons is shown in figure 5.26(b). We can see now a good agreement between the two distributions from MC11 and 2011 data. The calibration will be applied for the MC muons used in the neural network. For MC staus, we have to rely on the original MC response since there is no real data to calibrate this variable for staus.

This calibration method is also applied to the MC12 muons.

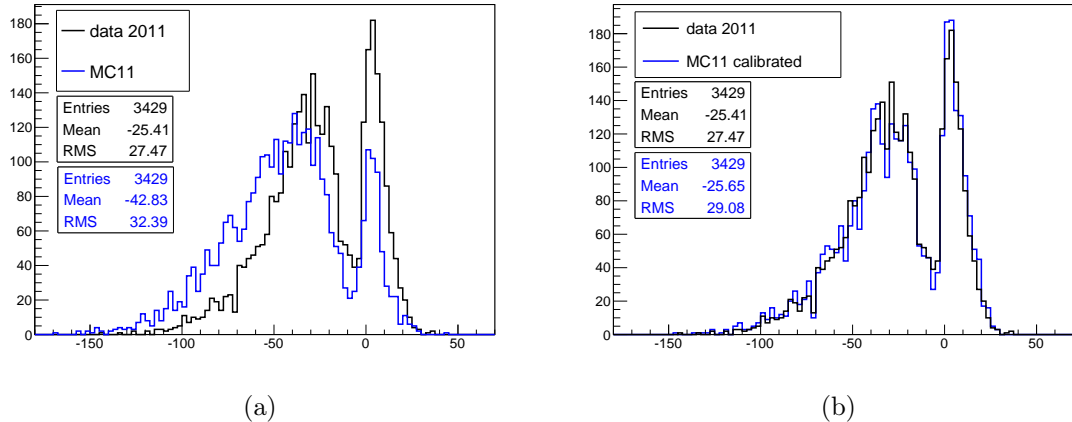


Figure 5.26.: In (a): the original distributions of the delta log-likelihood for the below-threshold particle hypothesis from muon tracks in MC11 and 2011 data. In (b): the MC11 distribution was generated again to make it similar to the one in data.

5.2.8. Impact parameter

The staus that we study and muons from Z^0, γ^* decays are produced at the primary vertex, they should therefore have a smaller impact parameter (IP) than the muons from the decays of heavy quarks, or from the misidentified sources or from the decay $Z^0, \gamma^* -> \tau^+ \tau^-$. We have selected tracks having P_T larger than 50 GeV/c from five samples and compared their IP values. These sources are:

- staus
- muons from Z^0, γ^*
- muons from $Z^0, \gamma^* -> \tau^+ \tau^-$, where the taus decay into muons.

- muons from top quark decays via the W^\pm bosons.
- mis-identified muons

The first four sources come from MC and the last one is from the data.

Figure 5.27(a) shows the impact parameter of the stau tracks and the muon tracks from Z^0, γ^* decays with respect to the best primary vertex reconstructed in the event, figure 5.27(b) shows the IP distributions from the three other background sources: decays of the top quarks, misidentified hadrons and decays $Z^0, \gamma^* \rightarrow \tau^+ \tau^-$. While the impact parameter values of stau and muon pairs (figure 5.27(a)) are close to zero, the ones for the other backgrounds (figure 5.27(b)) extend to larger values. An impact parameter less than 50 μm has been required to select the stau tracks.

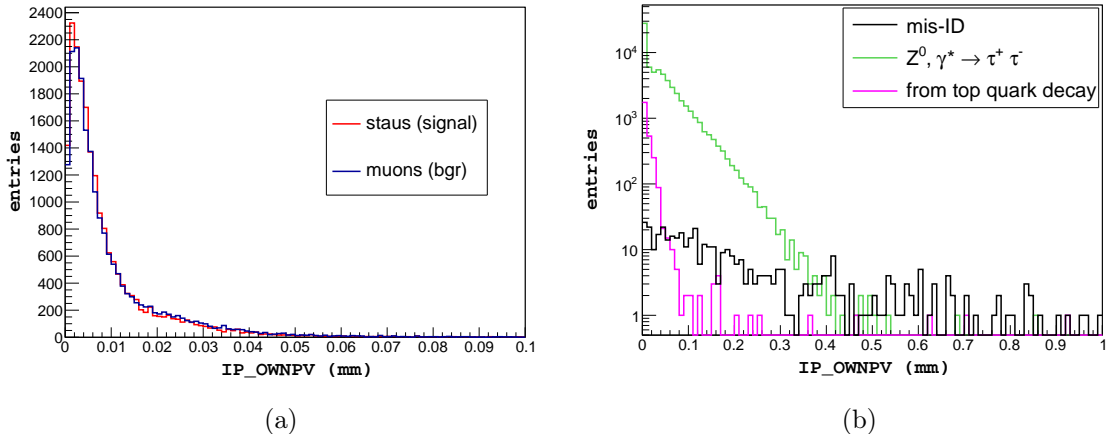


Figure 5.27.: Impact parameter of stau tracks ($m_{\tilde{\tau}} = 124 \text{ GeV}/c^2$) and muon tracks from Z^0, γ^* decays with respect to the best primary vertex in figure (a). The distributions for other backgrounds in figure (b).

5.2.9. Asymmetry in transverse momentum

The two staus in a pair are expected to have nearly equal transverse momenta. To express this property, the asymmetry of the transverse momenta of the two particles in the pair is defined:

$$P_T^{asym} = \frac{|P_T^+ - P_T^-|}{P_T^+ + P_T^-} \quad (5.1)$$

where P_T^+, P_T^- are the transverse momenta of the particles in a pair. This asymmetry for stau and muon pairs are shown in figure 5.28. In these figures, the pairs are selected by the $Z02MuMu$ stripping line and have an invariant mass $M_{pair} > 100 \text{ GeV}/c^2$, the

tracks are insured to be of good quality and have $P_T > 50$ GeV/c. The distributions show that a cut $P_T^{asym} < 0.4$ can be applied for the stau selection.

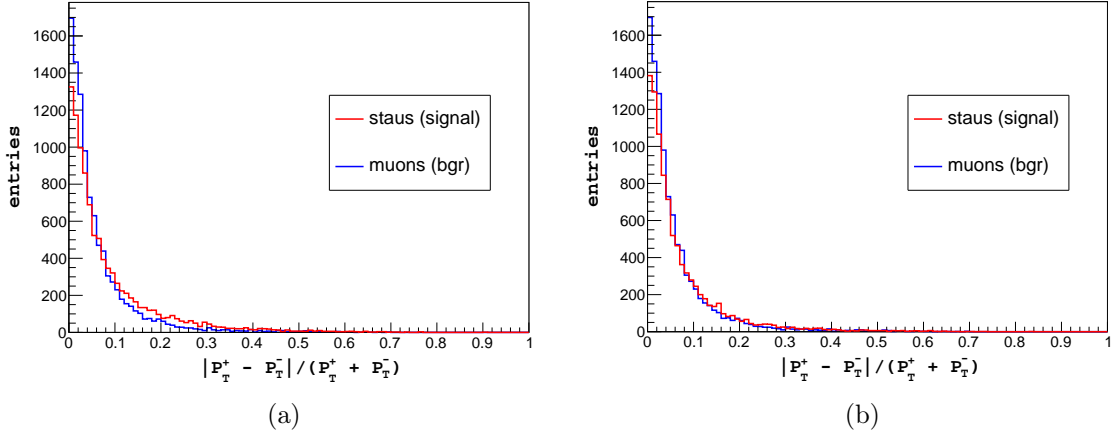


Figure 5.28.: The asymmetry in transverse momentum of the two particles in the stau and muon pairs. The staus used in figures (a) and (b) have the masses of 124 and 309 GeV/c² respectively.

5.2.10. Pair isolation

While the stau tracks and the muon tracks from Z^0, γ^* decays are quite isolated, the muons from the mis-ID source or from heavy quark decays are surrounded by other charged particles. In general, the particles which accompany the muons and staus have a small P_T . Therefore to quantify an isolation, we consider the asymmetry between the transverse momentum (P_T) of the considered track and the scalar sum (ΣP_T) of the transverse momenta of all charged particles in a cone surrounding this considered track. The transverse momentum of the considered track is excluded from this sum.

$$I_{track} = \frac{P_T - \Sigma P_T}{P_T + \Sigma P_T} \quad (5.2)$$

The cone is defined by:

$$R = \sqrt{(\eta_{track} - \eta_{particle})^2 + (\phi_{track} - \phi_{particle})^2} < 0.5 \quad (5.3)$$

where $(\eta_{track}, \phi_{track})$ are the coordinates of the considered track in spherical coordinates, $(\eta_{particle}, \phi_{particle})$ are the coordinates of any other charged particle. Then, the isolation

of a pair can be defined according to [45]:

$$I = \sqrt{\frac{(I_{track1} - 1)^2 + (I_{track2} - 1)^2}{8}} \quad (5.4)$$

The factor of 8 in the denominator is to normalise the value of I from 0 to 1.

Figure 5.29(a) shows the pair isolation distribution of the muon pairs from Z^0, γ^* decays and of the stau pairs with a mass of 124 GeV/c². These distributions tend to zero and this shows that the stau pairs and the muon pairs from Z^0, γ^* decays are quite isolated. Figure 5.29(b) shows the asymmetry I for the muon pairs from the decays $Z^0, \gamma^* \rightarrow \tau^+ \tau^-$ and from the top quark pairs. The muon pairs from these backgrounds are also quite isolated as we have required the muons to have a high P_T , greater than 50 GeV/c. This would not be the case if this condition on P_T had not been fulfilled. We will ask $I < 0.1$ to select the stau pairs. However we do not expect that a cut on this variable strongly rejects the backgrounds.

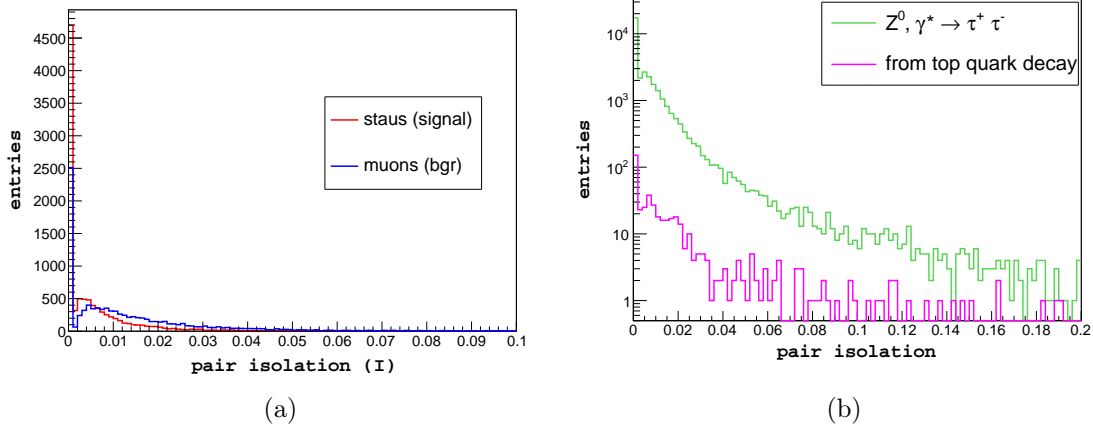


Figure 5.29.: The pair isolation of the stau pairs ($m_{\tilde{\tau}} = 124$ GeV) and the muon pairs from Z^0, γ^* decays in figure (a). The distributions of the same variable for the other backgrounds.

5.3. Selection and efficiencies

In the previous sections, we have considered the variables describing the stau pairs and their muon background. We will now summarize the cuts on these variables. They are:

1. The track is a long track.
2. The track is identified as muon track by the muon chambers with the variable $IsMuon = 1$.
3. The track has a chi-square per degree of freedom $\chi^2/dof < 3$.

4. The relative momentum resolution of the track satisfies $\sigma_P/P < 0.1$.
5. At least one muon of the pair has to fire the trigger on single muon of high P_T (L0, HLT1, HLT2).
6. The pseudo-rapidity of each track in the pair is in the range $2.07 < \eta < 4.38$.
7. The cuts on the momentum of the track vary with the masses of staus and are listed in table 5.8.

$m_{\tilde{\tau}}$ (GeV/c ²)	124	154	185	216	247	278	309
P (GeV/c) at 7 TeV	150	200	200	250	300	300	400
P (GeV/c) at 8 TeV	150	200	200	250	300	350	400

Table 5.8.: Cuts on the momentum of the track to select the staus.

8. The transverse momentum of the track satisfies $P_T > 50$ GeV/c.
9. The sum of the energy depositions in HCAL and ECAL divided by the track momentum $(E_{\text{ECAL}} + E_{\text{HCAL}})/P < 0.01$.
10. The impact parameter of the track with respect to the best primary vertex in the event must be $IP < 50 \mu m$.
11. The asymmetry of the P_T of the two tracks in a pair is $P_T^{\text{asym}} < 0.4$.
12. The variable "pair isolation" is $I < 0.1$.
13. The invariant mass of the pair must be $M_{\text{pair}} > 100$ GeV/c².

By applying the above cuts, we obtain the selection efficiencies for muon and stau pairs listed in tables 5.9 and 5.10. The selection efficiency is defined as the ratio between the number of pairs passing the selection cuts and the number of pairs generated in the LHCb acceptance.

Now we can estimate the expected number of pairs that we can select from the data with the formula:

$$n = L \times \epsilon \times A \times \sigma \quad (5.5)$$

where n is the expected number of the pairs, L is the integrated luminosity, ϵ is the selection efficiency, A is the acceptance factor and σ is the cross section for the pair production.

The LHCb experiment has collected data corresponding to integrated luminosities of 1.01 fb^{-1} and 2.1 fb^{-1} in 2011 and 2012, respectively. Using the equation 5.5 and the values of the cross sections (tables 5.2, 5.4), the acceptance factor (table 5.3) and the selection efficiencies (tables 5.9, 5.10), we compute the expected number of stau and muon pairs for these luminosities. The results are presented in table 5.11.

$m_{\tilde{\tau}}$ (GeV/c ²)	124	154	185	216	247	278	309
Efficiency (ϵ) (%) for stau	37.63	36.29	33.48	30.04	26.51	23.06	19.84
Efficiency (ϵ) (%) for muon	23.11	23.08	23.08	21.85	19.20	19.20	12.73

Table 5.9.: Selection efficiencies for muon and stau pairs using the selection cuts. These values are for MC11.

$m_{\tilde{\tau}}$ (GeV/c ²)	124	154	185	216	247	278	309
Efficiency (ϵ) (%) for stau	37.21	35.76	31.12	30.01	26.84	23.65	20.57
Efficiency (ϵ) (%) for muon	24.26	24.24	24.24	23.21	20.83	17.80	14.72

Table 5.10.: Selection efficiencies for muon and stau pairs using the selection cuts. These values are for MC12.

$m_{\tilde{\tau}}$ (GeV/c ²)	$L = 1.01 \text{ fb}^{-1}$ at 7 TeV		$L = 2.1 \text{ fb}^{-1}$ at 8 TeV	
	muon pairs	staus pairs	muon pairs	staus pairs
124	248.8	0.572	632.3	1.670
154	248.4	0.181	631.8	0.559
185	248.4	0.064	631.8	0.191
216	235.2	0.024	605.0	0.081
247	206.7	0.010	542.9	0.038
278	206.7	0.004	464.0	0.015
309	137.0	0.002	383.7	0.007

Table 5.11.: Expected number of selected stau and muon pairs.

5.4. Other backgrounds

The other background sources which may occur in our search are:

- Decays $Z^0, \gamma^* \rightarrow \tau\tau$ where both taus decay leptonically to muons and neutrinos. This decay is estimated by MC to contribute 0.017 events to the number of events selected in 1 fb^{-1} at 7 TeV collisions.
- Decays of the top quark pairs into b quarks and W bosons. These decays can contribute to the background when both W bosons decay to muons and neutrinos. This background may contribute 0.13 events to the number of events selected in 1 fb^{-1} at 7 TeV collisions. This estimation is done by MC.
- Pions and kaons may be mis-identified as muons if they decay in flight or they have enough energy to escape the calorimeters and are identified as muons by the muon chambers. To estimate this background, the minimum bias 2011 data were used. The good quality tracks with $IsMuon = 1$ and $P_T > 50 \text{ GeV}/c$ were selected.

The minimum bias (MB) events are mostly dominated by hadrons and the muons constitute an extremely small fraction, therefore we consider the fraction of all long tracks that are identified as muons in these MB events as an upper limit on the probability of hadron mis-identification. And we see that this upper limit on the probability for one track (pion or kaon) of $P_T > 50 \text{ GeV}/c$ to be mis-identified as muons is about 7.8×10^{-5} . In the minimum bias 2011 data, we found no events with two good quality tracks identified as muons with opposite charges.

In conclusion, the contribution of these backgrounds in our analysis are very tiny with respect to the contribution from $Z^0, \gamma^* \rightarrow \mu^+\mu^-$. Therefore, the above backgrounds are neglected and we conclude that the main source background to the stau search is $Z^0, \gamma^* \rightarrow \mu^+\mu^-$.

Chapter 6.

Analysis of the Monte Carlo data by Neural Network

In the previous chapter, we have defined the cuts to select the stau pairs. Definitely the muon pairs of high energies will also pass these cuts. We have also considered the signals deposited by staus and muons in the sub-detectors (VELO, ECAL, HCAL and RICHs) and calibrated these signals to get their responses from MC similar to the ones from the data. In this chapter, we will use these signals to separate the selected stau tracks from the muon tracks with a Neural Network (NN) [46]. This will be presented in section 6.1. In section 6.2, we will present two ways to define a region for the stau signal and estimate the expected numbers of stau pairs and muon pairs in this region.

The analysis presented in this chapter will use the Monte Carlo simulated data. The result from the real data will be shown in chapter 7.

6.1. Analysis of individual tracks

We will use a Neural Network to distinguish the stau tracks from muons tracks. The Neural Network is one of the methods based on machine learning techniques which are used to analyse the data. Here, the variables from MC events will be used to train and test the NN. Then, the trained NN will be used to classify the data. To analyse the tracks, we use four variables as inputs of the NN. These are:

- the average energy deposition in a VEL0 sensor
- the total energy deposition in the ECAL
- the total energy deposition in the HCAL
- the delta log-likelihood value for below-threshold particle hypothesis (DLLbt) given by the RICHs

The distributions of the four variables are shown in figure 6.1. In this figure, we use the muon and stau tracks simulated by MC11 and the staus have a mass of $124 \text{ GeV}/c^2$.

All muon and stau tracks are selected by the selection cuts corresponding to the case of 124 GeV/c^2 stau mass. These variables were calibrated.

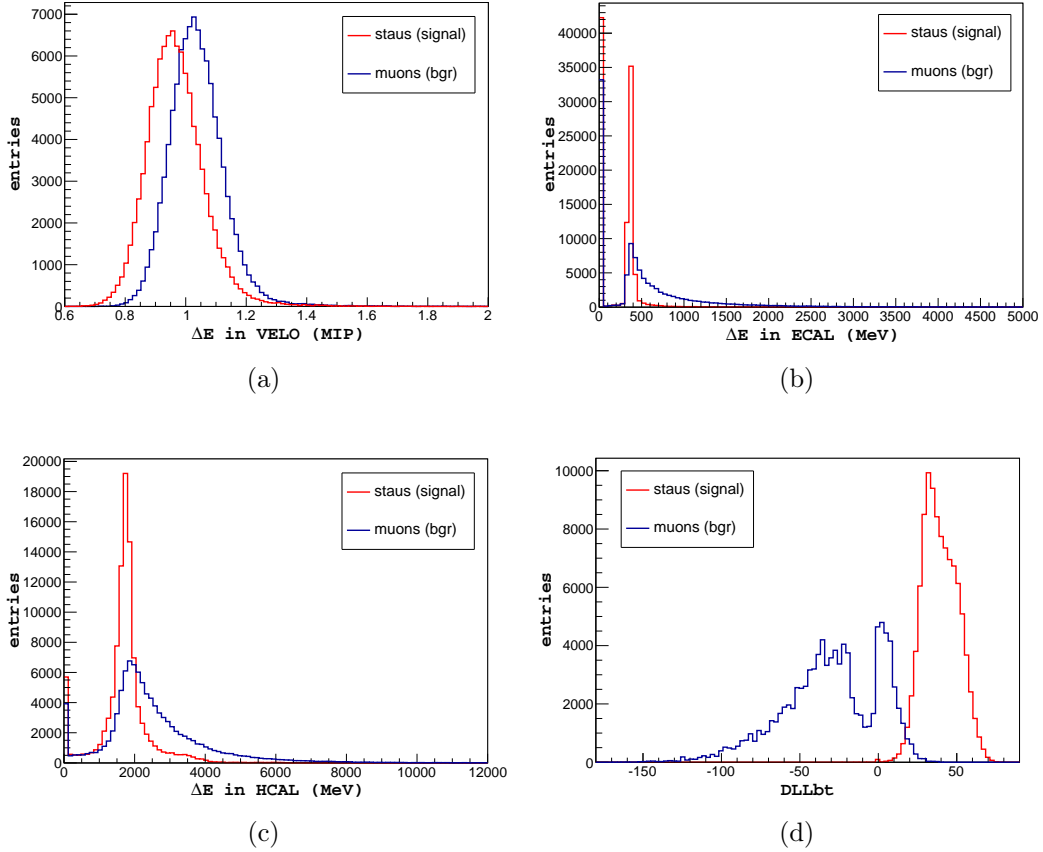


Figure 6.1.: The four variables of the stau and muon tracks used as inputs of the NN.

The training and testing samples have the same number of events. The stau is the signal source and the muon is the background source.

In the output, the NN gives to each track an NN response. In our analysis, we use the NN twice to distinguish the individual tracks and the pairs. To avoid confusion, the NN which distinguishes the individual tracks will be called the first NN and its output will be denoted by NN1. The NN which distinguishes the pairs will be called the second NN and its output will be denoted by NN2. Figures 6.2(a) and 6.2(b) present the NN1 responses for the muon tracks and the stau tracks of 124 and 309 GeV/c^2 masses, respectively. We see that the NN1 responses are mainly peaked at 1 for signals and at 0 for backgrounds. This NN1 response for the individual tracks will be used in the next analysis step, that is the analysis of the pairs.

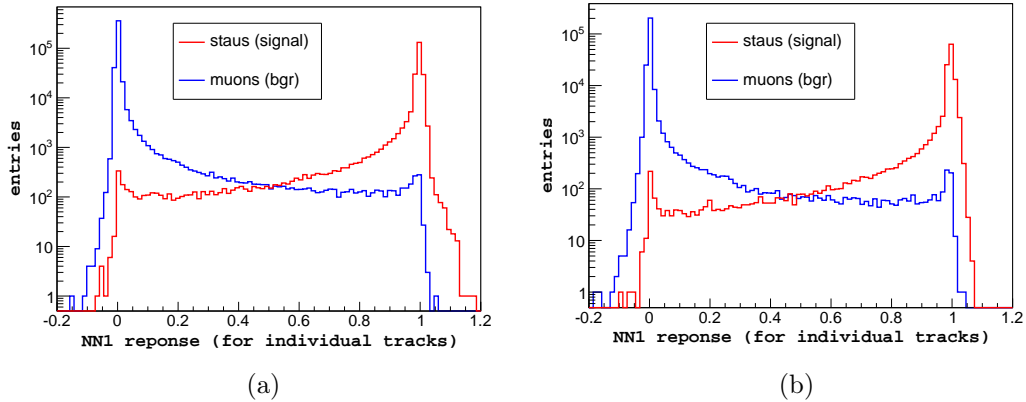


Figure 6.2.: NN1 responses for MC muon tracks and MC stau tracks. Figure (a) shows the NN1 response for the staus of $124 \text{ GeV}/c^2$ mass and figure (b) is for the staus of $309 \text{ GeV}/c^2$ mass. The vertical scale is logarithmic.

6.2. Selection of the stau pairs

6.2.1. Selection based on the pair significance

Using the results of the classification for the individual tracks in the previous section, we compute the product of the two NN1 responses for the two tracks in a pair. This product can be considered as a "significance for each pair", and we called it *pair significance*. This *pair significance* is presented in figures 6.3(a) and 6.3(b) for the muon pairs and the stau pairs corresponding to the 124 and $309 \text{ GeV}/c^2$ masses, respectively. We can see that this *pair significance* gives quite separated results for the muon and stau pairs reflecting a kind of pattern rather than just random distribution and allowing us to characterize this product as a "significance".

We will apply a cut on the pair significance to separate the stau pairs and muon pairs. The region higher than the cut will be called *stau region*. And the cut is chosen so that 95% of the stau pairs are kept in the stau region. Table 6.1 gives the cuts corresponding to the different masses of staus. The fractions (R) of the muon pairs staying in the stau region are shown in table 6.2.

$m_{\tilde{\tau}}$ (GeV/c^2)	124	154	185	216	247	278	309
MC11	0.57602	0.55754	0.53046	0.54970	0.55054	0.49818	0.65834
MC12	0.73058	0.71966	0.70454	0.69950	0.69026	0.73058	0.77510

Table 6.1.: Cuts on the pair significance to separate the stau pairs and the muon pairs.

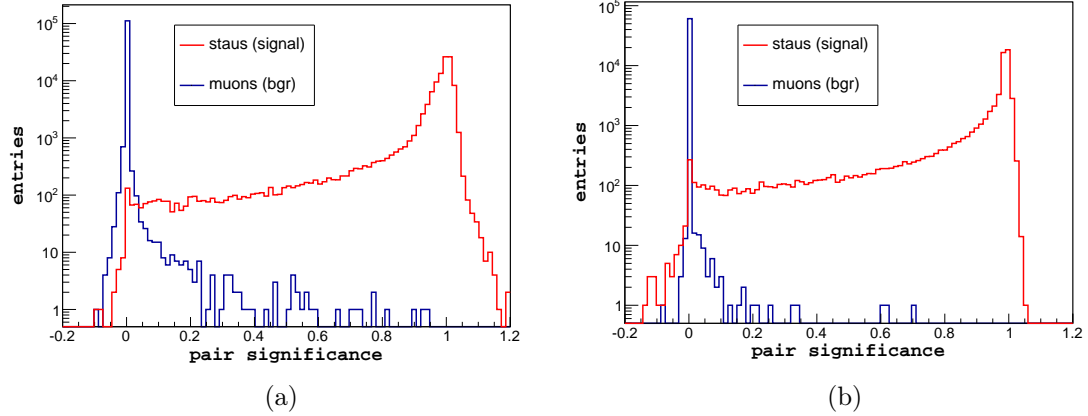


Figure 6.3.: The *pair significance* of the muon pairs and the stau pairs with the masses of 124 GeV/c^2 (a) and 309 GeV/c^2 (b).

$m_{\tilde{\tau}}$ (GeV/c^2)	124	154	185	216	247	278	309
MC11 ($\times 10^{-5}$)	5.6	7.1	7.5	4.2	9.0	9.5	2.4
MC12 ($\times 10^{-5}$)	1.7	1.7	1.7	2.5	0.8	1.4	0.6

Table 6.2.: Fraction (R) of the muon pairs staying in the stau region.

Finally, the expected numbers of the stau pairs and of the muon pairs falling into the stau region are computed by the formula:

$$n_{\text{exp}} = n \times R \quad (6.1)$$

where n_{exp} is the expected number of pairs in the stau region, n is the expected number of pairs passing the selection cuts and computed with equation 5.5, R is the fraction of surviving muon pairs in the stau region given in table 6.2 and R is equal 95% for the stau pairs. The expected numbers are presented in table 6.3.

$m_{\tilde{\tau}}$ (GeV/c ²)	$L = 1.01 \text{ fb}^{-1}$		$L = 2.1 \text{ fb}^{-1}$	
	stau pairs	muon pairs	stau pairs	muon pairs
124	0.543	0.014	1.587	0.011
154	0.172	0.018	0.531	0.011
185	0.061	0.019	0.181	0.011
216	0.023	0.010	0.077	0.015
247	0.010	0.019	0.036	0.004
278	0.004	0.020	0.014	0.007
309	0.002	0.003	0.007	0.002

Table 6.3.: Expected numbers of the stau pairs and the muon pairs in the stau region for the luminosities of 1.01 and 2.1 fb^{-1} .

6.2.2. Selection based on the pair significance and invariant mass of the pairs

In this section, we present another selection for the stau pairs based on the pair significance and incorporating the invariant mass of the pairs.

The invariant mass for the muon pairs and the stau pairs is shown in figure 6.4. Although we calculate the invariant mass of the stau pairs by assuming the mass of each stau to be that of a muon, we still see a difference between the invariant mass distributions of the stau pairs and the muon pairs. The true masses of the staus in figures 6.4(a) and 6.4(b) are 124 and 309 GeV/c^2 , respectively. We see that higher is the true mass of the staus, more does the invariant mass distribution extend towards high values. This gives a hint to distinguish the stau pairs from the muon pairs more efficiently.

We now use the pair significance that we consider in section 6.2.1 and the invariant mass as two inputs for a new classifying NN analysis (the NN2). The output of the second NN is shown in figure 6.5. The original masses of the staus used in this figure are 124 GeV/c^2 (a) and 309 GeV/c^2 (b). We can observe that the NN2 responses are largely grouped toward the value 1 for the stau pairs, whereas the muon pair responses are grouped around the value 0.

This second NN analysis is only aimed to provide a cut on NN2 to separate stau and muon pairs. To set this cut, we will estimate the significance $(S/\sqrt{S+B})$ versus the NN2 response, where S and B are the integrals of the signal (stau) and the background (muon) from the NN2 value to the right edge in the histograms of figure 6.5. The significances corresponding to the two histograms in figure 6.5 are drawn in figure 6.6. The cuts then are defined basing on these significances. In general, the cut will be chosen at the NN2 value where the significance gets to a maximum. In our case, the significance lines exhibit plateaux, instead of peaks. Instead of choosing the cut at the center of the plateau, we

chose a NN2 response of 0.8 to reduce more background. The cuts are pointed out by the magenta arrows in figure 6.6 and by the green lines in figure 6.5. This cut is applied to analysis for all the stau masses ($124 \div 309 \text{ GeV}/c^2$).

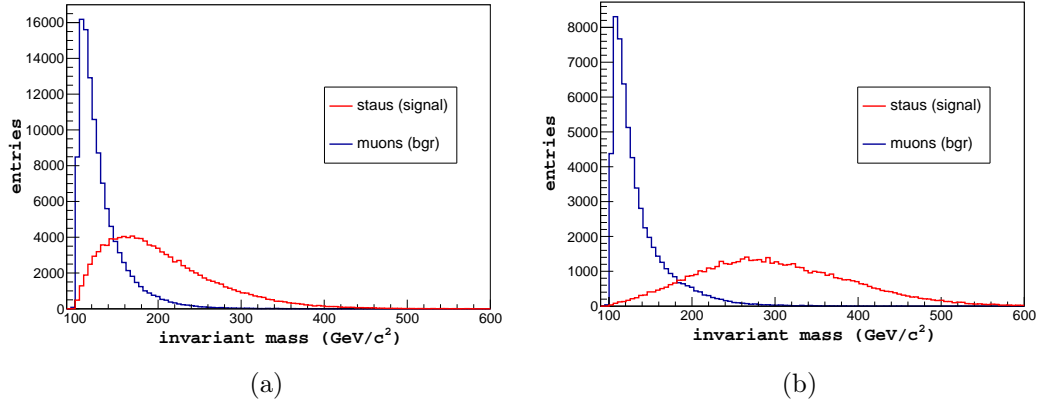


Figure 6.4.: Invariant mass of the muon pairs and the stau pairs with the original masses of $124 \text{ GeV}/c^2$ (a) and $309 \text{ GeV}/c^2$ (b).

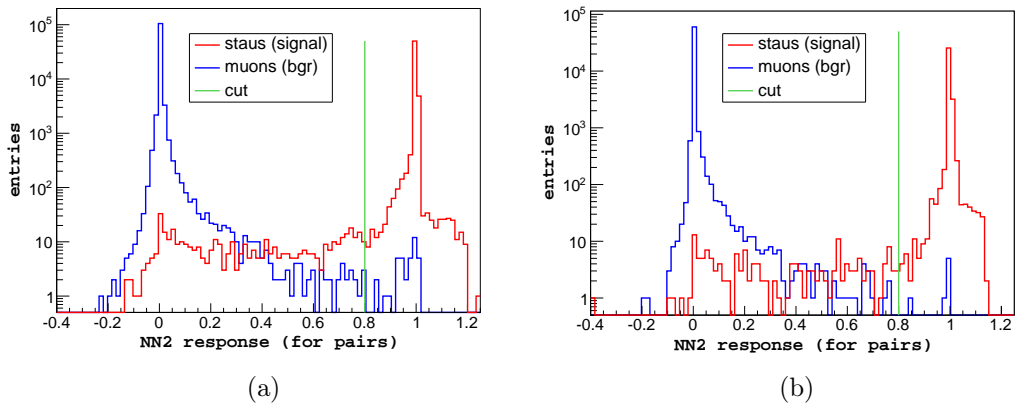


Figure 6.5.: NN2 responses for stau and muon pairs. The original masses of the staus in (a) and (b) are $124 \text{ GeV}/c^2$ (a) and $309 \text{ GeV}/c^2$, respectively.

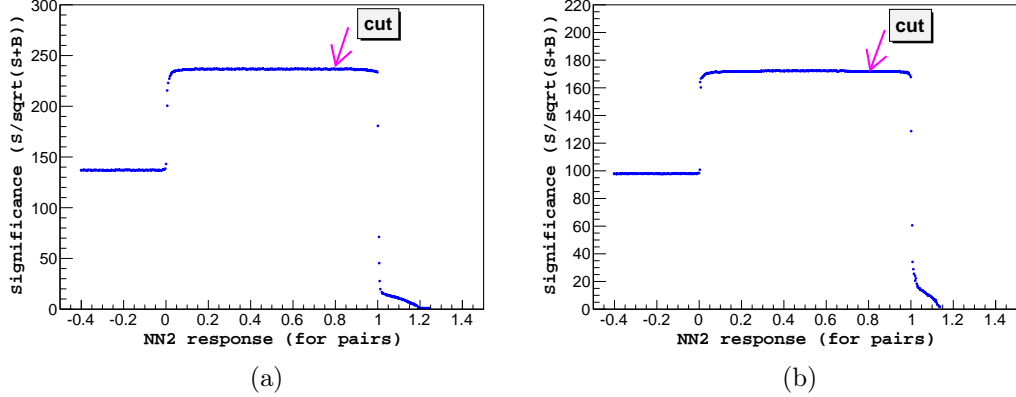


Figure 6.6.: Significance $S/\sqrt{S+B}$ versus the NN2 response. Figures (a) and (b) correspond to the histograms 6.5(a) and 6.5(b), respectively.

We now draw the bi-parametric histogram of the pair significance and the invariant mass in figure 6.7. The stau pairs and the muon pairs are displayed by red and blue, respectively. The cut of 0.8 on NN2 is now corresponding to the green line. In this method, we also call the region above the green line *stau region*.

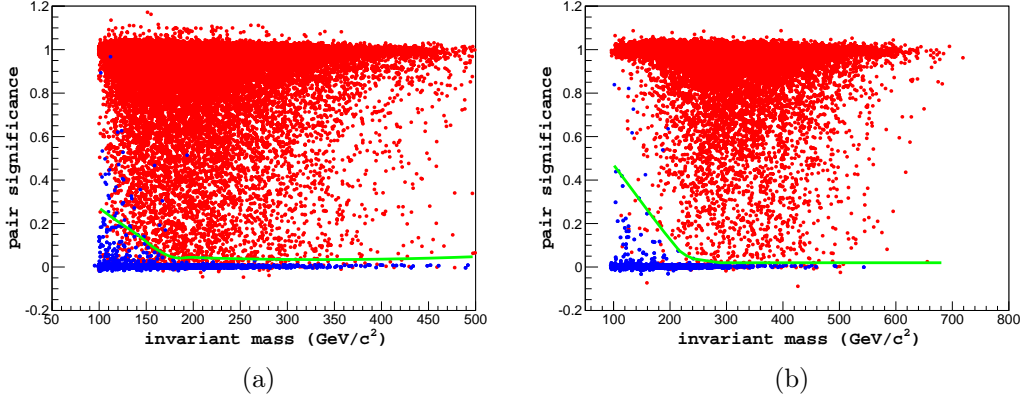


Figure 6.7.: The green boundary separates the stau and the muon regions in the bi-parametric histogram of the pair significance and the invariant mass. Figures (a) and (b) correspond to the staus of 124 and 309 GeV/c^2 masses, respectively.

After having defined the stau region boundary, we can compute the fraction (R) of surviving stau and muon pairs remaining in the stau region. Table 6.4 lists these fractions for muon and stau pairs estimated by MC11 and MC12. For the stau pairs, this fraction is very high, while it is very tiny for the muon pairs. This is a convenience for our search.

$m_{\tilde{\tau}}$ (GeV/c ²)	MC11		MC12	
	stau pairs (%)	muon pairs (%)	stau pairs (%)	muon pairs (%)
124	99.21	0.035	99.359	0.025
154	99.10	0.034	99.365	0.023
185	99.20	0.029	99.406	0.020
216	99.15	0.020	99.378	0.021
247	99.16	0.013	99.405	0.022
278	99.17	0.018	99.445	0.013
309	99.43	0.011	99.506	0.019

Table 6.4.: Fraction (R) of surviving stau and muon pairs in the stau region.

For the integrated luminosities of 1.01 fb^{-1} and 2.1 fb^{-1} , the number of the stau pairs and of the muon pairs expected to be observed in the stau region are presented in table 6.5.

$m_{\tilde{\tau}}$ (GeV/c ²)	$L = 1.01 \text{ fb}^{-1}$		$L = 2.1 \text{ fb}^{-1}$	
	stau pairs	muon pairs	stau pairs	muon pairs
124	0.567	0.087	1.660	0.158
154	0.179	0.084	0.555	0.145
185	0.063	0.072	0.190	0.126
216	0.024	0.047	0.080	0.127
247	0.010	0.027	0.038	0.119
278	0.004	0.037	0.015	0.060
309	0.002	0.015	0.007	0.070

Table 6.5.: Expected numbers of the stau pairs and the muon pairs in the stau region for the luminosities of 1.01 and 2.1 fb^{-1} .

The methods presented in section 6.2.1 and in this section give the expected numbers of the stau pairs and the muon pairs, which are comparable. These methods can cross-check each other.

In conclusion, in chapters 5 and 6, we have simulated the stau pairs and their backgrounds in the LHCb detector; we have defined the selection cuts to select the stau pairs. By analysing the stau and muon pairs by the neural network, we have evaluated the expected numbers of signal and background that could be observed in the data

collected in 2011 and 2012. In the last chapter of this thesis, we will apply to the selection to the data.

Chapter 7.

Results

In this chapter, the analysis procedure outlined in the previous chapters will be applied: we will first pass the events through the selection cuts, then classify the selected events using the NN trained by the MC events. We will also have a look at the two events observed in the stau region. The systematic errors will then be discussed. Finally, the limit on the cross section for stau pair production will be presented.

The data we used have been selected by the *Z02MuMu* stripping line, the stripping was of the version 17 for the 2011 data and 20 for the 2012 data.

7.1. Selection

Applying the cuts defined in section 5.3, we get the numbers of pairs from the 2011 and 2012 data that are, respectively, listed in tables 7.1 and 7.2. We remind that the selection cuts depend on the mass of the stau. The selected numbers are smaller than the ones expected by MC (table 5.11), but they are compatible by taking account of the uncertainties.

The data analysis is presented in the case of the stau of $124 \text{ GeV}/c^2$ mass with the NN trained for this stau mass. Before analysing these data, we present in figures 7.1 and 7.2 the distributions of the kinetic variables of the pairs selected by the cuts corresponding to staus of $124 \text{ GeV}/c^2$ mass.

$m_{\tilde{\tau}}$ (GeV/c ²)	124	154	185	216	247	278	309
Selected events	206	206	206	196	178	178	116

Table 7.1.: The numbers of pairs selected by the cuts in the 2011 data.

$m_{\tilde{\tau}} \text{ (GeV/c}^2\text{)}$	124	154	185	216	247	278	309
Selected events	609	609	609	587	532	446	380

Table 7.2.: The numbers of pairs selected by the cuts in the 2012 data.

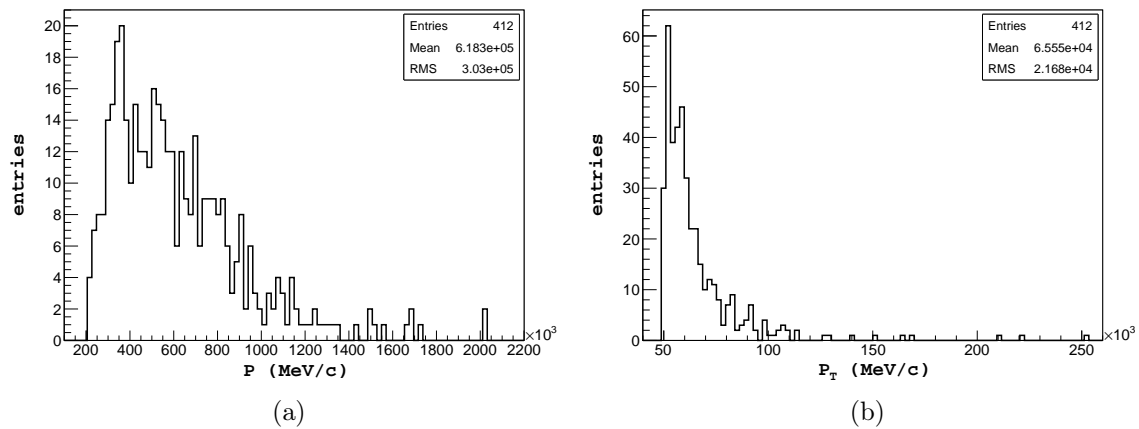


Figure 7.1.: P and P_T of the tracks of the pairs selected in the 2011 data by the selection cuts corresponding to staus of $124 \text{ GeV}/c^2$ mass.

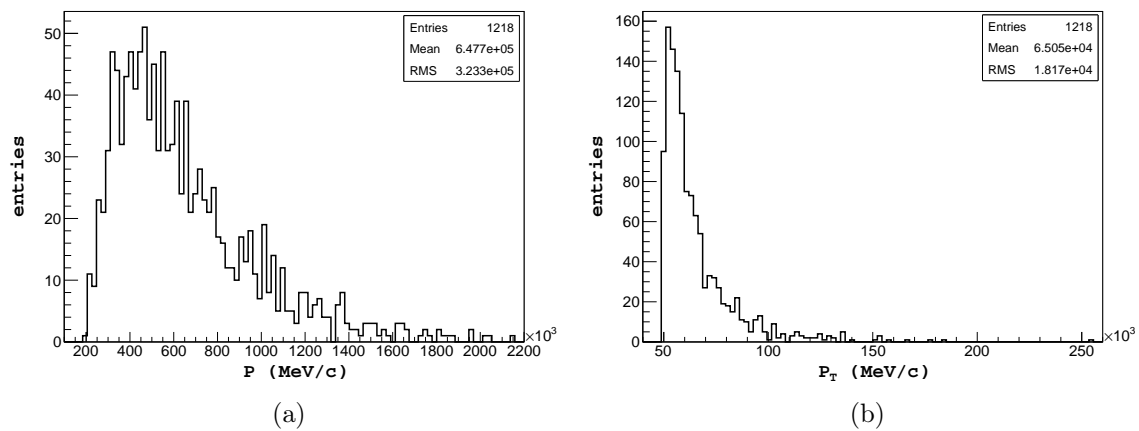
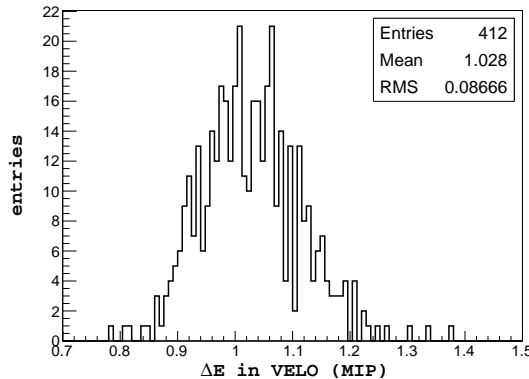


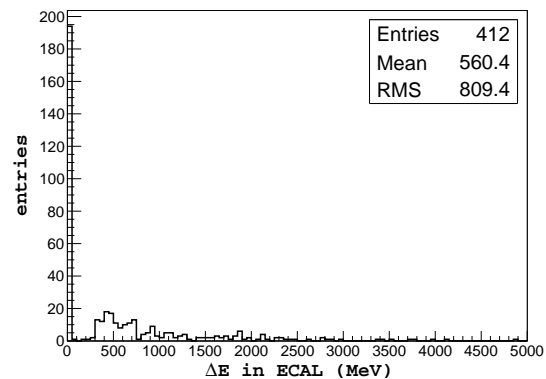
Figure 7.2.: P and P_T of the tracks of the pairs selected in the 2012 data by the selection cuts corresponding to staus of $124 \text{ GeV}/c^2$ mass.

7.2. Analysis of the tracks with Neural Network

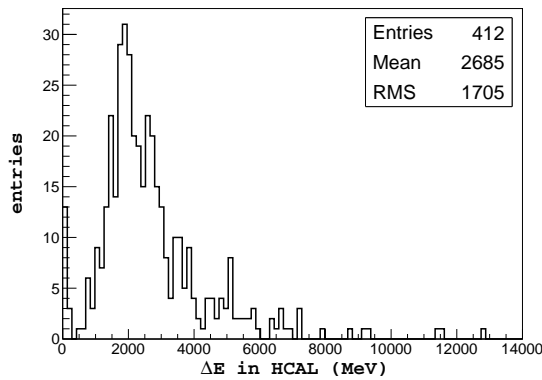
In this section, we present the classification of the tracks according to the NN. The input variables to the first Neural Network, i.e. the signals deposited by the tracks in the sub-detectors, are drawn in figures 7.3 and 7.4 for the 2011 and 2012 data, respectively. These are: the average energy deposition in a VELO sensor, the total energy deposition in the ECAL, the total energy deposition in the HCAL and the delta log-likelihood value for below-threshold particle hypothesis (DLLbt) given by the RICHs. The high value of the first bin in the ECAL response is due to the fact that the tracks have an amount of energy depositions smaller than the readout thresholds of the calorimeters.



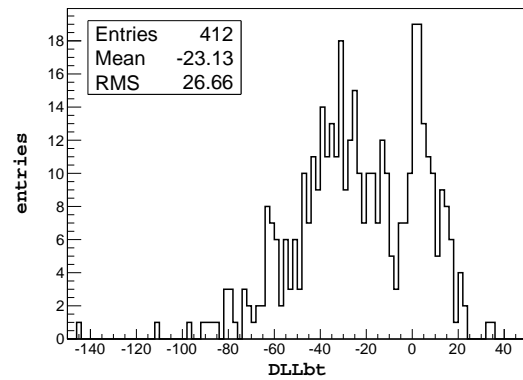
(a) Average energy deposition in a VELO sensor



(b) Total energy deposition in the ECAL



(c) Total energy deposition in the HCAL



(d) Delta log-likelihood for below-threshold particle hypothesis (DLLbt)

Figure 7.3.: The input variables to the first NN. The tracks are selected from the 2011 data and the selection cuts correspond to staus of the $124 \text{ GeV}/c^2$ mass.

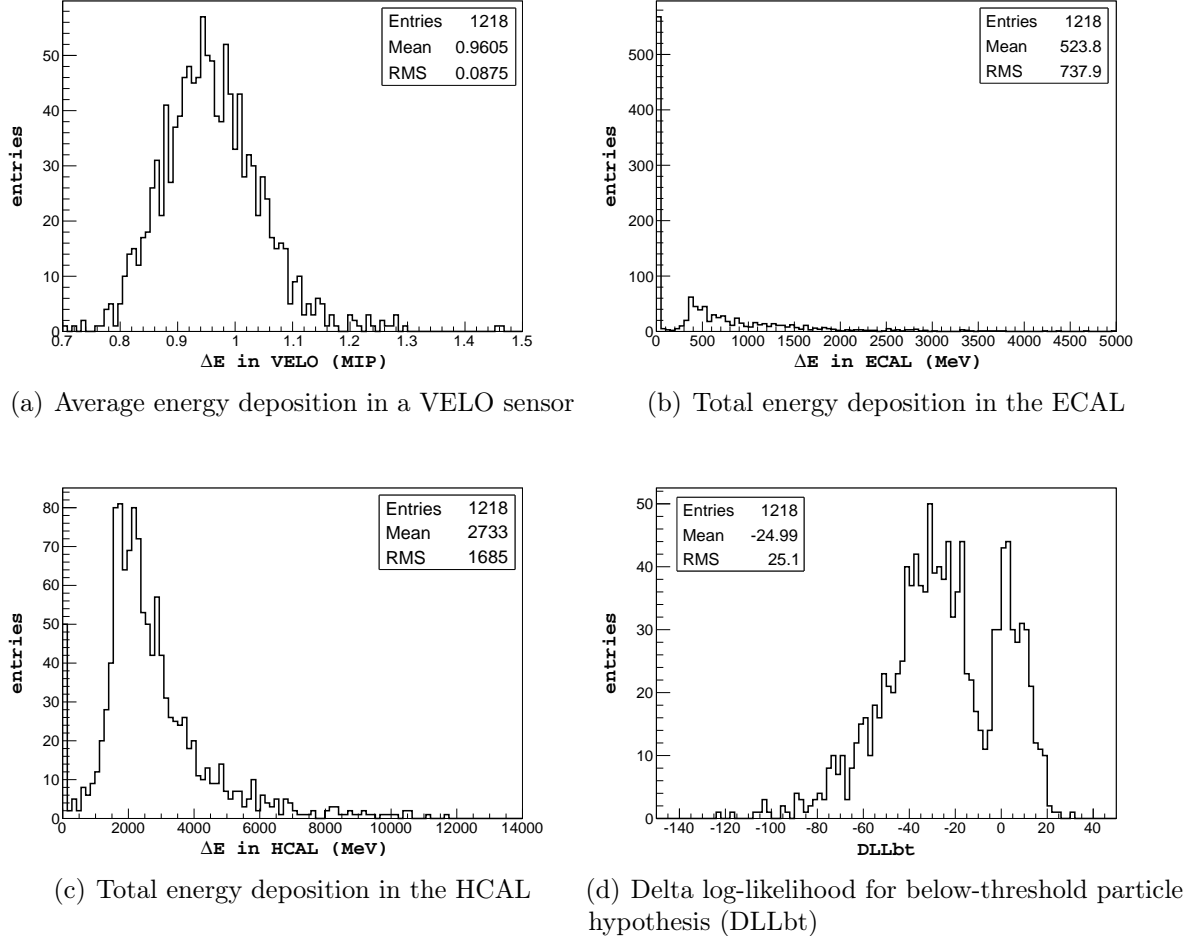


Figure 7.4.: The input variables to the first NN. The tracks are selected from the 2012 data and the selection cuts correspond to staus of the $124 \text{ GeV}/c^2$ mass.

In the first step, we will use the NN1 trained with the calibrated MC responses to classify the selected tracks. The NN1 classification is presented in figure 7.5 for the tracks of the 2011 and 2012 data. The distributions peak at zero, showing that most of the tracks are muons.

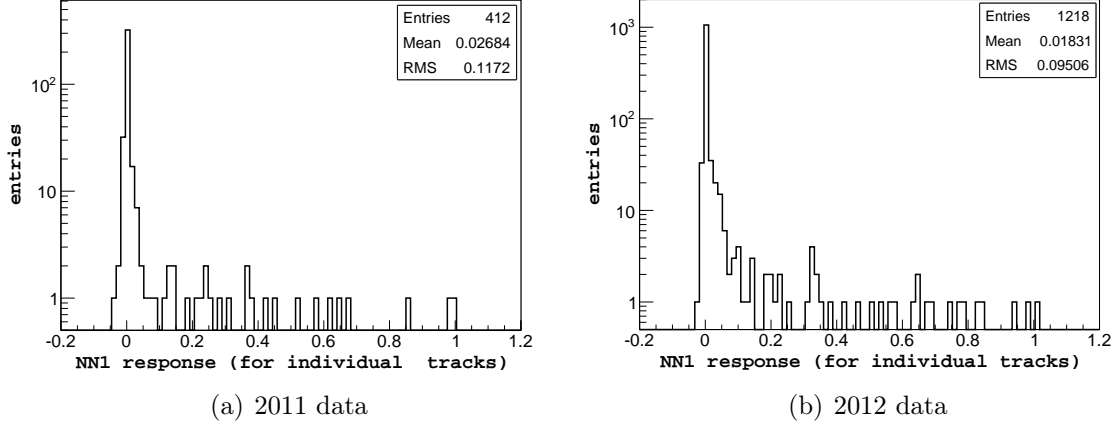


Figure 7.5.: NN1 classification for tracks selected according to criteria defined for stau mass of $124 \text{ GeV}/c^2$.

7.3. Selection of the stau pairs

7.3.1. Selection based on the pair significance

In this section, we present the selection based on the pair significance (see section 6.2.1). The NN1 responses for the tracks in section 7.2 are employed to compute the pair significance, which is shown in figure 7.6. After applying the cuts on the pair significance (table 6.1), we found no event. This is compatible with the expected number of the background.

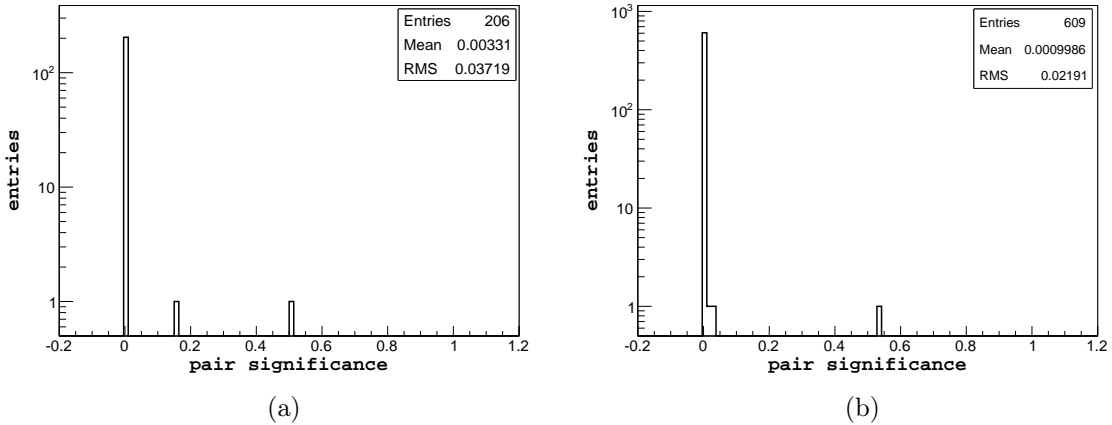


Figure 7.6.: Pair significance of the pairs selected from the 2011 data (a) and 2012 data (b) with the selection cuts corresponding to the case of the $124 \text{ GeV}/c^2$ mass.

7.3.2. Selection based on the pair significance and the invariant mass of the pairs

In this section, we present the selection based on the pair significance and the invariant mass of the pairs (see section 6.2.2) for the data. The pair significance was shown in figure 7.6. The invariant mass of the pair is presented in figures 7.7. We remind that the invariant mass is calculated assuming the mass of each particle to be that of a muon.

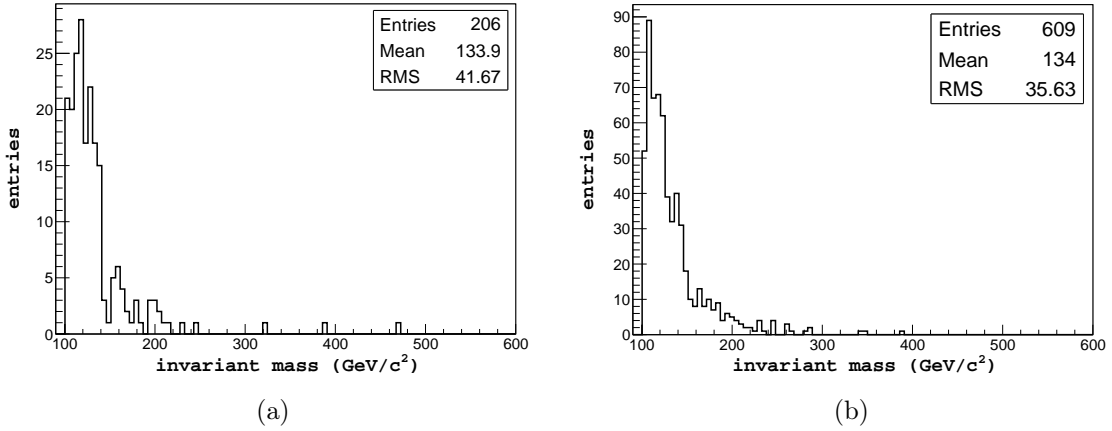


Figure 7.7.: Invariant mass of the pairs selected from the 2011 data (a) and the 2012 data (b) with the selection cuts corresponding to the case of the 124 GeV/c² mass.

To classify the data we input the variables shown in figures 7.6 and 7.7, into a second trained NN; we obtain the NN2 classification displayed in figures 7.8(a) and 7.9(a) for 2011 and 2012 data, respectively. The NN2 response peaks at zero, corresponding to the value of muon pairs.

In section 6.2.2, we defined a cut at 0.8 on the NN2 response to identify the region for the stau pair. In the case of the 124 GeV/c² stau mass, we observe one event in this region in the 2011 data sample and one event in 2012 data sample. These two events are both at a NN2 of 1, satisfying the hypothesis of being a stau pairs. In figures 7.8 and 7.9, these two events are displayed in magenta. Figures 7.8(b) and 7.9(b) draw the bi-parametric histograms of the pair significance and the invariant mass of the selected pairs.

The analysis process is the same for all other masses of the staus. The numbers of the observed pairs in the stau region corresponding to all the stau masses are listed in table 7.3 for the 2011 and 2012 data. The event observed in 2011 data is the same one in the analysis for four masses of stau, from 124 to 216 GeV/c². Similarly, we got the same event in 2012 data corresponding to the stau masses from 124 to 247 GeV/c². For the other higher masses of stau, these events were discarded by the cut on the momentum of the tracks. In the next sections, we will have a detailed look at these events.

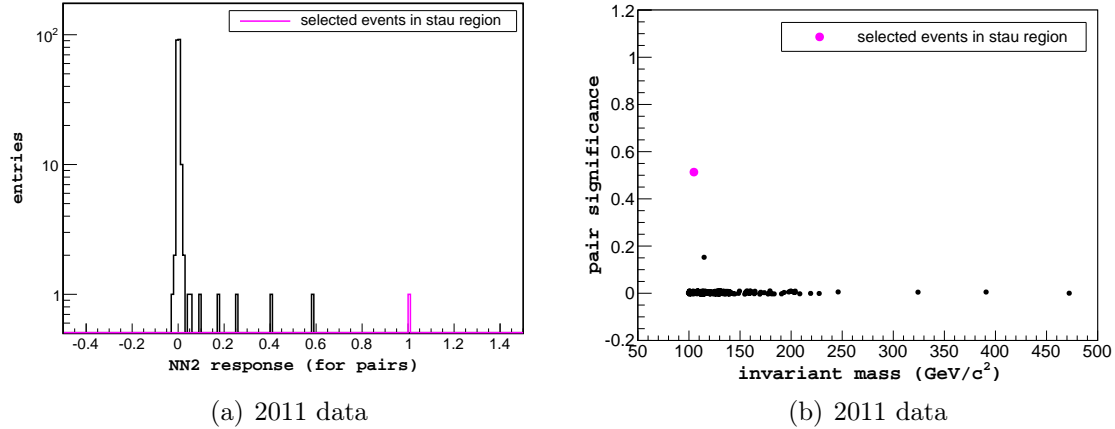


Figure 7.8.: NN2 response for the pairs selected by the cuts corresponding to the staus of 124 GeV/c^2 mass in the 2011 data.

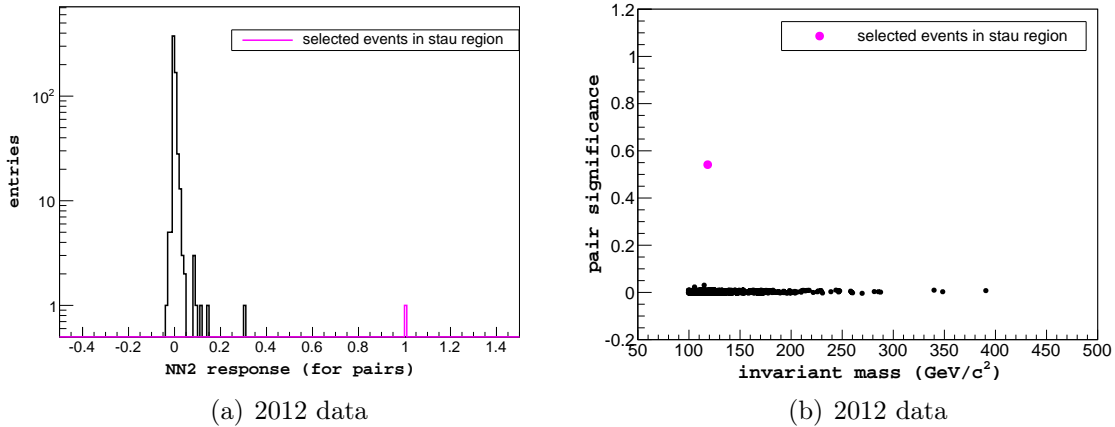


Figure 7.9.: NN2 response for the pairs selected by the cuts corresponding to the staus of 124 GeV/c^2 mass in the 2012 data.

$m_{\tilde{\tau}}$ (GeV/c^2)	124	154	185	216	247	278	309
2011 data	1	1	1	1	0	0	0
2012 data	1	1	1	1	1	0	0

Table 7.3.: The number of pairs observed in the stau region from 2011 and 2012 data.

Event surviving in the 2011 data

In this section, we examine the event observed in the 2011 data, displayed in the LHCb detector in figure 7.10. The two tracks of the pair are in magenta. Tracks with $P_T < 1$ GeV/c are not displayed. The negative and positive charges are, respectively, above and below the beam line in this figure. They are quite symmetric with respect to the beam line and straight due to their high momenta. Except the lack of signal from the negative track in the TT station, the signals in the all other sub-detectors are fully reconstructed: the interaction points in the VELO, TT and OT are displayed by the star markers, the energy depositions in ECAL and HCAL are respectively shown by red and blue columns, the interaction points in the muon chambers are marked by the green points and in the RICHs they are identified as below threshold particle. The information about the two tracks are presented in table 7.4. The track reconstruction parameters, σ_P/P and χ^2/ndof , show that they are of very good quality. The pair significance of this pair is around 0.51 and assuming the muon mass its invariant mass is 104 GeV/c².

	The negative track	The positive track
P (GeV/c)	257.18	383.15
P_T (GeV/c)	50.34	52.21
ΔE in ECAL (MeV)	388.67	706.32
ΔE in HCAL (MeV)	1952.77	1526.03
ΔE in VELO (MIP)	1.13	1.03
RICH PID	5	5
DLLbt	34.27	20.23
η	2.32	2.68
σ_P/P	0.027	0.012
χ^2/ndof	1.25	1.05

Table 7.4.: Reconstructed information from the candidate event from the 2011 data in the LHCb detector.

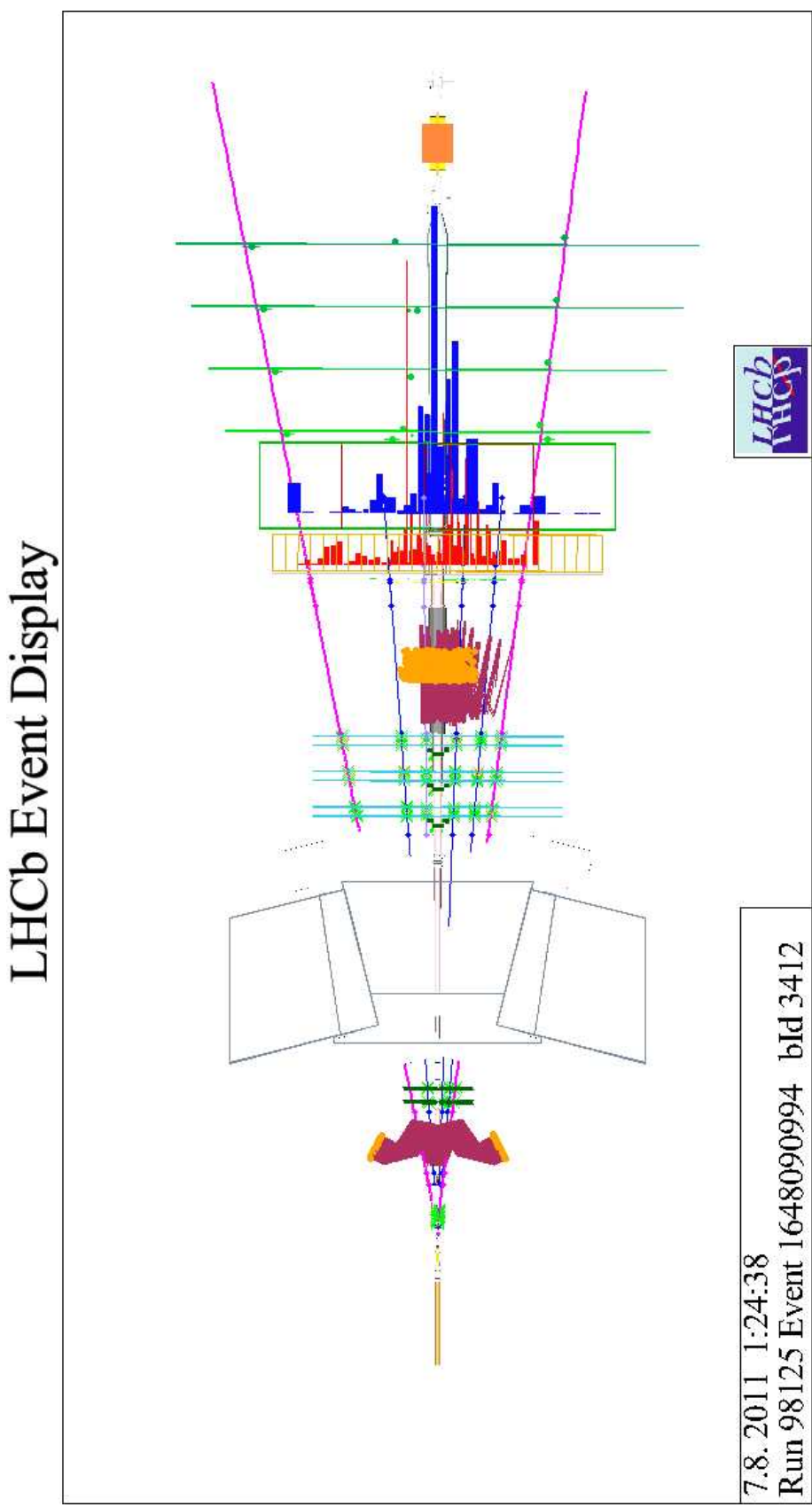


Figure 7.10.: Global view of the observed event from the 2011 data in the LHCb detector. The tracks with the $P_T < 1$ GeV/c are not displayed.

We now have a more detailed look at the geometry of the tracks with respect to the primary vertices (PVs) in this event. Figure 7.11 shows the positions of the two tracks of the pair and the reconstructed primary vertices. The PVs are displayed by the steel blue balls in figure (a) and the steel blue points in figure (b); the two tracks are in magenta. Table 7.5 presents the number of tracks, the coordinates and the chi-squared of the PVs. The two tracks belong to the primary vertex of the key number 0 and they have a closest approach distance of $1.4 \mu\text{m}$.

Key	Number of tracks	x (mm)	y (mm)	z(mm)	χ^2
0	45	0.427	-0.001	-56.38	0.358
1	10	0.486	-0.166	-23.696	0.497

Table 7.5.: Primary vertices reconstructed in the event observed from the 2011 data.

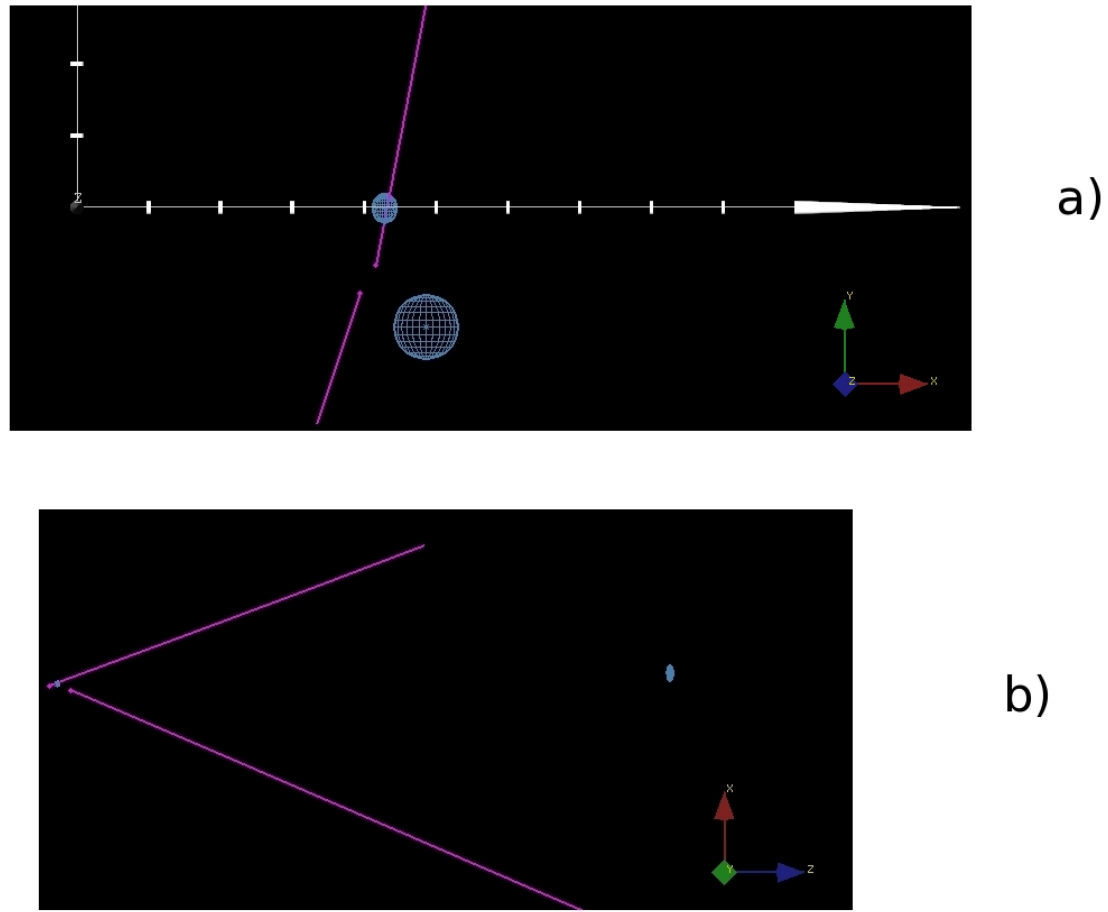


Figure 7.11.: Primary vertices reconstructed in the event observed from the 2011 data.

For a full view of the reconstructed track segments in the VELO detector, see figure 7.12. The two tracks of the observed pair are in magenta. The vertical lines are the VELO sensors.

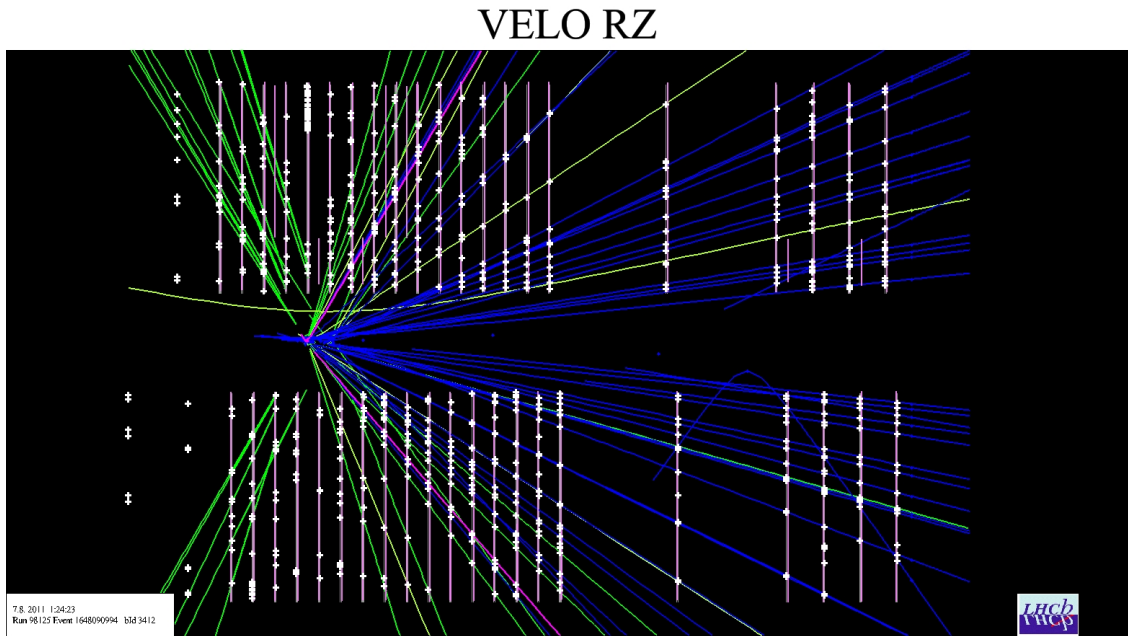


Figure 7.12.: The VELO track segments of the event observed from the 2011 data.

Event surviving in the 2012 data

In the same way as in previous section, we now have a detailed look at the event observed in the 2012 data. The global view of this event in the LHCb detector is displayed in figure 7.13. The tracks of the selected pair are also drawn in magenta. The tracks of the negative and positive charges are respectively below and above the beam line in the figure. The two tracks of the pair are not symmetric with respect to the beam line. These tracks are very straight due to their very high momenta. The negative track possesses a momentum (1032 GeV/c) much higher than the positive track (332 GeV/c). The interaction points of the tracks in the sub-detectors are displayed in the same way as for the event of the 2011 data. Their detailed information is listed in table 7.6.

The negative track has no energy depositions in the ECAL and HCAL. This can be explained as follows: this track makes an angle of 56 mrad with respect to the beam line, this means that it is in the inner region of the calorimeters and has an energy deposition smaller than the readout thresholds of the calorimeters.

LHCb Event Display

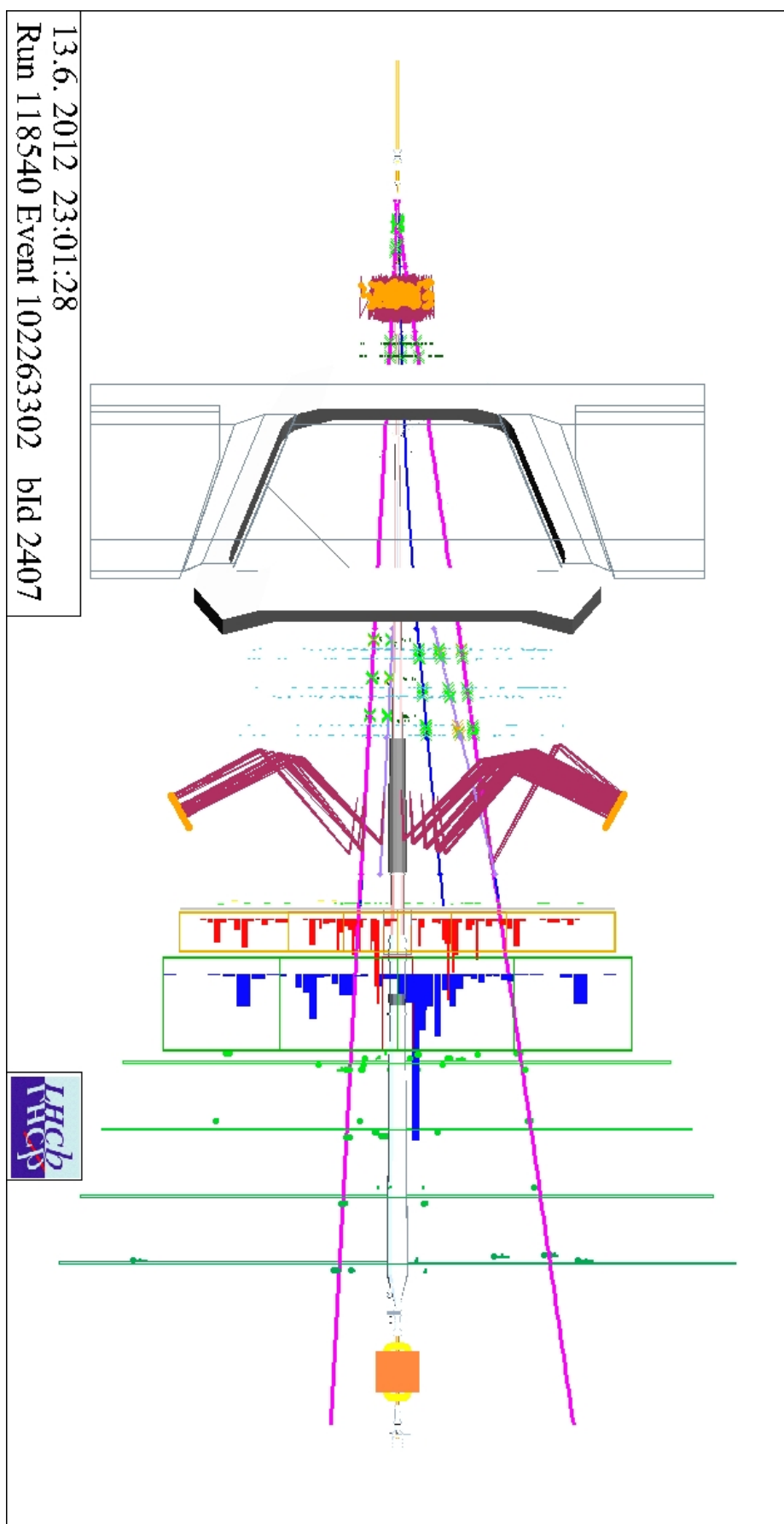


Figure 7.13.: Panorama of the observed event from the 2012 data in the LHCb detector. The tracks with the $P_T < 1 \text{ GeV}/c$ are not displayed.

	The negative track	The positive track
P (GeV/c)	1032.7	332.3
P_T (GeV/c)	58.3	50.3
ΔE in ECAL (MeV)	0	535
ΔE in HCAL (MeV)	0	1617
ΔE in VELO (MIP)	1.08	0.83
RICH PID	5	5
DLLbt	19.74	18.49
η	3.57	2.58
σ_P/P	0.025	0.01
χ^2/ndof	0.87	1.04

Table 7.6.: Reconstructed information of the observed event from the 2012 data in the LHCb detector.

Similar to the event of the 2011 data, we examine the geometry of the tracks with respect to the primary vertices in this event. The two tracks and the reconstructed primary vertices are displayed in figure 7.14. The two tracks are still shown in magenta, while the PVs are presented by the green balls in figure (a) and the green points in figure (b). Two PVs were reconstructed in this event and their information is listed in table 7.7. The observed pair belongs to the primary vertex having the key number 1 and they have a closest approach distance of $0.3 \mu\text{m}$.

Key	Number of tracks	x (mm)	y (mm)	z(mm)	χ^2
0	18	0.652	0.035	58.807	0.996
1	18	0.621	0.103	86.562	0.465

Table 7.7.: Primary vertices reconstructed in the event observed from the 2012 data.

We also present the track segments reconstructed in the VELO detector in figure 7.15 with four muon tracks displayed in magenta, where the two tracks of the observed pair are the outermost ones.

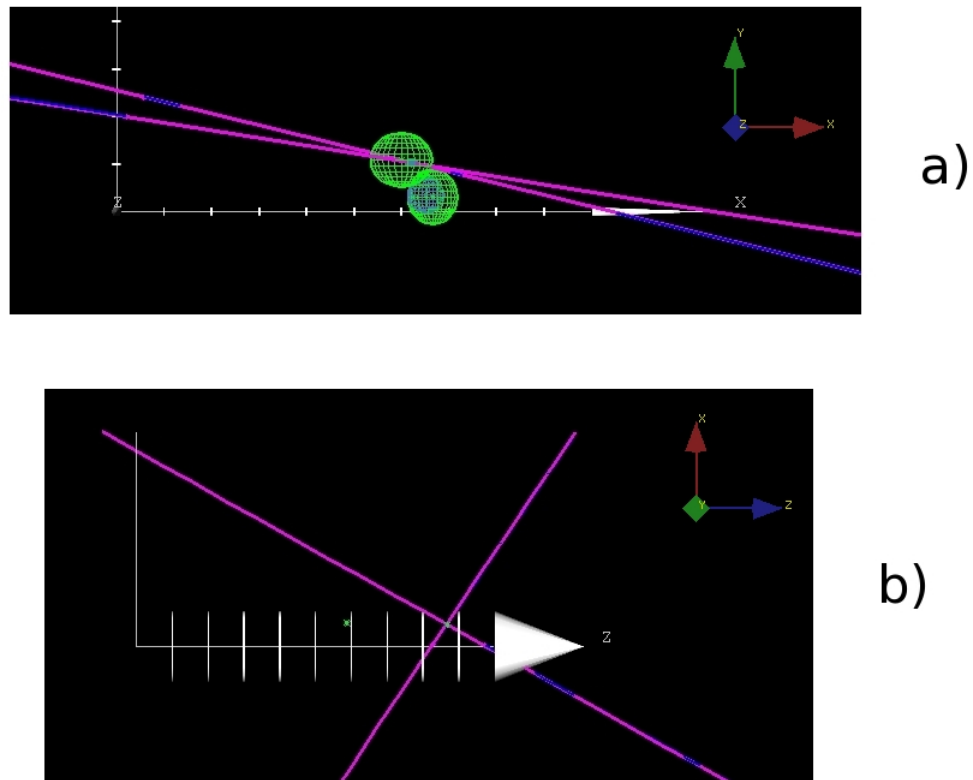


Figure 7.14.: Primary vertices reconstructed in the event observed from the 2012 data.

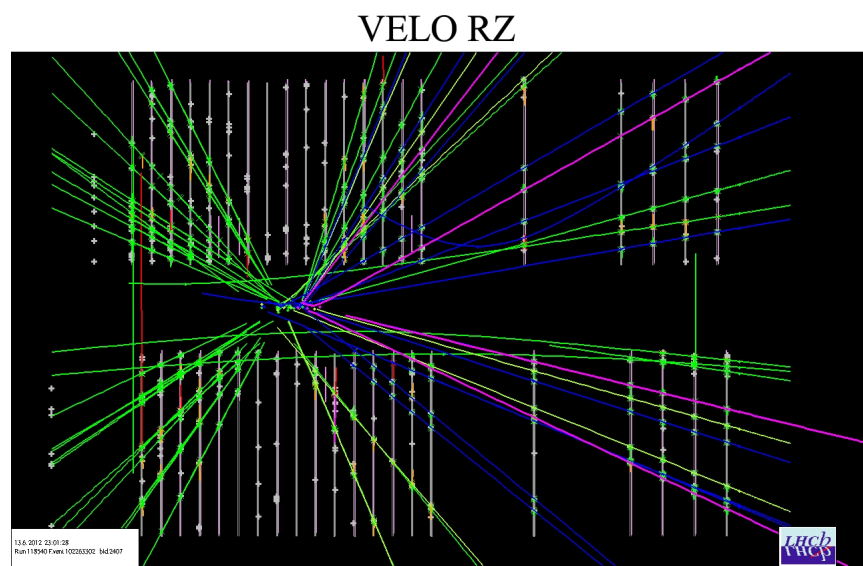


Figure 7.15.: The VELO track segments of the event observed from the 2012 data.

The invariant mass of the pair is $121 \text{ GeV}/c^2$ assuming the muon mass and its pair significance is around 0.54.

While the selection method based on the pair significance gives no observed event, this second method found two events, which is much higher than the total expected numbers of stau pairs and muon pairs, except the case of the $124 \text{ GeV}/c^2$ staus. Even though the NN2 responses for these two events peak at 1, the pair significance and the invariant mass of the pair are quite low. Moreover, the most sensitive criterion for the separation of muons and staus, namely the DLLbt, lie around 20, except for the negative track of the 2011 event. Such a value does not allow us to unambiguously claim that stau pairs have been observed. In section 7.5, we will compute the upper limits for both cases with two observed event and without observed event.

7.4. Systematics

The expected numbers of observed events predicted by the Monte Carlo for staus and muons are affected by systematic uncertainties. In this section, we will consider the different sources of these uncertainties.

Luminosity

The LHCb experiment uses two methods to measure the luminosity. One method is the "van der Meer scan", the other one is a method based on the high resolution of the VELO detector [47]. Both methods are in good agreement and can give a precision of 3.5% in the absolute luminosity measurement. The datasets of 2011 and 2012 used in this analysis correspond to the integrated luminosities of $1.01 \pm 0.035 \text{ fb}^{-1}$ and of $2.1 \pm 0.105 \text{ fb}^{-1}$, respectively. The uncertainties on the integrated luminosities are 3.5% for the 2011 dataset and 5% for the 2012 dataset.

Cross section

The cross section for stau pair production is computed by the Prospino2.1 programme (see section 5.1). The uncertainties on the cross section come from the uncertainties on the parton distribution function (PDF), on the energy scale and on the strong coupling.

- *Uncertainty on the energy scale:* Prospino sets the re-normalisation and factorization scales (Q) as the mass of the participating particles to compute the cross-section. This arbitrary choice leads to an uncertainty on the calculated cross section. To estimate this uncertainty, the scale is varied between $Q/2$ and $2*Q$. Then, the uncertainty will be taken as the differences between the cross sections corresponding to the scales of $Q/2$ and Q , Q and $2*Q$. Therefore, this is an asymmetric uncertainty ($\delta_{s,\text{up}}$ and $\delta_{s,\text{down}}$).

- *Uncertainty from PDF*: In Prospino2.1, we use the parton distribution function CTEQ6.6. To estimate the uncertainty from this PDF, one calculates the cross section with the 44 different PDFs which correspond to the 22 variations (up and down) of the CTEQ6.6 in the range of the uncertainties coming from the experimental errors. Then one calculates the uncertainties by:

$$\delta_{\text{PDF,up}} = \sqrt{\sum_{i=1}^{22} (\max[\sigma^+ - \sigma^0, \sigma^- - \sigma^0])^2} \quad (7.1)$$

$$\delta_{\text{PDF,down}} = \sqrt{\sum_{i=1}^{22} (\max[\sigma^0 - \sigma^+, \sigma^0 - \sigma^-])^2} \quad (7.2)$$

where σ^+ is the cross section corresponding to the up variation, σ^- corresponds to the down variation and σ^0 the central value without variation.

- *Uncertainty from the strong coupling*: This uncertainty is estimated by varying the strong coupling α_s in the uncertainty range of one sigma (up and down).

Finally, the uncertainties on the cross section [48] are:

$$\delta_{\text{up}} = \sqrt{\delta_{s,\text{up}}^2 + \delta_{\text{PDF,up}}^2 + \delta_{\alpha_s,\text{up}}^2} \quad (7.3)$$

$$\delta_{\text{down}} = \sqrt{\delta_{s,\text{down}}^2 + \delta_{\text{PDF,down}}^2 + \delta_{\alpha_s,\text{down}}^2} \quad (7.4)$$

The relative uncertainties in percent on the the cross section for stau pair production are listed in table 7.8.

$m_{\tilde{\tau}}$ (GeV/c ²)	σ (pb) in $\sqrt{s} = 7$ TeV	σ (pb) in $\sqrt{s} = 8$ TeV
124	0.016900 (pb) $\begin{array}{l} +5.0(\%) \\ -4.4(\%) \end{array}$	0.02120 (pb) $\begin{array}{l} +3.8(\%) \\ -4.8(\%) \end{array}$
154	0.007190 $\begin{array}{l} +6.1 \\ -4.6 \end{array}$	0.00920 $\begin{array}{l} +5.6 \\ -4.3 \end{array}$
185	0.003440 $\begin{array}{l} +6.6 \\ -4.9 \end{array}$	0.00450 $\begin{array}{l} +5.9 \\ -4.7 \end{array}$
216	0.001790 $\begin{array}{l} +6.8 \\ -5.3 \end{array}$	0.00239 $\begin{array}{l} +6.7 \\ -4.8 \end{array}$
247	0.000988 $\begin{array}{l} +7.5 \\ -5.8 \end{array}$	0.00135 $\begin{array}{l} +7.1 \\ -5.4 \end{array}$
278	0.000572 $\begin{array}{l} +7.6 \\ -6.2 \end{array}$	0.00080 $\begin{array}{l} +7.0 \\ -5.9 \end{array}$
309	0.000344 $\begin{array}{l} +8.6 \\ -6.0 \end{array}$	0.00049 $\begin{array}{l} +7.9 \\ -5.9 \end{array}$

Table 7.8.: Cross section of the stau pair production at pp collisions at $\sqrt{s} = 7$ and 8 TeV. The systematic uncertainties (%) are relative ones.

The systematic errors on the cross section of $Z^0, \gamma^* \rightarrow \mu^+ \mu^-$ were discussed in section 5.2.2. The total relative systematic error is the sum in quadrature of the errors on the PDF and on the theory. The values are listed in table 7.9.

	σ (pb)
at $\sqrt{s} = 7$ TeV	1.065 $^{+7.6}_{-6.3}$
at $\sqrt{s} = 8$ TeV	1.24 $^{+8.9}_{-6.7}$

Table 7.9.: Cross section of the decay $Z, \gamma^* \rightarrow \mu^+ \mu^-$ in pp collisions at $\sqrt{s} = 7$ and 8 TeV. The systematic uncertainties (%) are relative ones.

Selection cuts:

The simulation and reconstruction by MC might be not perfect to describe the data. This will make the efficiencies predicted by MC different from those of the data when we apply the selection cuts, resulting in an uncertainty in the expected number of the stau pair candidates, as well as the expected number of the muon pairs, and hence in the upper limits of the production cross section of stau pairs.

In section 5.3, we used thirteen cuts to select the stau pairs, where the first four of them choose a good muon track, the fifth one is the cut on trigger and the remaining additional cuts are to reduce the muon background. Here, we will consider the uncertainty contributions from the muon tracking, the trigger and the additional cuts separately.

- *Muon tracking:* We will here compare the muon tracking efficiencies from MC and data for the tracks of $P_T > 50$ GeV/c. In section 5.3, to select a good muon track, we used four cuts: long track, $IsMuon = 1$, $\chi^2/dof < 3$ and $\sigma_P/P < 0.1$. For both MC and data, we use the samples of $Z^0, \gamma^* \rightarrow \mu^+ \mu^-$ with a mass window $80 < M_{\mu\mu} < 100$ GeV/c², then we count the number of tracks having $P_T > 50$ GeV/c and the fraction of these tracks passing the above cuts. This fraction is considered as the muon tracking efficiency. This is applied for the positive and negative tracks separately. The muon tracking efficiency for a pair will be the product of the ones for the minus track and the plus track. The efficiencies are given in table 7.10. The difference between the efficiencies for the pair given by the MC and data will be considered as the uncertainty on the muon tracking efficiency for the pair predicted by MC. Table 7.10 shows that the MC reconstructs the tracks more efficiently than the data. However, the uncertainties will be taken in both directions. This uncertainty is $\pm 6.7\%$ for MC11 and $\pm 22\%$ for MC12.

- *Trigger:* In our selection, we demanded at least one track of the pair to fire the trigger on single muon of high P_T . In order to estimate the difference between the trigger efficiencies from MC and data, we choose the muon pairs which are selected by the $Z02MuMu$ stripping line, have an invariant mass $M_{\text{pair}} > 100$ GeV/c² and $P_T > 50$

	ε_{μ^-}	ε_{μ^+}	$\varepsilon_{\mu^-} \times \varepsilon_{\mu^+}$
MC11	0.997	0.996	0.993
Data 2011	0.961	0.964	0.926
MC12	0.999	0.998	0.997
Data 2012	0.881	0.882	0.777

Table 7.10.: Efficiencies of the muon tracking.

GeV/c for each track and ask the tracks to have good quality according to the four criteria given in the previous paragraph. Then, we count the fraction of the pairs which satisfy the above trigger cut. These fractions given by MC and data are listed in table 7.11. The systematic uncertainty on the trigger can be taken as the difference between the fractions given by MC and data. The values in table 7.11 show that the trigger described by MC is a little less efficient than the data. Symmetric uncertainties will be taken. The uncertainty is therefore $\pm 1.5\%$ for the MC11 trigger and $\pm 3\%$ for MC12 trigger.

	MC11	Data 2011	MC12	Data 2012
ε_{trig}	0.915	0.929	0.901	0.928

Table 7.11.: Efficiencies of the trigger cut.

We would like to comment here that the data sample we used in the estimation of this uncertainty might contain the stau pair candidates. However, since we have seen in the previous sections that the data is dominated by the muon pairs from Z^0, γ^* and that there is only one stau pair candidate, the estimation is therefore correct.

- *Additional cuts:* As we mentioned above, any imperfection in the description of the data by MC will lead to an imprecision on the selection efficiencies predicted by MC when we apply the cuts on the variables. Here we will estimate the difference between the efficiencies for the MC and data due to the additional cuts, i.e. the last eight cuts listed in section 5.3. We use two samples: one is MC and another is data. The two samples contain the pairs with an invariant mass $M_{\text{pair}} > 100 \text{ GeV}/c^2$ and $P_T > 50 \text{ GeV}/c$ for each track. The tracks are of good quality and the pairs pass the trigger cut. Then, we count the fraction of these pairs which satisfy the additional cuts. The fractions given by the MC and data samples are different and are given in table 7.12. The difference between these fractions given by the MC and data will be taken as the uncertainty due to the additional cuts. They are $\pm 27.8\%$ for MC11 and $\pm 20\%$ for MC12. In this estimation, the statistics from the data sample was limited, but we will still accept these results.

	MC11	Data 2011	MC12	Data 2012
ε_{add}	0.219	0.280	0.249	0.296

Table 7.12.: The differences between the efficiencies when the additional cuts are applied.

The uncertainties on the muon tracking, the trigger and the additional cuts contribute to the total uncertainty on the selection efficiencies for the muon pairs that we described in section 5.3. We take the sum of these uncertainties in quadrature as in table 7.13. This estimation is done with the selection cuts corresponding to the stau of $124 \text{ GeV}/c^2$ mass. For the selection cuts corresponding to the other stau masses, only the cut on the momentum is changed. Therefore, the uncertainties obtained in table 7.13 can be used in the remaining cases as a good estimate.

	MC11	MC12
muon tracking	6.7	22.0
trigger	1.5	3
additional cuts	27.8	20.0
total	28.6	29.8

Table 7.13.: Total uncertainty (%) on the selection efficiencies for the muon pairs.

For the stau pairs, there is no data sample to evaluate the uncertainty on their selection. However, the selection efficiencies for stau pairs are not immune from such an uncertainty. We have seen in chapter 5 that among the variables on which we impose a cut, only the distributions of P (see figures 5.9 and 5.10) and $(E_{\text{ECAL}} + E_{\text{HCAL}})/P$ (see figure 5.23(a)) for the staus and muons are quite different, the others are not very different. Therefore, we will use the uncertainties on the muon pairs for the staus as a good estimate.

Neural Network

- Even though we tried to calibrate the energy depositions of the particles in ECAL and HCAL, these depositions in MC and data are not in perfect agreement. This can be seen in figures 5.19, 5.20, 5.21, 5.22, in particular because of the peaks and the first bin of the histograms. This disagreement certainly brings a systematic error on the percentages (R) of the stau and muon pairs falling in the stau region given by the Neural Network when we apply the cut on NN2 (see section 6.2).

To estimate this error for muon pairs, we generated again the energy deposition in ECAL for the MC muons that we used to train the NN using the energy deposition

distribution from the data. All other variables used as inputs to the first NN were kept the same as before. Then, we trained the NN again with this re-generated energy deposition in ECAL. The difference between the efficiencies due to the cut of 0.8 on NN2 that we get before and after re-generating the energy deposition in ECAL is considered as the systematic error on the muon percentage falling in the stau region. We did the same for the energy deposition in HCAL of the MC muons.

These errors are estimated for the muon background only. For the MC staus, there is no sample from data to compare to.

- We have seen in figures 6.5 and 6.3 the low statistics for the muon pairs at high values of the NN2 response and of the pair significance, respectively. This also leads to an error on the percentage of the muon pairs falling into the stau region. To estimate the size of this error, we take the difference between the percentages given by the training and testing samples. These two samples come from a larger sample and have the same statistics. This error can be neglected for the staus since its statistics are large enough in the stau region.

The total error on the percentage of the muon pairs in the stau region due to the NN is now the sum in quadrature of the errors due to the energy depositions in ECAL, HCAL and due to low statistics. These errors are 18.8% and 31.0% for the MC11 and MC12, respectively. The estimation of the errors were achieved using the staus of 124 GeV/c^2 mass, and the result will be used for all the remaining cases of staus.

Total systematic uncertainties:

Finally, we compute the total systematic uncertainty by taking the sum in quadrature of all components. For the stau pairs, the contributions come from the luminosity, the cross section and the selection cuts. The values estimated for the 2011 and 2012 data are presented in tables 7.14 and 7.15, respectively.

$m_{\tilde{\tau}}$ (GeV/c^2)	124	154	185	216	247	278	309
systematic uncertainty (%)	+29.2 -29.1	+29.4 -29.2	+29.6 -29.2	+29.6 -29.3	+29.8 -29.4	+29.8 -29.5	+30.1 -29.4

Table 7.14.: The total uncertainties on the expected number of the stau pairs in the stau region estimated for 2011 data.

For the muon background, the total systematic uncertainty comes from the uncertainties on the luminosity, the cross section, the selection cuts and the neural network. These total uncertainties are shown in table 7.16.

$m_{\tilde{\tau}}$ (GeV/c ²)	124	154	185	216	247	278	309
systematic uncertainty (%)	+30.5 -30.6	+30.7 -30.5	+30.8 -30.6	+30.9 -30.6	+31.0 -30.7	+31.0 -30.8	+31.2 -30.9

Table 7.15.: The total uncertainties on the expected number of the stau pairs in the stau region estimated for 2012 data.

	2011 data	2012 data
Total uncertainty (%)	+35.2 -34.9	+43.2 -42.9

Table 7.16.: The total uncertainties on the expected numbers of the muon pairs estimated for 2011 and 2012 data.

7.5. Limit on cross section

We have observed two candidate events: one in the 2011 data and another in the 2012 data. One can compute the upper limits using the observed number (n_{obs}) and the expected number of backgrounds (b). These limits are the observed upper limit which corresponds to n_{obs} and the expected limit which shows the sensitivity of the experiment.

The systematic uncertainty affects the estimation of the upper limits. To incorporate the systematic uncertainty on the background in the calculation of the upper limits, we will use the profile likelihood method [49], [50], [53]. This method is a generalization of the Feldman-Cousins approach (F-C) [51]. The likelihood function is now defined as:

$$L = P(n_{\text{obs}}|\mu + b) \times G(b_0|b; \sigma_b) \quad (7.5)$$

where $P(n_{\text{obs}}|\mu + b)$ is the probability density function of a Poisson process with μ being the parameter of interest, i.e. the number of signal events in our computation. $G(b_0|b; \sigma_b)$ is a Gaussian constraint, which expresses the systematic uncertainty on the background. The parameter b_0 is called the global observable.

The upper limits on the cross section at a certain confidence level (CL) are then calculated by dividing the corresponding parameter of interest (μ) by the stau pair "acceptance", which is defined as $L \times \epsilon \times A \times R$, the parameters L , ϵ , A and R being those of the considered stau.

The calculation is achieved using RooStats [52], [53], which is implemented within the ROOT program [54].

In our analysis, we have used two method to select the stau pairs and these two methods give two different results: the selection method based on the pair significance gives no observed event, the selection method based on the pair significance and the invariant mass of pair gives two observed events. We will compute the observed upper

limit and expected upper limit at 95%CL on the cross section for the stau pair production at $\sqrt{s} = 7$ and 8 TeV for both cases.

Limits in the case where no event has been observed

The observed upper limits and the expected upper limits are presented in tables 7.17 and 7.18. The figures 7.16 and 7.17 draw these limits and the predictions from the theory at NLO. The bands of one and two sigmas on the expected upper limits are also drawn in these figures. Without any observed event, the observed upper limits are always lower than the expected upper limits.

Mass	NLO prediction (pb)	Observed limit (pb)	Expected limit(pb)
124	0.0169	0.0746	0.0815
154	0.00719	0.1000	0.1090
185	0.00344	0.1341	0.1458
216	0.00179	0.1739	0.2063
247	0.000988	0.2615	0.2817
278	0.000572	0.3678	0.3965
309	0.000344	0.4441	0.5205

Table 7.17.: Cross section for stau pair production at $\sqrt{s} = 7$ TeV as predicted by theory at the NLO and the upper limits in the case where no event has been observed.

Mass	NLO prediction (pb)	Observed limit (pb)	Expected limit(pb)
124	0.0212	0.0481	0.0534
154	0.0092	0.0601	0.0668
185	0.0045	0.0747	0.0830
216	0.00239	0.0955	0.1018
247	0.00135	0.1083	0.1395
278	0.0008	0.1742	0.1968
309	0.00049	0.2240	0.2741

Table 7.18.: Cross section for stau pair production at $\sqrt{s} = 8$ TeV as predicted by theory at the NLO and the upper limits in the case where no event has been observed.

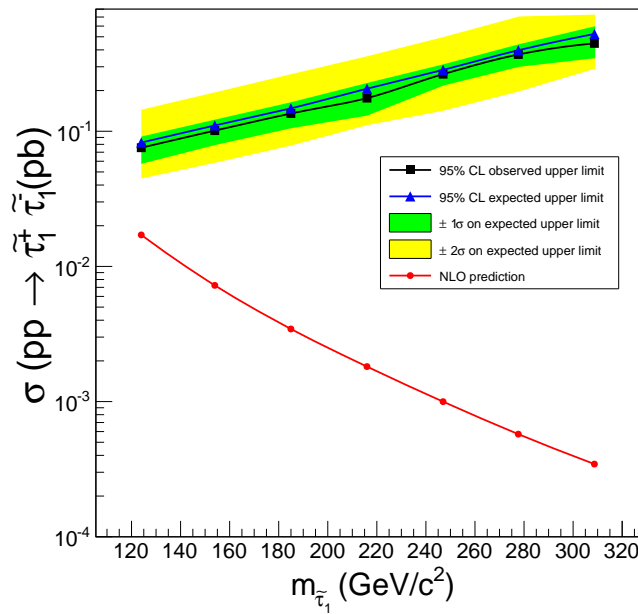


Figure 7.16.: Upper limits on the cross section for stau pair production in the pp collisions at $\sqrt{s} = 7$ TeV (no event observed).

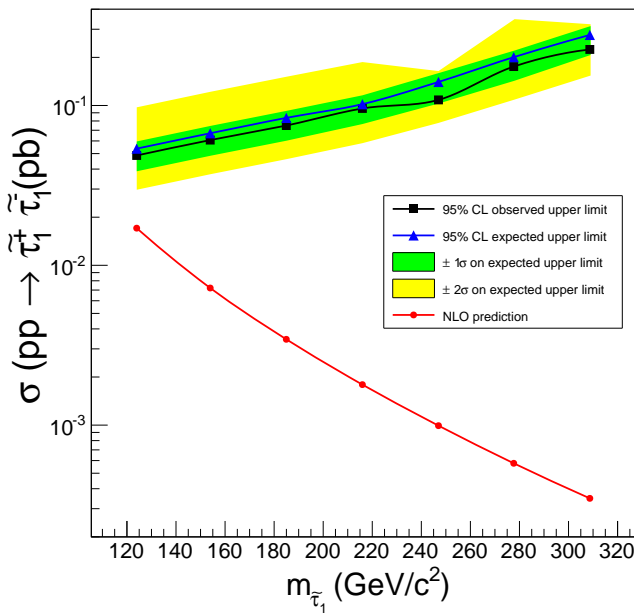


Figure 7.17.: Upper limits on the cross section for stau pair production in the pp collisions at $\sqrt{s} = 8$ TeV (no event observed).

Limits with two observed events

The observed upper limits and the expected upper limits are presented in tables 7.19 and 7.20. Similarly, the figures 7.18 and 7.19 show these limits and the predictions from the theory at NLO. The bands of one and two sigmas on the expected upper limits are also drawn in these figures. We see that the upper limits at $\sqrt{s} = 8$ TeV are smaller than the corresponding ones at $\sqrt{s} = 7$ TeV because the stau pair acceptance at 8 TeV is higher than the one at 7 TeV. We also see in these figures that the observed upper limits are smaller than the expected upper limits in the cases where no event has been observed, i.e. for stau masses from 247 to 309 GeV 2 . The fact that the observed and expected upper limits increase with the stau mass is due to a decrease of the stau pair acceptances as we go to higher masses.

Mass	NLO prediction (pb)	Observed limit (pb)	Expected limit(pb)
124	0.0169	0.142	0.083
154	0.00719	0.189	0.108
185	0.00344	0.259	0.147
216	0.00179	0.356	0.205
247	0.000988	0.238	0.269
278	0.000572	0.356	0.385
309	0.000344	0.370	0.489

Table 7.19.: The cross section for stau pair production at $\sqrt{s} = 7$ TeV predicted by theory at the NLO and the upper limits.

Mass	NLO prediction (pb)	Observed limit (pb)	Expected limit(pb)
124	0.0212	0.091	0.055
154	0.0092	0.119	0.068
185	0.0045	0.148	0.085
216	0.00239	0.185	0.103
247	0.00135	0.242	0.146
278	0.0008	0.175	0.194
309	0.00049	0.235	0.267

Table 7.20.: The cross section for stau pair production at $\sqrt{s} = 8$ TeV predicted by theory at the NLO and the upper limits.

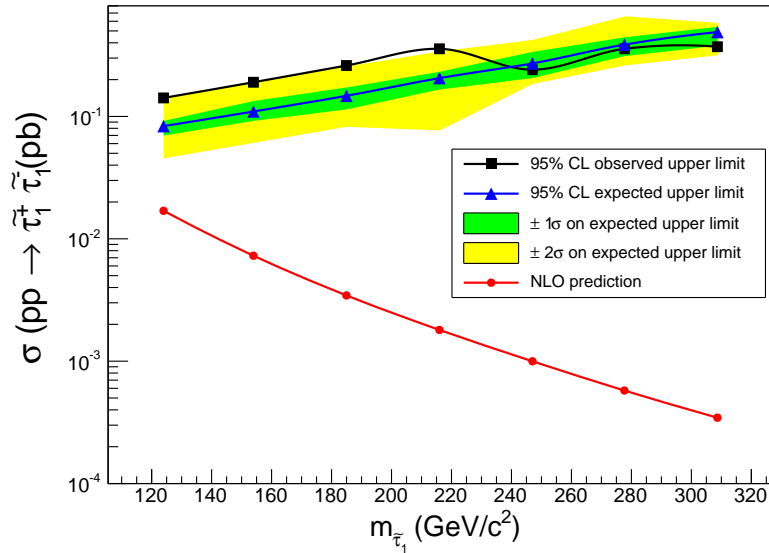


Figure 7.18.: The upper limits on the cross section of the stau pair production in the pp collisions at $\sqrt{s} = 7$ TeV

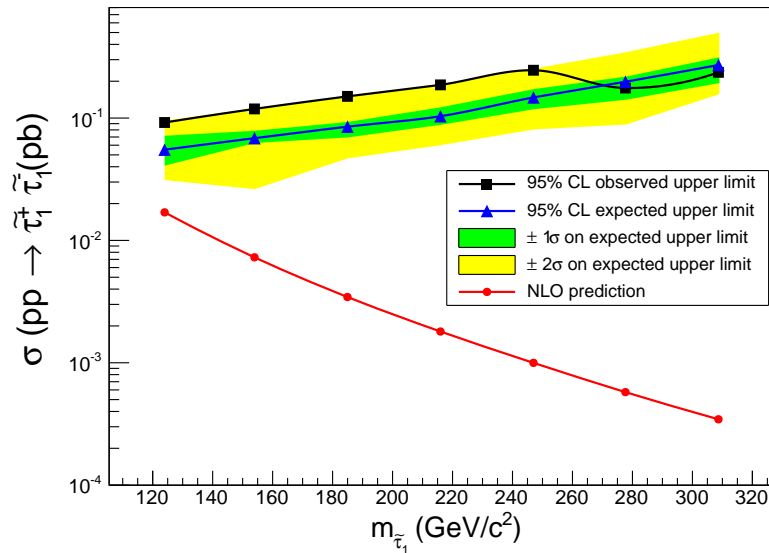


Figure 7.19.: The upper limits on the cross section of the stau pair production in the pp collisions at $\sqrt{s} = 8$ TeV.

We now compare our results to the ones of the D \oslash and ATLAS experiments which were published in [55] and [56] (see figure 7.20).

The upper limits on the cross section of stau pair production at 95%CL of the D0 experiment are set by using 1.1 fb^{-1} of data collected in $p\bar{p}$ collisions at $\sqrt{s} = 1.96$

TeV [55]. We have 1 fb^{-1} of data at 7 TeV and 2 fb^{-1} of data at 8 TeV, but our signal acceptance is smaller. $D\emptyset$ observed one event, corresponding to stau mass from 100 to 300 GeV/c^2 , and its expected background numbers are around 2 events [55]; while depending on the used methods we observed no event or one event and our expected background numbers are always less than 0.2. Therefore our limits are higher than the ones from $D\emptyset$.

The ATLAS experiment gave upper limits which are much lower than ours and $D\emptyset$'s [56]. The ATLAS experiment has a much higher potential in the stau search than the LHCb and $D\emptyset$ experiments with a detector with an acceptance that is much higher than ours and a high luminosity. ATLAS used the data corresponding to a luminosity of 4.7 fb^{-1} (see figure 7.20(b)).

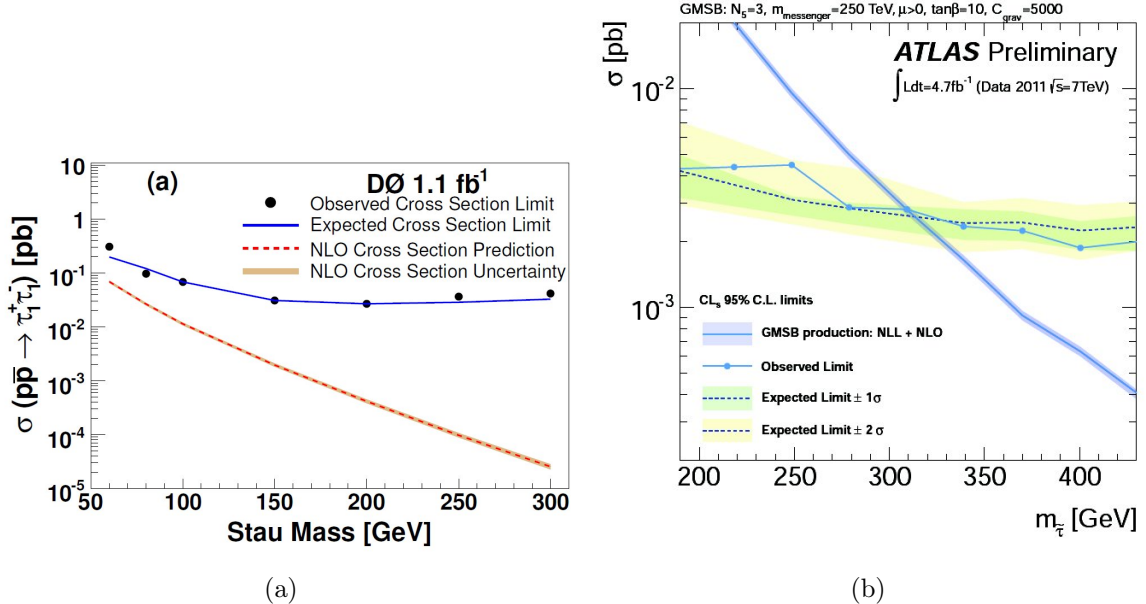


Figure 7.20.: (a): the upper limits on the cross section of the stau pair production in the $p\bar{p}$ collisions at $\sqrt{s} = 1.96 \text{ TeV}$ from the $D\emptyset$ experiment [55]. (b): the upper limits on the cross section of the stau pair production in the $p\bar{p}$ collisions at $\sqrt{s} = 7 \text{ TeV}$ from the ATLAS experiment [56].

Conclusions and Outlook

Through this PhD thesis, we have undertaken a search for heavy and long-lived staus in the LHCb detector at $\sqrt{s} = 7$ and 8 TeV.

- In our study, the muon pairs from decays $Z^0, \gamma^* \rightarrow \mu^+\mu^-$ are the main background to stau pairs as they are both long-lived and have the same electromagnetic interactions in matter. We have simulated the muon pairs and stau pairs of seven different masses ranging from 124 to 309 GeV/c^2 , in order to examine their characteristics in the detector. Based on the results of the Monte Carlo, we have defined a set of selection cuts for the stau pairs. Definitely, the muon pairs at high energies will also pass these cuts and they are much more abundant than the staus due to the difference between their production cross sections in pp collisions.
- To distinguish the stau pairs from the muon pairs, we employed their properties in the sub-detectors:
 - + The difference in the masses of the staus and of the muons leads to a difference between the energies they leave by ionisation and excitation of the atoms in the silicon sensors of the VELO sub-detector.
 - + The muons can radiate at high momentum, while the staus cannot because of their heavy mass. Hence, the total energy depositions of the staus in the thick detectors, ECAL and HCAL, are probably smaller than those of the muons.
 - + The momentum thresholds to trigger the Cherenkov effect in the RICH detectors for the staus are much higher than for the muons.
- Based on the different responses of the sub-detectors (VELO, ECAL, HCAL and RICH), we established the method to classify the stau and muon pairs with two steps:
 - + Analysis of the individual tracks: we used the MC responses from the four above mentioned sub-detectors to train a Neural Network. Then, the trained Neural Network was used to classify the tracks of the pairs selected from data. This method requires that the responses described by Monte Carlo agree with those in the data. To guarantee this agreement, the MC responses have been calibrated.
 - + Selection of the stau pairs: two methods were used. The first one is to put a cut on the product of the two NN responses for the two tracks, the so-called "pair significance". The second one is to use the pair significance and the invariant mass of the pairs from MC events to train a second Neural Network, then a cut is applied on the output of the second Neural Network. The cuts in the two methods define a

region of signal, where we can evaluate the expected numbers of stau and muon pairs.

- The above methods have been applied to the data collected by the LHCb experiment at $\sqrt{s} = 7$ TeV and $\sqrt{s} = 8$ TeV. The integrated luminosities for these two years of running were 1.01 fb^{-1} and 2.1 fb^{-1} . No significant excess of signal has been observed.
- Furthermore, we calculated the upper limits at 95% CL on cross section for stau pair production in pp collisions at $\sqrt{s} = 7$ and 8 TeV by using the profile likelihood method.

In the future, when the LHC reaches higher energies, the cross section for stau pair production in pp collisions will increase. This will offer the possibility of getting more positive signal. It also allows us to study the higher masses of the staus.

Bibliography

- [1] Guy D. Coughlan, James E. Dodd, Ben M. Gripaios, *The ideas of particle Physics - An introduction for scientists*, Cambridge University Press, ISBN 0-521-67775-0
- [2] W. E. Burcham and M. Jobes, *Nuclear and Particle Physics*, Longman Scientific and Technical.
- [3] Jean-Pierre Derendinger , *Théorie quantique des champs*, 2001, Presses Polytechniques et Universitaires Romandes.
- [4] J. Beringer et al. (Particle Data Group), Phys. Rev. D86, 010001 (2012), pages 177-198.
- [5] M. S. Longair, *High energy astrophysics*, Second Edition, Volume 2, Cambridge University Press
- [6] Stephen P. Martin, *A Supersymmetry Primer*, Northern Illinois University and Fermi National Accelerator Laboratory, arXiv:hep-ph/9709356, version 6, September 2011.
- [7] Ian J. R. Aitchison, *Supersymmetry and the MSSM: An Elementary Introduction*, Oxford University, arXiv:hep-ph/0505105v1 12 May 2005
- [8] Michael E. Peskin, *Supersymmetry in Elementary Particle Physics*, arXiv:0801.1928v1 [hep-ph] 13 Jan 2008, SLAC-PUB-13079
- [9] G.F. Giudice and R. Rattazzi, *Theories with Gauge-Mediated Supersymmetry Breaking*, Theory Division - CERN, arXiv:hep-ph/9801271v2 19 Apr 1999, Phys.Rept. 322 (1999) 419-499
- [10] John Ellis, *Limits of the Standard Model*, CERN-TH/2002-320, hep-ph/0211168, 12 Nov 2002
- [11] J. Beringer et al. (Particle Data Group), Phys. Rev. D86, 010001 (2012), pages 209-217.
- [12] Giuseppe Bozzi, Benjamin Fuks and Michael Klasen, *Threshold Resummation for Slepton-Pair Production at Hadron Colliders*, arXiv:hep-ph/0701202v3 1 Jun 2007
- [13] <http://home.web.cern.ch/about/accelerators/large-hadron-collider>
- [14] Jeroen van Tilburg, *Track simulation and reconstruction in LHCb*, 2005, Ponsen & Looijen b.v.

- [15] <http://aliceinfo.cern.ch/>
- [16] <http://atlas.ch/>
- [17] <http://cms.web.cern.ch/>
- [18] <http://lhcb.web.cern.ch/lhcb/>
- [19] <http://totem.web.cern.ch/Totem/>
- [20] <http://home.web.cern.ch/about/experiments/lhc1f>, <http://hep.fi.infn.it/LHCf/>
- [21] <http://moedal.web.cern.ch/>
- [22] The LHCb Collaboration, *The LHCb Detector at the LHC*, 2008 JINST 3 S08005
- [23] R. Forty, *RICH pattern recognition for LHCb*, Nucl.Instrum.Meth. A433 (1999) 257-261
- [24] , The LHCb RICH group, *Performance of the LHCb RICH detector at the LHC*, arXiv:1211.6759v2 [physics.ins-det] 17 Sep 2013
- [25] F. Archillia and all, *Performance of the Muon Identification at LHCb*, arXiv:1306.0249v2 [physics.ins-det] 3 Aug 2013
- [26] <http://lhcb-comp.web.cern.ch/lhcb-comp/>
- [27] W. Porod, *SPPheno, a program for calculating supersymmetric spectra, SUSY particle decays and SUSY particle production at e^+e^- colliders*, Comput. Phys. Commun. 153 (2003) 275 arXiv:hep-ph/0301101.
- [28] B.C. Allanach, *The Snowmass Points and Slopes: Benchmarks for SUSY Searches*, arXiv:hep-ph/0202233v1 25 Feb 2002
- [29] Torbjörn Sjöstrand, Stephen Mrenna and Peter Skands, *PYTHIA 6.4 Physics and Manual*, arXiv:hep-ph/0603175v2 12 May 2006
- [30] H. L. Laif and all, *Global QCD Analysis of Parton Structure of the Nucleon: CTEQ5 Parton Distributions*, HEP-ph/9903282, arXiv:hep-ph/9903282v3 6 Aug 1999
- [31] W. Beenakker, R. Höpker, and M. Spira, *PROSPINO: a program for the PROduction of Supersymmetric Particles In Next-to-leading Order QCD*, hep-ph/9611232, arXiv:hep-ph/9611232v1 5 Nov 1996
- [32] <http://www.thphys.uni-heidelberg.de/~plehn/index.php?show=prospino&visible=tools>
- [33] Pavel M. Nadolsky and all, *Implications of CTEQ global analysis for collider observables*, arXiv:0802.0007v3 [hep-ph] 17 Mar 2008
- [34] <http://geant4.cern.ch/>
- [35] The LHCb collaboration, *Measurement of the cross-section for $Z, \gamma^* \rightarrow \mu^+\mu^-$ production with 1 fb^{-1} of pp collisions at $\sqrt{s} = 7 \text{ TeV}$* , LHCb-CONF-2013-007.

- [36] <http://theory.fi.infn.it/grazzini/dy.html>
- [37] Ryan Gavin, Ye Li, Frank Petriello and Seth Quackenbush, *FEWZ 2.0: A code for hadronic Z production at next-to-next-to-leading order*, arXiv:1011.3540
- [38] A.D. Martin, W.J. Stirling, R.S. Thorne and G. Watt, *Parton distributions for the LHC*, arXiv:0901.0002v3 [hep-ph] 7 Jul 2009
- [39] R. Aaij et al., *The LHCb trigger and its performance in 2011*, JINST 8 (2013) P04022.
- [40] J. Albrecht, V. V. Gligorov, G. Raven, S. Tolk, *Performance of the LHCb High Level Trigger in 2012*, arXiv:1310.8544v1
- [41] J. Beringer et al. (Particle Data Group), Phys. Rev. D86, 010001 (2012), pages 323-338.
- [42] LA Thi Viet Nga, *Identification des Charginos par leur énergie déposée dans le détecteur VELO de LHCb*, 2009, <http://lphe.epfl.ch/publications/theses.php#mast>
- [43] Jie Chen and Todd Adams, *Searching for high speed long-lived charged massive particles at the LHC*, Eur. Phys. J. C (2010) 67: 335–342
- [44] Matthew Coombes, *Search for long lived charged particles in the LHCb RICH detector*, Exotica and Jets meeting, Wednesday 20th April 2011, <https://indico.cern.ch/conferenceDisplay.py?confId=135970> or http://lhcb-physics2011.physi.uni-heidelberg.de/Programme/talks/M-Coombes_ParticleSearch.pdf
- [45] James Michael Keaveney, *A measurement of the Z cross-section at LHCb*, CERN-THESIS-2011-202
- [46] A. Hoecker and all, TMVA 4 - Toolkit for Multivariate Data Analysis with ROOT, arXiv:physics/0703039
- [47] The LHCb Collaboration, *Absolute luminosity measurements with the LHCb detector at the LHC*, 2012 JINST 7 P01010
- [48] Michael Krämer and all, *Supersymmetry production cross sections in pp collisions at $\sqrt{s} = 7$ TeV*, arXiv:1206.2892
- [49] Robert D. Cousins, James T. Linnemann and Jordan Tucker, *Evaluation of three methods for calculating statistical significance when incorporating a systematic uncertainty into a test of the background-only hypothesis for a Poisson process*, arXiv:physics/0702156
- [50] Kyle S. Cranmer, *Frequentist Hypothesis Testing with Background Uncertainty*, arXiv:physics/0310108
- [51] Gary J. Feldman and Robert D. Cousins, Phys. Rev. D 57, 3873–3889 (1998)

- [52] <https://twiki.cern.ch/twiki/bin/view/RooStats>
- [53] Lorenzo Moneta and all, The RooStats Project, arXiv:1009.1003
- [54] <http://root.cern.ch/drupal/>
- [55] D0 Collaboration, *Search for Long-Lived Charged Massive Particles with the D0 Detector*, Phys. Rev. Lett. 102 161802 (2009)
- [56] ATLAS Collaboration, *Searches for heavy long-lived sleptons and R-hadrons with the ATLAS detector in pp collisions at $\sqrt{s} = 7$ TeV.*, Physics Letters B 720 (2013) 277–308

List of Figures

1.1. The interaction energy chosen for the two components of the Higgs field. The state of minimum energy corresponds to a non-zero value for the field[1].	8
1.2. The coupling constants as a function of energy using SM expression; α^{-1} is the inverse of the coupling constants, the horizontal axis scale is the exponent of the energy scale in GeV[11].	11
1.3. The loop containing a Dirac fermion f that couples to Higgs field[6].	12
1.4. The velocities as a function of radius are measured using Kepler's law and for the luminous matter for the galaxy M33.	13
2.1. Feynman diagrams presenting the contributions to the Higgs mass from fermion in (a) and from boson in (b)[6].	16
2.2. The coupling constants as a function of $\log Q$ in the SM and in the MSSM; where α_i^{-1} is the inverse of the coupling constants, the index $i = 1,2,3$ [11]. . .	26
2.3. The Yukawa coupling between Higgs boson and top quark (a), Higgsino ans stops (b),(c)[6].	27
2.4. The mechanism for mediating the SUSY breaking source from the secluded sector to the visible sector in the GMSB models.	34
2.5. The loop gives masses to the gauginos[6].	36
2.6. A mass spectrum and life time of the particles in the mGMSB, where the stau is the NLSP marked by the blue star. The stau has a mass of $124 \text{ GeV}/c^2$ and a lifetime of 184 ns.	38
2.7. Feynman diagrams for stau pair production at leading order in perturbative QCD (a) and at next-to-leading order (NLO) (b)[12].	39
3.1. The LHC scheme (a) and the LHC tunnel (b).	44
4.1. The global LHCb detector	45
4.2. LHCb magnet in xy plane in (a); the vertical magnetic field along the z -axis in (b).	46

4.3. The top figure shows the arrangement of the silicon sensors in the xz plane, at $y = 0$, when the VELO is fully closed. The bottom figures describe the relative positions of a right sensor and a left sensor when the VELO is fully closed or opened.	48
4.4. In (a), the VELO modules and the RF box. In (b), the overlap of the RF-foil corrugated faces when the detector halves are in the fully closed position. The other edges of the boxes are cut away. The R and ϕ -sensors are in different colours.	48
4.5. Overview of the VELO vacuum vessel.	49
4.6. Two stations of the TT.	50
4.7. The second layer of TT (a) and the two types of the TT half-modules: the 4-2-1 type in (b) and the 4-3 type in (c).	51
4.8. The structure of the TT stations.	51
4.9. The four individual detector boxes of an IT station.	52
4.10. Layouts of the x layer in (a) and of the u layer in (b).	52
4.11. The OT layer composes of 14 long modules and 8 short modules.	53
4.12. A module of 64 straw tubes in (a); the structure of a straw in (b).	54
4.13. Five track types in LHCb.	54
4.14. Cherenkov angle versus the particle momentum in the three RICH radiators.	56
4.15. The schematic layouts of the RICH1 in (a) and the RICH2 in (b).	56
4.16. The schema of a HPD in (a); The HPD used for RICHs of LHCb in (b).	57
4.17. Interaction of particles and the evolution of their showers in the LHCb calorimeter system.	59
4.18. The quarter of ECAL with inner, middle and outer sections.	61
4.19. Three types of modules are used in ECAL.	61
4.20. The quarter of HCAL with inner and outer sections in (a); the schematic of the HCAL cell structure in (b).	62
4.21. View of the muon system.	63
4.22. One quadrant of a station in the xy plane, each rectangle represents one chamber.	63
4.23. Cross section of MWPC showing the five panels defining four gaps.	64
4.24. Cross section of the strip-GEM chamber.	64

5.1. Invariant masses of the stau pairs. Figures (a) and (b) correspond to the two masses of 124 and 309 GeV/c^2 respectively.	74
5.2. Velocity of the staus generated in pp collisions at 7 TeV. The stau masses are 124 GeV/c^2 and 309 GeV/c^2 in figure (a) and (b) respectively.	74
5.3. P and P_T of the staus generated in pp collisions at $\sqrt{s} = 7$ TeV, figures (a, c) and (b, d) correspond to the staus of 124 and 309 GeV/c^2	75
5.4. Distributions of the pseudorapidity (η) for staus of 124 GeV/c^2 mass (a) and of 309 GeV/c^2 mass (b) passing through the LHCb acceptance.	75
5.5. Invariant mass distribution of stau pairs using the muon's mass (the true mass of the generated stau is 124 GeV/c^2) in (a). Distribution of $Z, \gamma^* \rightarrow \mu^+\mu^-$ decay selected from the 2011 data is shown in (b).	77
5.6. P_T distribution of 124 GeV/c^2 staus in (a) and the one of real muons in (b).	77
5.7. The chi-square per degree of freedom (χ^2/dof) is shown for staus of 124 GeV/c^2 mass (figure (a)) and for staus of 309 GeV/c^2 mass (figure (b)).	79
5.8. The relative momentum error (σ_P/P) is displayed for staus of 124 GeV/c^2 mass (figure (a)) and for staus of 309 GeV/c^2 mass (figure (b)).	79
5.9. P and P_T are reconstructed for tracks corresponding to staus of 124 GeV/c^2 mass.	80
5.10. P and P_T are reconstructed for tracks corresponding to staus of 309 GeV/c^2 mass.	80
5.11. ΔE deposited by the staus of 124 GeV/c^2 mass and the muons is plotted as a function of momentum (a). Projection of histogram (a) on the ΔE axis (b).	82
5.12. ΔE deposited by the staus of 309 GeV/c^2 mass and the muons is plotted as a function of momentum (a). Projection of histogram (a) on the ΔE axis (b).	82
5.13. Distributions of the momentum (a) and transverse momentum (b) of muon tracks from MC11 and 2011 data.	83
5.14. Distributions of the momentum (a) and transverse momentum (b) of muon tracks from MC12 and 2012 data.	83
5.15. In (a): distributions of ΔE in VELO from MC11 and 2011 data. In (b): the MC distribution was scaled by a factor of 0.93. In (c): the MC distribution was re-generated by a convolution of the scaled MC distribution with a Gaussian.	84
5.16. In (a): distributions of ΔE in VELO from MC12 and 2012 data. In (b): the MC distribution was scaled by a factor of 1.058. In (c): the MC distribution was re-generated by a convolution of the scaled MC distribution with a Gaussian.	84
5.17. The left figure (a) shows the deposited energies in ECAL as a function of the transverse momentum (P_T), the right histogram (b) is the projection on the deposited energy's axis. The staus used here have a mass of 124 GeV/c^2	85

5.18. The left figure (a) shows the deposited energies in HCAL as a function of the transverse momentum (P_T), the right histogram (b) is the projection on the deposited energy's axis. The staus used here have a mass of $124 \text{ GeV}/c^2$	86
5.19. (a): Original distributions of the total deposited energies of muons from MC11 and 2011 data in ECAL. (b): the MC11 distribution was scaled by a factor of 0.80.	87
5.20. (a): Original distributions of the total deposited energies of muons from MC12 and 2012 data in ECAL. (b): the MC12 distribution was scaled by a factor of 0.79.	87
5.21. (a): Original distributions of the total deposited energies of muons from MC11 and 2011 data in HCAL. (b): the MC11 distribution was scaled by a factor of 0.85.	88
5.22. (a): Original distributions of the total deposited energies of muons from MC12 and 2012 data in HCAL. (b): the MC12 distribution was scaled by a factor of 0.84.	88
5.23. Figure (a): the distributions of the ratio between the sum of the total deposited energies of the muon and stau tracks in the ECAL and HCAL and their momentum; the mass of stau is $124 \text{ GeV}/c^2$. Figure (b): the same variable for muons from the mis-ID source. Note the different scales on the horizontal axes.	89
5.24. Particle identification (PID) given by RICHs for the muons and staus simulated in MC11. The staus in figure (a) and (b) have the masses of $124 \text{ GeV}/c^2$ and of $309 \text{ GeV}/c^2$, respectively.	91
5.25. Distribution of the delta log-likelihood for the below threshold particle hypothesis that the RICHs give to the muon and stau tracks simulated by MC11. The two figures (a) and (b) use staus of 124 and $309 \text{ GeV}/c^2$ masses, respectively.	91
5.26. In (a): the original distributions of the delta log-likelihood for the below-threshold particle hypothesis from muon tracks in MC11 and 2011 data. In (b): the MC11 distribution was generated again to make it similar to the one in data.	92
5.27. Impact parameter of stau tracks ($m_{\tilde{\tau}} = 124 \text{ GeV}/c^2$) and muon tracks from Z^0, γ^* decays with respect to the best primary vertex in figure (a). The distributions for other backgrounds in figure (b).	93
5.28. The asymmetry in transverse momentum of the two particles in the stau and muon pairs. The staus used in figures (a) and (b) have the masses of 124 and $309 \text{ GeV}/c^2$ respectively.	94
5.29. The pair isolation of the stau pairs ($m_{\tilde{\tau}} = 124 \text{ GeV}$) and the muon pairs from Z^0, γ^* decays in figure (a). The distributions of the same variable for the other backgrounds.	95
6.1. The four variables of the stau and muon tracks used as inputs of the NN.	100

6.2. NN1 responses for MC muon tracks and MC stau tracks. Figure (a) shows the NN1 response for the staus of $124 \text{ GeV}/c^2$ mass and figure (b) is for the staus of $309 \text{ GeV}/c^2$ mass. The vertical scale is logarithmic.	101
6.3. The <i>pair significance</i> of the muon pairs and the stau pairs with the masses of $124 \text{ GeV}/c^2$ (a) and $309 \text{ GeV}/c^2$ (b).	102
6.4. Invariant mass of the muon pairs and the stau pairs with the original masses of $124 \text{ GeV}/c^2$ (a) and $309 \text{ GeV}/c^2$ (b).	104
6.5. NN2 responses for stau and muon pairs. The original masses of the staus in (a) and (b) are $124 \text{ GeV}/c^2$ (a) and $309 \text{ GeV}/c^2$, respectively.	104
6.6. Significance $S/\sqrt{S+B}$ versus the NN2 response. Figures (a) and (b) correspond to the histograms 6.5(a) and 6.5(b), respectively.	105
6.7. The green boundary separates the stau and the muon regions in the bi-parametric histogram of the pair significance and the invariant mass. Figures (a) and (b) correspond to the staus of 124 and $309 \text{ GeV}/c^2$ masses, respectively.	105
7.1. P and P_T of the tracks of the pairs selected in the 2011 data by the selection cuts corresponding to staus of $124 \text{ GeV}/c^2$ mass.	110
7.2. P and P_T of the tracks of the pairs selected in the 2012 data by the selection cuts corresponding to staus of $124 \text{ GeV}/c^2$ mass.	110
7.3. The input variables to the first NN. The tracks are selected from the 2011 data and the selection cuts correspond to staus of the $124 \text{ GeV}/c^2$ mass.	111
7.4. The input variables to the first NN. The tracks are selected from the 2012 data and the selection cuts correspond to staus of the $124 \text{ GeV}/c^2$ mass.	112
7.5. NN1 classification for tracks selected according to criteria defined for stau mass of $124 \text{ GeV}/c^2$	113
7.6. Pair significance of the pairs selected from the 2011 data (a) and 2012 data (b) with the selection cuts corresponding to the case of the $124 \text{ GeV}/c^2$ mass.	113
7.7. Invariant mass of the pairs selected from the 2011 data (a) and the 2012 data (b) with the selection cuts corresponding to the case of the $124 \text{ GeV}/c^2$ mass.	114
7.8. NN2 response for the pairs selected by the cuts corresponding to the staus of $124 \text{ GeV}/c^2$ mass in the 2011 data.	115
7.9. NN2 response for the pairs selected by the cuts corresponding to the staus of $124 \text{ GeV}/c^2$ mass in the 2012 data.	115
7.10. Global view of the observed event from the 2011 data in the LHCb detector. The tracks with the $P_T < 1 \text{ GeV}/c$ are not displayed.	117

7.11. Primary vertices reconstructed in the event observed from the 2011 data.	118
7.12. The VELO track segments of the event observed from the 2011 data.	119
7.13. Panorama of the observed event from the 2012 data in the LHCb detector. The tracks with the $P_T < 1$ GeV/c are not displayed.	120
7.14. Primary vertices reconstructed in the event observed from the 2012 data.	122
7.15. The VELO track segments of the event observed from the 2012 data.	122
7.16. Upper limits on the cross section for stau pair production in the pp collisions at $\sqrt{s} = 7$ TeV (no event observed).	131
7.17. Upper limits on the cross section for stau pair production in the pp collisions at $\sqrt{s} = 8$ TeV (no event observed).	131
7.18. The upper limits on the cross section of the stau pair production in the pp collisions at $\sqrt{s} = 7$ TeV	133
7.19. The upper limits on the cross section of the stau pair production in the pp collisions at $\sqrt{s} = 8$ TeV.	133
7.20. (a): the upper limits on the cross section of the stau pair production in the $p\bar{p}$ collisions at $\sqrt{s} = 1.96$ TeV from the D \oslash experiment[55]. (b): the upper limits on the cross section of the stau pair production in the pp collisions at $\sqrt{s} = 7$ TeV from the ATLAS experiment[56].	134

List of Tables

1.1.	The elementary particles of the Standard Model	6
1.2.	The bosons before and after the spontaneous symmetry breaking. In parentheses are the physical degrees of freedom of the particles.	9
2.1.	Chiral supermultiplets in the Minimal Supersymmetric Standard Model.	17
2.2.	Gauge supermultiplets in the Minimal Supersymmetric Standard Model.	18
2.3.	The particles in the MSSM.	33
4.1.	The muon stations are required to have hits in the FOI in order to identify muons.	65
4.2.	The input and output rates for three levels.	65
5.1.	The six GMSB parameters and the corresponding masses and lifetimes of staus.	72
5.2.	Cross sections of the stau pair production at NLO in pp collisions of $\sqrt{s} = 7$ and 8 TeV in full acceptance.	73
5.3.	Acceptance factors of the stau pair in pp collisions of $\sqrt{s} = 7$ and 8 TeV.	73
5.4.	Cross section for the decay $Z, \gamma^* \rightarrow \mu^+ \mu^-$ in pp collisions. The first uncertainty is from the choice of PDF, the second one is from the theory.	78
5.5.	The factors have been used to scale the MC distributions of the total deposited energies in the calorimeters.	86
5.6.	The thresholds of momentum to generate Cherenkov light for muons and staus in the RICH radiators.	90
5.7.	The PIDs corresponding to the identified particles by RICHs.	90
5.8.	Cuts on the momentum of the track to select the staus.	96
5.9.	Selection efficiencies for muon and stau pairs using the selection cuts. These values are for MC11.	97

5.10. Selection efficiencies for muon and stau pairs using the selection cuts. These values are for MC12.	97
5.11. Expected number of selected stau and muon pairs.	97
6.1. Cuts on the pair significance to separate the stau pairs and the muon pairs. . .	101
6.2. Fraction (R) of the muon pairs staying in the stau region.	102
6.3. Expected numbers of the stau pairs and the muon pairs in the stau region for the luminosities of 1.01 and 2.1 fb^{-1}	103
6.4. Fraction (R) of surviving stau and muon pairs in the stau region.	106
6.5. Expected numbers of the stau pairs and the muon pairs in the stau region for the luminosities of 1.01 and 2.1 fb^{-1}	106
7.1. The numbers of pairs selected by the cuts in the 2011 data.	109
7.2. The numbers of pairs selected by the cuts in the 2012 data.	110
7.3. The number of pairs observed in the stau region from 2011 and 2012 data. . .	116
7.4. Reconstructed information from the candidate event from the 2011 data in the LHCb detector.	116
7.5. Primary vertices reconstructed in the event observed from the 2011 data. . .	118
7.6. Reconstructed information of the observed event from the 2012 data in the LHCb detector.	121
7.7. Primary vertices reconstructed in the event observed from the 2012 data. . .	121
7.8. Cross section of the stau pair production at pp collisions at $\sqrt{s} = 7$ and 8 TeV. The systematic uncertainties (%) are relative ones.	124
7.9. Cross section of the decay $Z, \gamma^* \rightarrow \mu^+ \mu^-$ in pp collisions at $\sqrt{s} = 7$ and 8 TeV. The systematic uncertainties (%) are relative ones.	125
7.10. Efficiencies of the muon tracking.	126
7.11. Efficiencies of the trigger cut.	126
7.12. The differences between the efficiencies when the additional cuts are applied. .	127
7.13. Total uncertainty (%) on the selection efficiencies for the muon pairs.	127
7.14. The total uncertainties on the expected number of the stau pairs in the stau region estimated for 2011 data.	128
7.15. The total uncertainties on the expected number of the stau pairs in the stau region estimated for 2012 data.	129

7.16. The total uncertainties on the expected numbers of the muon pairs estimated for 2011 and 2012 data.	129
7.17. Cross section for stau pair production at $\sqrt{s} = 7$ TeV as predicted by theory at the NLO and the upper limits in the case where no event has been observed. .	130
7.18. Cross section for stau pair production at $\sqrt{s} = 8$ TeV as predicted by theory at the NLO and the upper limits in the case where no event has been observed. .	130
7.19. The cross section for stau pair production at $\sqrt{s} = 7$ TeV predicted by theory at the NLO and the upper limits.	132
7.20. The cross section for stau pair production at $\sqrt{s} = 8$ TeV predicted by theory at the NLO and the upper limits.	132

CURRICULUM VITAE

LA Thi Viet Nga
ltvnga84@gmail.com

Personal Profile

Date of birth Oct 25th, 1984
Place of birth Ninh Binh province, Vietnam
Citizenship Vietnamese
Gender Female

Key Strengths

High education in high energy physics; experiences in simulation, analysis and statistics; good computer programming skills and good teamwork abilities.

Education

2009 - 2013 PhD in High Energy Physics, EPFL, Switzerland
Thesis: A search for heavy long-lived staus in the LHCb detector at $\sqrt{s} = 7$ and 8 TeV.
Supervisor: Dr. Minh-Tam Tran (EPFL)
2009 Master Degree in Nuclear Physics and Applications
Bordeaux I University, France
2006 Bachelor degree in Physics
Hanoi University of Sciences, Vietnam

Experiences

2009 - 1012 Teaching Assistant, School of Basic Sciences (EPFL)
Subjects: General Physics and Nuclear Physics.

Languages

Vietnamese, English, French

Computer skills

OS Linux/Unix, Windows
Programing C++, Python
Scientific Mathlab, ROOT
Application Latex, Microsoft Office